

JEAN-CHARLES SAINT-MARC

**Development of a ballistic hybrid fabric model for aeroengine fan
blade containment application**

Mémoire présenté
à la Faculté des études supérieures et postdoctorales de l'Université Laval
dans le cadre du programme de maîtrise en génie mécanique
pour l'obtention du grade de Maître ès sciences (M.Sc.)

DÉPARTEMENT DE GÉNIE MÉCANIQUE
FACULTÉ DES SCIENCES ET DE GÉNIE
UNIVERSITÉ LAVAL
QUÉBEC

2012

Résumé

Ce mémoire présente les travaux de recherche effectués au sein du département de Génie Mécanique de l'Université Laval dans le cadre du projet « Impact modeling of Composite Aircraft Structure », IMCAS du Consortium de Recherche et d'Innovation en Aérospatiale (CRIAQ).

Le but de ces travaux était de créer une loi de comportement pour les composites tissés sec mous et de les implanter dans un élément coque reproduisant le comportement dynamique d'un croisement de fibres dans un pli typique sous impact balistique et en fonction de certains paramètres géométriques propres au tissé. La création d'une loi de comportement de l'utilisateur dans le logiciel d'analyse par éléments finis Abaqus a été nécessaire pour mener à bien ce projet.

La méthodologie de développement de la sous-routine de l'utilisateur, qui définit le matériau tissé et est utilisée en conjonction avec l'élément shell S4R, est basée sur les récents travaux de Grujicic et al (1) et Shahkarami et al (2). La validation de ce modèle a été réalisée en vérifiant la validité de sa réponse à certaines sollicitations rencontrées dans des études simples d'impact. Le résultat final de ces tests numériques d'impact a permis de démontrer que nous obtenons des résultats similaires à ceux de Shahkarami pour les mêmes paramètres d'expérimentation. Enfin, après cette dernière validation, nous avons appliqué l'outil développé à l'étude, en dynamique explicite, de l'impact d'une pale de soufflante sur un caisson de confinement hybride. Ce caisson est composé d'une première couche intérieure en coque métallique et sur laquelle s'empilent plusieurs couches de kevlar.

Tout au long de ce mémoire, nous avons détaillé toutes les hypothèses, les démarches et les outils utilisés pour réaliser ce travail. Nos résultats montrent finalement qu'il est possible de reproduire les phénomènes physiques à une échelle méso-mécanique lors d'un impact haute vitesse sur un matériau composite tissé multicouche tout en minimisant le temps de calcul nécessaire.

Abstract

This thesis presents the work that has been carried out inside the Mechanical Engineering Department of Laval University within a CRIAQ project related to Impact Modeling of Composite Aircraft Structure (IMCAS).

The main goal of this work was to develop a dry fabric model for ballistic impact application and to implement it into a shell element capable of reproducing the dynamic behavior of a yarn crossover point with due account of some specific geometric and material parameters. The development of a material user subroutine (VUMAT user subroutine) was necessary to carry out this project.

The methodology employed for the development of the user subroutine to be used with the S4R shell element available in Abaqus is based upon the works of Grujicic et al (1) and Shahkarami et al (2). The validity of the mesomechanical model created was carried out in order to assess the accuracy of its behavior under elementary loadings. Subsequently, using the same parameters to set up the analysis, the developed model has been applied in simple impact problems in Abaqus to demonstrate that we are able to obtain the same results as in the work of Shahkarami (2) used as a reference. Finally, after this last validation, the model is used in the impact study of an aeronautical engine's fan blade containment problem using a hybrid casing. In our problem the casing's inner shell is metallic and multiple Kevlar fabric layers are wrapped around it to contribute to the energy absorption and containment of the fan blade debris released outward at high speed.

In this thesis all the assumptions, process and tools necessary to carry out every analysis have been described in details. Our results demonstrate that it is possible to capture the physical phenomenon happening at the yarn's mesoscopic level during a high-velocity impact on a dry fabric while minimizing the computation time.

Table of Contents

Résumé.....	iii
Abstract.....	ii
Table of Contents.....	iv
List of Tables.....	viii
List of Figures.....	ix
Acknowledgements.....	xii
Dedication.....	xiii
CHAPTER 1 - INTRODUCTION: DYNAMIC ANALYSIS OF FABRIC SYSTEMS.....	1
1.1 Textile composites.....	3
1.1.1 Composite under impact.....	3
1.1.2 Numerical impact modeling on textiles.....	3
1.2 Research objectives and methodology.....	5
1.2.1 Objectives.....	5
1.2.2 Methodology.....	5
1.3 Outline of the thesis.....	6
CHAPTER 2 - OVERVIEW ON TEXTILE COMPOSITES.....	9
2.1 Fibers in textile composites.....	9
2.1.1 Glass fibers.....	10
2.1.2 Carbon fibers.....	10
2.1.3 Organic fibers.....	12
2.2 Yarns types.....	13
2.3 Fabric structure.....	14
2.3.1 Woven.....	14
2.3.2 Other types of fabrics.....	16
2.4 Multi-scale nature of composite materials.....	17
2.4.1 Observation of the fabric architecture.....	19
2.5 Mechanical properties of textiles reinforcements.....	19
2.5.1 Deformation modes in the fabrics architecture (1).....	20
2.5.2 Mechanical behavior of composites under various loadings.....	22
2.6 Conclusion.....	24
CHAPTER 3 - MODELING BALLISTIC FABRICS.....	25
3.1 Overview of ballistic fabric modeling techniques.....	25
3.1.1 Finite-element analyses based on the use of pin-jointed orthogonal bars.....	25
3.1.2 Detailed full-blown 3D continuum.....	26

3.1.3	Unit-cell based approach.....	26
3.1.4	Higher-order membrane/shell	27
3.2	Analytical based modeling for the unit-cell method.....	27
3.2.1	Meso-structurally based analytical models.....	28
3.2.2	Pin-jointed truss geometry	31
3.3	Continuum based modeling	32
3.3.1	3D solid models	33
3.3.2	Shell based unit-cell models	34
3.4	Literature review on shell based unit-cell models	35
3.5	Shell fabric unit-cell formulation description.....	39
3.5.1	Simplifying assumptions.....	39
3.5.2	In-plane extensional response.....	40
3.5.3	Shear Response	41
3.6	Governing equations of the model.....	43
3.6.1	Tension (4).....	43
3.6.2	Shearing (4).....	43
3.6.3	Yarns crossover contact (4)	45
3.6.4	Yarn bending (1).....	46
3.6.5	Yarn locking (1).....	46
3.7	Conclusion	47
CHAPTER 4 -	DESCRIPTION OF THE MAIN TOOLS	49
4.1	Explicit Dynamic FE formulation.....	49
4.1.1	Central difference integration rule	50
4.1.2	Time step control	51
4.2	Constitutive law of the model.....	52
4.3	Description of the Green-Naghdi hypoelastic approach.....	55
4.3.1	Updating current constitutive axes.....	56
4.3.2	Transforming strains and stresses between GN frame and yarn frame	57
4.3.3	Computation algorithm for the hypoelastic GN approach.....	58
4.3.4	Computation algorithm for Badel's fiber frame (FF) approach.....	59
4.4	Shell element description.....	60
4.4.1	S4R overview.....	61
4.4.2	S4R formulation.....	61
4.4.3	In-plane displacement hourglass control	68
4.4.4	Rotational hourglass control	70
4.4.5	Parametric interpolation.....	70
4.4.6	The rate of virtual work	71
4.4.7	Numerical integration	72
4.5	Conclusion	75

CHAPTER 5 - DEVELOPMENT AND TESTING OF THE 3D CROSSOVER MODEL	76
5.1 Model basics	77
5.2 3D model definition of the unit cell	79
5.2.1 Geometrical definition	79
5.2.2 Mechanical definition of the model	82
5.3 Testing of the fabric unit-cell	84
5.3.1 Extensional response of the unit-cell	84
5.3.2 Transverse compression of the unit cell	87
5.3.3 Shear behavior of the unit cell	89
5.4 Conclusions	90
CHAPTER 6 - DEVELOPMENT OF THE FABRIC UNIT-CELL CROSS-OVER MATERIAL MODEL SUBROUTINE	91
6.1 VUMAT subroutine description	92
6.1.1 Generalities on the subroutine	92
6.1.2 Material point deletion	93
6.2 User subroutine computations	96
6.2.1 Using the VUMAT in Abaqus	96
6.2.2 Short description of the VUMAT's built-in variables	97
6.2.3 Initial rigidity matrix	100
6.2.4 VUMAT computation steps	100
6.2.5 Newton-Raphson iterations	107
6.2.6 Tensile response	110
6.2.7 Shear response	112
6.2.8 Final computations	114
6.2.9 Intermediate result extraction	115
6.3 Shell element testing	115
6.3.1 Input parameters for the VUMAT	115
6.3.2 Uniaxial extensional response	115
6.3.3 Biaxial extensional response	118
6.3.4 Shear response	119
6.4 Conclusion	120
CHAPTER 7 - MODELING OF A BALLISTIC IMPACT ON A COMPOSITE PLATE	121
7.1 Analysis set-up for 1-ply model	121
7.1.1 Geometrical setup of the analysis	122
7.1.2 Definition of the materials	123
7.1.3 Definition of the step	124
7.1.4 Definition of the boundary conditions	125
7.1.5 Transverse shear stiffness	125
7.1.6 Interactions and contact properties	126
7.2 Analysis results discussion for 1-ply analysis	126

7.2.1	Projectile velocity analysis	128
7.2.2	Parametric study.....	129
7.3	Analysis results and discussion for 4-ply analysis.....	133
7.3.1	Graphical evolution of the analysis.....	134
7.3.2	Energies plots to validate the analysis	135
7.3.3	Comparison between FEM analysis and experiment.....	135
7.3.4	Mesh size influence on projectile velocity.....	136
7.4	Final velocity comparison between different layup configuration	138
7.5	Conclusion	141
CHAPTER 8 - MODELING THE IMPACT OF AN ENGINE FAN BLADE ON A COMPOSITE CASING		142
8.1	Overview of the analysis.....	142
8.2	First analysis setup: fan blade rotation.....	143
8.2.1	Analysis basics.....	143
8.2.2	Defining the geometry	143
8.2.3	Defining the material of the fan blade	145
8.2.4	Constraining the model.....	145
8.2.5	Applying the boundary conditions.....	146
8.2.6	Implicit analysis results.....	148
8.3	Second analysis setup: fan blade containment.....	148
8.3.1	Definition of the geometry.....	149
8.3.1	Definition of the materials	149
8.3.2	Interactions.....	150
8.3.3	Contact property.....	150
8.3.4	Boundary conditions	151
8.3.5	Predefined field.....	151
8.4	Impact on the hybrid casing.....	151
8.5	Impact on full metal casing.....	154
8.6	Hybrid fan case containment study.....	157
8.6.1	Computation interruption.....	160
8.7	Conclusion	161
GENERAL CONCLUSION		163
APPENDIX A – MAPLE CODE FOR PARAMETER DETERMINATION		165
APPENDIX B – NEWTON RAPHSON ALGORITHM		168
Bibliography		170

List of Tables

Table 2-1: Characteristics and Applications of Carbon Fibers (6)	12
Table 2-2: Geometrical parameters of the RVE to be defined in Abaqus	14
Table 5-1: Geometrical parameters of the RVE defined in Abaqus/CAE	80
Table 5-2: Mechanical parameters of the RVE defined in Abaqus/CAE	82
Table 7-1: Mechanical parameters of the steel impactor	123
Table 7-2: Summary of parameters used by the VUMAT to define the fabric	124
Table 7-3: Parameter a and b variation	132
Table 8-1: Titanium properties for the definition of the fan blade	145
Table 8-2: Aluminum properties for the definition of the fan blade.....	150
Table 8-3: Results obtained from FEA	156
Table 8-4: Weight reduction approximate study	161

List of Figures

Figure 1-1: Composite materials in new Boeing 787 Dreamliner (bintang.site11.com)	2
Figure 2-1: Schematic representation of carbon fiber preparation from PAN fibers (6).....	11
Figure 2-2: Representation of various weave patterns for textile reinforcements: plain weave a), twill weave b) and satin weave c) (7)	16
Figure 2-3: Non crimp fabric constituted of an assemblage of unidirectional plies stitched together (3).....	16
Figure 2-4: 3D fabric reinforcement (3)	17
Figure 2-5: Deformed geometry of RUC at mesoscale level in plane shear (8).....	18
Figure 2-6: Microscale image of a plain weave showing the undulation of the yarns and their cross-sectional shape (13).....	19
Figure 2-7: Fabric in uniaxial tensile deformation a) and in shear deformation b) (1)	20
Figure 2-8: Response of characterizing loads on a plain weave fabric: shear response a) and tensile response b) (14).....	22
Figure 2-9: Straightening of the yarns in case of uniaxial tension (14).....	22
Figure 2-10 Shearing effects taking place at the mesoscale level at crossover where the yarns interact: a) initial configuration, yarn undeformed b) final configuration, yarn deformed (15).....	24
Figure 3-1: Geometry proposed by Peirce (27)	28
Figure 3-2: Geometrical representation of the plain weave fabric unit-cell used by Bejan and Poterasu (28).....	29
Figure 3-3: Section description: a) section E-A, b) section A-H.....	30
Figure 3-4: Pin-jointed truss geometry proposed by Kawabata et al. (11)	32
Figure 3-5: Continuum modeling approaches.....	33
Figure 3-6: Full blown 3D modeling example.....	33
Figure 3-7: Unit-cell based modeling process from Grujicic et al (1).....	36
Figure 3-8: Illustration of the biaxial crossover model of a single plain weave fabric crossover with linear yarns originally developed by Kawabata et al. (21)	37
Figure 3-9: Cross-sectionnal micro-image of a plain weave fabric made of Kevlar fibers (2) ...	40
Figure 3-10: 3D finite element mesh of a single fabric crossover (left) and the equivalent mathematical representation of the yarns by their centerlines (right).....	41
Figure 3-11: Shear model representation.....	45
Figure 4-1: Explicit integration scheme loop.....	50
Figure 4-2: Initial frame e_{0i} , rotated frame e_i and yarn frame f_i in the case of unidirectional yarns	53
Figure 4-3: An element with simple shear under plane stress showing Green-Naghdi (n) and Fiber Frames (f) before and after deformation (41).....	56

Figure 4-4: Notation for the assumed strain field on the standard isoparametric element.	65
Figure 5-1: Cosine-based shape of an arbitrary yarn in a plain weave fabric (4).....	79
Figure 5-2: Initial lenticular shape of the yarns' cross-sectional area	81
Figure 5-3: Modified lenticular shape of the yarns' cross-sectional area.....	81
Figure 5-4: Undulated shape of one yarn in Abaqus	82
Figure 5-5: Crossover model in Abaqus	84
Figure 5-6: Biaxial extension of the crossover (magnitude of displacements U).....	85
Figure 5-7: Stress-strain relationship in direction one for the 3D crossover	86
Figure 5-8: Strain relationship for Poisson ratio.....	87
Figure 5-9: a) Compression model of the crossover in Abaqus b) Graphical results for the strains during the compression test.....	88
Figure 5-10: Transverse compaction characterization of the 3D crossover	89
Figure 6-1: Trellis mechanism in initial undeformed configuration.....	95
Figure 6-2: Trellis mechanism in deformed configuration	95
Figure 6-3: Geometry of the yarn crossover before and after deformation by symmetrically applied displacements along the two crossing yarn directions. Both yarns are shown on the same plane (1).....	96
Figure 6-4: Stress and strain components in fiber frame	104
Figure 6-5: Evolution of the Green-Naghdi and material frames during the deformation's evolution	105
Figure 6-6: A yarn in the fabric (left) in contact with the crossing yarn with a free body diagram showing the forces acting on it (right)	107
Figure 6-7: Yarn centerline height position depending on angle β	112
Figure 6-8: Shear modulus as a function of β	114
Figure 6-9: Application of the loads on the shell element for a simple extension test.....	116
Figure 6-10: Tension in the warp yarn during a simple extension test.....	116
Figure 6-11: Shahkarami et al. (4) unidirectional tensile loading curve for Kevlar S-726	117
Figure 6-12: Movement of the warp and fill yarn centerline at the crossing point during a simple extension test.....	117
Figure 6-13: Tension in the warp yarn during a biaxial extension test.....	118
Figure 6-14: Movement of the warp and fill yarn centerline at the crossing point during a simple extension test.....	119
Figure 6-15: Shear modulus evolution as a function of the transverse displacement of the yarns	119
Figure 7-1: a) Impactor section definition in the sketch module, b) final three dimensional geometry of the impactor to be used in the assembly	122
Figure 7-2: Model assembly with impactor and fabric plate	123
Figure 7-3: Boundary conditions applied on the model.....	125
Figure 7-4: Evolution of the impact analysis on a one-ply plain weave fabric over time (in milliseconds).....	127

Figure 7-5: Projectile velocity result.....	129
Figure 7-6: Initial velocity influence over projectile velocity during the analysis	130
Figure 7-7: Crimp influence over projectile velocity during the analysis	131
Figure 7-8: Plate sidelength influence over projectile velocity during the analysis	132
Figure 7-9: Compression parameters influence	133
Figure 7-10: Evolution of the ply stresses on a four-ply plain weave fabric over time (in milliseconds).....	134
Figure 7-11: Evolution of the kinetic, internal and total energy of the system over time (in milliseconds).....	135
Figure 7-12: Comparison between FEM and experimental analyses from Shahkarami (4) of the impact velocity.....	136
Figure 7-13: Mesh size influence over the results compared with the results obtained with the nominal mesh size.....	137
Figure 7-14: Mesh size influence over the projectile velocity throughout the analysis	138
Figure 7-15: Influence of the number of layers over the final velocity of the projectile.....	139
Figure 7-16: Prediction analysis to define the number of layers needed to stop the projectile .	140
Figure 7-17: Stresses caused by the projectile stopped by 6 layers of plain weave fabric	141
Figure 8-1: a) Fan blade geometry as defined by G. Toussaint (5). b) fan blade geometry defined in Abaqus for the present work.....	144
Figure 8-2: a) Coupling constraint between the control point and the base of the fan blade. b) Tie constraint between the two sub-components of the fan blade.....	146
Figure 8-3: Progressive application of the rotating motion to the fan blade	147
Figure 8-4: a) Stress distribution inside the fan blade obtained by G. Toussaint (5) using LS- Dyna. b) Stress distribution obtained in Abaqus	148
Figure 8-5: a) Assembly of the casing and the fan blade for the explicit analysis, b) definition of the boundary condition on the edges of the casing to fix it rigidly in space.....	149
Figure 8-6: Graphical evolution of the impact analysis of the fan blade on the hybrid casing .	152
Figure 8-7: Blade's velocity over the duration of the analysis	153
Figure 8-8: Energy curve of the blade's velocity over the duration of the analysis	154
Figure 8-9: Fan containment made of twenty four layers of aluminum	155
Figure 8-10: Analysis results for the 25-layer fan containment: (a) the blade has been stopped inside the containment, (b) graphical representation of the stresses at the end of the analysis.....	156
Figure 8-11: Blade's velocity over the duration of the analysis	157
Figure 8-12: The fan blade's velocity evolution or different configurations of the hybrid casing	158
Figure 8-13: Velocity evolution predictions of the fan blade for different configuration of the casing	159
Figure 8-14: Comparison of the blade velocity evolution for the twenty-five layer metallic casing and the thirty layer hybrid casing	160

Acknowledgements

I thank my Professor, Augustin, who gave me Knowledge

I thank my Mother who gave me Strength

I thank my Father who gave me Freedom

Dedication

I dedicate this modest memoir to Mankind and its achievements to which I want to contribute.

CHAPTER 1 - INTRODUCTION: DYNAMIC ANALYSIS OF FABRIC SYSTEMS

Because of their high resistance and lightweight, composite materials have naturally become very attractive for aerospace applications. Indeed, in this particular industry, in order to decrease the weight of flight vehicles and increase their energy efficiency, the demand is very high for more effective materials capable of replacing aluminum or steel structures used in airplane main structural components. Composites parts also have the advantage of having great design flexibility so they can be adapted to the loads they are designed to withstand. This particularity has greatly extended the field of their possible applications.

Because of the safety issues that drive the aerospace industry, composites were very slowly introduced even though it was widely recognized that they had a very high potential. As we can imagine, the need to gain confidence in a technology is crucial before implementing it in a commercial plane. In consequence, the use of these materials started in the early 1960 when they were first introduced in the manufacturing of aircraft “secondary” parts. As such they were meant to replace the traditional metallic parts of existing aircrafts and they served as a test to explore their inflight durability. This was the case of the DC-10 rudder, or the Lockheed L-1011

Tristar ailerons. At this time the weight reduction for these specific parts ranged from 20% to 25%.

Then, progressively, as the confidence in the design of these materials grew and as the manufacturing expertise became more solid, they were applied to “primary” (or structural) components such as the vertical stabilizer or the engine casing for example. Nowadays, composite materials are used by every commercial airplane manufacturer and the most recent large commercial airplane is the new Boeing 787 which is 50% composites.

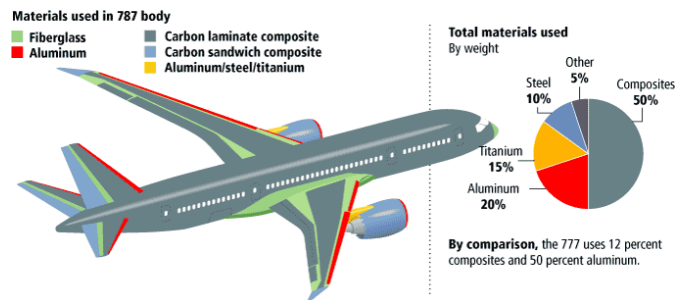


Figure 1-1: Composite materials in new Boeing 787 Dreamliner (bintang.site11.com)

As we can see in Figure 1-1 the whole fuselage is now made of composite which leads to tremendous gains in terms of weight of the structure. Also, it simplifies the structure because there is no longer a need to assemble the hundreds of metal sheets that used to constitute the skin in the fuselage.

Another example of the great confidence the industry has developed using these materials is the Airbus A380, largest commercial aircraft ever produced and for which the center wing box, linking the wings, is made of carbon fiber reinforced plastics (CFRP).

There is still great potential for the development of continuous fiber-reinforced composites to be used as load-bearing parts. New manufacturing techniques decrease the cost with short production cycle time and increased reproducibility by automation. This evolution leads to an ever increasing use of fabric reinforced plastics to obtain part with even more complex forms. These high performance applications are always in need of new ways to design composites and this is why the industry focused on textile reinforced composites.

1.1 Textile composites

Textile composites have textile reinforcement, constituted of continuous fibers that are arranged in a repetitive woven pattern. The interesting property of the fabric reinforcement lies in the fact that the stiffness and strength of the fabric depend not only on the yarns and matrix properties, but also on the composite material parameters (3). These parameters define the geometry of the fabric such as the fabric count specifying the number of yarns per inch, or the type of weave used determining how the warp and fill are interlaced, etc.

1.1.1 Composite under impact

In aeronautics, composite parts are exposed to high velocity impact, ranging from bird strikes on the wings leading edges to engine fan blade debris striking on the casing in case of a catastrophic failure, the examples are numerous. In order to address these issues, there is a great deal of studies and tests carried out on composite materials to study various textile composites behavior under impact as well as their deformation modes, damage and rupture.

We already know in theory that in the case of textile, the reinforcements are continuous yarns, that infer to the resulting composite a good impact and fatigue resistance but that the modeling of the impact resistance still raises some questions. There is still a great deal of work that remain to be done in order to fully understand and model all the phenomena that take place under such a dynamic loading (4).

1.1.2 Numerical impact modeling on textiles

The procedure used in the aerospace industry to achieve the certification of a certain aircraft component made of composite materials relies on the “building-block” approach. That approach implies that a large number of experimental tests are performed at each stage of the product development. This procedure of systematic testing is very costly and time consuming so the natural tendency is to substitute numerical testing to physical testing. The use of analytical and numerical models for the prediction of the mechanical behavior of composites structures can replace some tests, and as it evolves, it will take an ever growing place in the design and certifications processes.

But numerical testing needs models adapted to the specific phenomenon we want to analyze. It takes time to develop and validate such models before they can finally be used in the industry. Also, to further complicate the problem there are often different ways to model the same phenomenon, and each way has its specific capabilities and deficiencies we need to be aware of. As we can see, the amount of work is considerable. Even though several approaches have been proposed, but they can however be divided in two main categories: first the mesoscale models and then the macro-scale models.

Mesoscale models describe in details the structure of a textile unit cell using finite elements or analytical equations. These models use the theory of the physical phenomena and deformation mechanisms at the mesoscale level to predict the macro-scale behavior. Mesoscale models have the potential to avoid costly textile spending for the representative volume element (RUC) characterization and to virtually design multiple-ply systems (4). The RUC is the smallest repeatable geometrical unit of a fabric which characterizes the whole fabric structure.

Macroscale models are typically implemented in a non-linear finite element program to perform forming or impact simulations. These models are generally of elastic nature and consider a homogenized medium or a set of elements (truss, membrane, shell, etc...). They usually display behaviors as identified in fabric numerical tests with mesoscale models. Researchers have developed a continuum model for the mechanical behavior of woven fabrics in planar deformation to deal with the impact problem. The macroscopic behavior under impact is determined by deformation mechanisms at smaller scales. In order to perform simulations at acceptable numerical cost, a multi-scale material approach is applied such that the smaller length scale model predicts the mechanical behavior at the larger length scale.

This model can simulate simple existing plain weave fabrics but can also predict the behavior of novel fabrics provided that we have the geometrical properties of the yarns and the weave pattern defining the RUC. The approach relies on the selection of the geometric model for the fabric weave, coupled with constitutive models for the yarn behaviors.

1.2 Research objectives and methodology

1.2.1 Objectives

The main objective of this research theme is the study of the containment of engine debris inside the engine casing should a catastrophic malfunction of the engine occur. This naturally leads us to the study of the high velocity impact problem on composite fabrics using industrial FE software such as Abaqus.

The specificity of this work is that it consider a “dry” woven composite which means there is still the textile reinforcement made of fiber but there is no matrix. Indeed, for the confinement application, the textile acts as a net to prevent any debris from perforating the confining ring structure. Also, an in-house material model will be developed using facilities provided by an Abaqus user’s subroutine called VUMAT to apply it to shell elements mimicking the behavior of one fiber crossover. In the long term the study will provide a numeric testing answer to the question of how many plies of a specific type of fibers and weave do we need to have in order to contain a specific type of debris.

This numerical approach to composite fabric analysis is justified because as we have seen before, the use of composites will replace the actual metallic casing and save some weight while reducing the cost of physical testing because the same analysis will be done numerically.

1.2.2 Methodology

The methodology behind this work is as follows:

1. The development in Abaqus of a full blown 3D crossover. This is done by selecting the geometry we want to study and by modeling it inside the FE software. Applying displacements on the yarns of the representative volume element we are able to capture its behavior in specific modes of deformation.
2. Our second and most important task is to create the user material subroutine that will be used to model the behavior of the dry fabric. We based this VUMAT user subroutine development on the algorithm proposed by Shahkarami (2).
3. Using the 3D crossover specific geometrical and mechanical parameters the VUMAT user subroutine is tested the VUMAT by applying to one shell element in the same

modes of deformation that was used in the 3D model. This will enable to verify and validate the response given by the shell element.

4. Once the tests on a single shell element have proven successful, the subroutine is then applied to an impact analysis involving several elements. A dry fabric plate is thus modeled and its behavior under impact is observed and recorded. This is first done on a single ply fabric and then on a 4-ply fabric structure. Throughout this thesis Shahkarami's work is used to validate our model since he was able to perform the physical experiments and to present data against which our own results could be tested.
5. The last part of this work is the modeling of the impact of fan blade debris on an engine casing. This is a pretty interesting work since it involves several modeling techniques with Abaqus FE software that were not yet explored in our laboratory. The casing was made of an inner metallic ring around which composite plies are wrapped.

1.3 Outline of the thesis

This thesis consists of eight chapters that provide the necessary background knowledge on textile composite reinforcements (Chapter 2), the literature review (Chapter 3), the necessary numerical tools needed in the work (Chapter 4), the detailed modeling of the 3D crossover (Chapter 5), the development, verification and validation of the VUMAT user subroutine that was designed (Chapter 6 and 7) and finally the modeling of the impact of a fan blade containment study by an hybrid engine casing which is the goal of this study (Chapter 8).

Chapter 2 presents an overview of textile reinforced composite materials. Starting with the most elementary constituents of a composite material we present the characteristics of fibers and the way they are assembled to form the yarns. Then, we discuss the geometrical configuration of different types of weave patterns and their specific mechanical properties. Also, the definition of the representative volume element (RVE) is presented since it is a crucial concept at the basis of this work. The mechanical phenomena observed during experimentation and taking place in the plain weave during deformation are discussed. This gives us the best understanding of the physics at the microscopic and mesoscopic scales that ultimately define the behavior of textile reinforcements at a macroscopic scale.

Chapter 3 constitutes the literature review. We briefly talk about the evolution of composite modeling and the different types of modeling techniques that have been developed by various researchers. In this chapter we outline the basic principles of their work and point out the good as well as the less interesting aspects of each technique.

Chapter 4 presents all the tools that are necessary to understand in order to conduct this work. Of course, the shell element theory will be briefly discussed outlining the main features and characteristics of the shell element that was used. In the case of the 4-ply fabric impact, a contact definition between plies that is suited for high velocity impacts in Abaqus that was used is also described. The dynamic and explicit formulation codes are also overviewed since they are constantly used throughout this work. Abaqus documentation is extensive on these subjects but we will extract the main ideas that helped us while working on the analysis. VUMAT user subroutine description is also presented in great details. Using that particular subroutine inside Abaqus some very specific guidelines must be followed in order to handle the computations and return the results to Abaqus FE engine. Finally, our work on the subroutine involved the use of the Newton-Raphson optimization routine at the heart of the VUMAT and thus we think it is important to summarize the basic knowledge we acquired with it.

Chapter 5 deals with the modeling of the crossover in 3D using Abaqus. The geometry representing the crossover as well as mechanical properties to define the yarns' material are first chosen. Then, the virtual testing of the crossover is described extensively from the definition of boundary conditions to the applied displacement on the yarns' edges. The goal in this chapter is to define a crossover model from which we can extract mechanical properties and all the necessary parameters to be used in the material subroutine. The crossover was tested in biaxial tension, uniaxial tension, shear and transverse compression.

Chapter 6 is concerned with the development of the VUMAT used with the shell element. The subroutine is simply the representation of a complex yarn geometry using a trellis mechanism. Simplifying assumptions are discussed as well as the complete procedure of computations taking place inside the subroutine. The VUMAT is essentially a procedure using constitutive relations to model the behavior of the crossover under specific in plane loadings. Also in this

chapter the testing of the subroutine on one single shell element is described and the obtained results are compared to observation and analysis.

Chapter 7 presents the modelling of the impact problem in Abaqus. The geometry of the problem is described as well as the features we used like element deletion and surface interactions. Analysis was created for the impact study on a 1-ply, 2-ply and finally 4-ply fabric. The influence of several parameters is studied to see whether or not their variation impacted the results of the analysis. Finally we tested our results against the results obtained by Shahkarmi (2).

Chapter 8 explains all the necessary steps required for modelling the impact of a fan blade debris on a hybrid engine casing. As in chapter 7 the specific modelling techniques that have been used for the successful creation of this analysis are presented. The results that we were able to obtain are presented and their validity is discussed using the work of previous graduate students (5) who modeled the same impact problem on an engine casing made of aluminum and dry woven composite.

Finally, a summary of the work done and of the findings of this thesis along with the conclusions that can be drawn from them are presented. Moreover some propositions aimed at further improving and refining the designed VUMAT model and the modeling approach are also suggested.

CHAPTER 2 - OVERVIEW ON TEXTILE COMPOSITES

The mechanics of textiles composites can be studied better by understanding the multiple levels of their design and hierarchical organization. There are four levels of organization, from small scale to relatively large scale:

1. Fiber
2. Yarn
3. Textile
4. Composite

We will now discuss these four levels in details.

2.1 Fibers in textile composites

The choice of fibers represents the first step in the manufacturing of a textile composite. There exists a wide choice of fibers and each type has specific material properties depending on their internal structure. Today, the industry has created many types of fibers capable of reinforcing any class of materials either metals, plastics or ceramics.

To resist high loads in structural applications, textile structural composites products must be made from high modulus fibers like glass, graphite, Aramid or Kevlar for example. Other types of fiber like ceramic or steel fibers can also be found but they are rarely used for aeronautical applications and therefore we will not discuss them in details.

2.1.1 Glass fibers

Glass fibers represent more than 99% in mass of the reinforcement used in the industry of composites. They are made from the most part of silicium which has a fusion temperature of 1700°C, this temperature does not allow the use of a threading die because of the lack of material that can resist it. This is why silicium is combined with other elements such as sodium, magnesium oxide or potassium oxide to better control the temperature which is lowered to 1200°C. Other elements such as alumina (Al_2O_3) are employed to stabilize the glass structure and modify its physical properties (6).

There are five types of glass fibers and each has its specific properties suited for different applications. E-type glass is the most commonly used and its Young modulus is similar to aluminum. S-type and R-type contain more alumina and therefore have higher mechanical properties than the E-type; they are used for advanced structural composites. C-type glass is especially resistant to corrosion and D-type has been developed for application in which dielectric properties are important (6).

Glass fibers usually have a diameter ranging from 5 μm to 15 μm . These fibers have less superficial flaws than massive glass and therefore have a much better resistance to failure; they display an elastic behavior in tension and a brittle failure.

2.1.2 Carbon fibers

Carbon has the strongest covalent link in nature, but carbon atoms can be organized in different ways such as graphite, diamond or other forms. Graphite displays a very peculiar micro-structural anisotropic organization which is formed by successive planes distant of 0.34 nm from one another. Carbon fiber is very strong when stretched or bent, but weak when compressed or exposed to high shock (a carbon fiber bar is extremely difficult to bend, but will

crack easily if hit with a hammer). Carbon fibers are used in composites with a lightweight matrix. Carbon fiber composites are ideally suited to applications where strength, stiffness, lower weight, and outstanding fatigue characteristics are critical requirements. That kind of structure is found in very high modulus graphite fibers (6).

Most carbon fibers are manufactured using a process designed in England and Japan in 1960. An acrylic polymer made of 49% carbon called polyacrylonitril (PAN), is heated to 1000°C to obtain a fiber which is 93% carbon in mass. During pyrolysis the fiber must be kept under tension so that the molecular structure is oriented. Between 1500°C and 1600°C the fiber become 100% carbon and its resistance reaches a maximum, if it continues to be heated, the mechanical resistance will decrease and Young modulus will increase. The three stages process is illustrated in the next figure and comprises of: (i) Oxidative stabilization, (ii) carbonization and (iii) graphitization (graphitization process between 1500^o and 3000^oC).

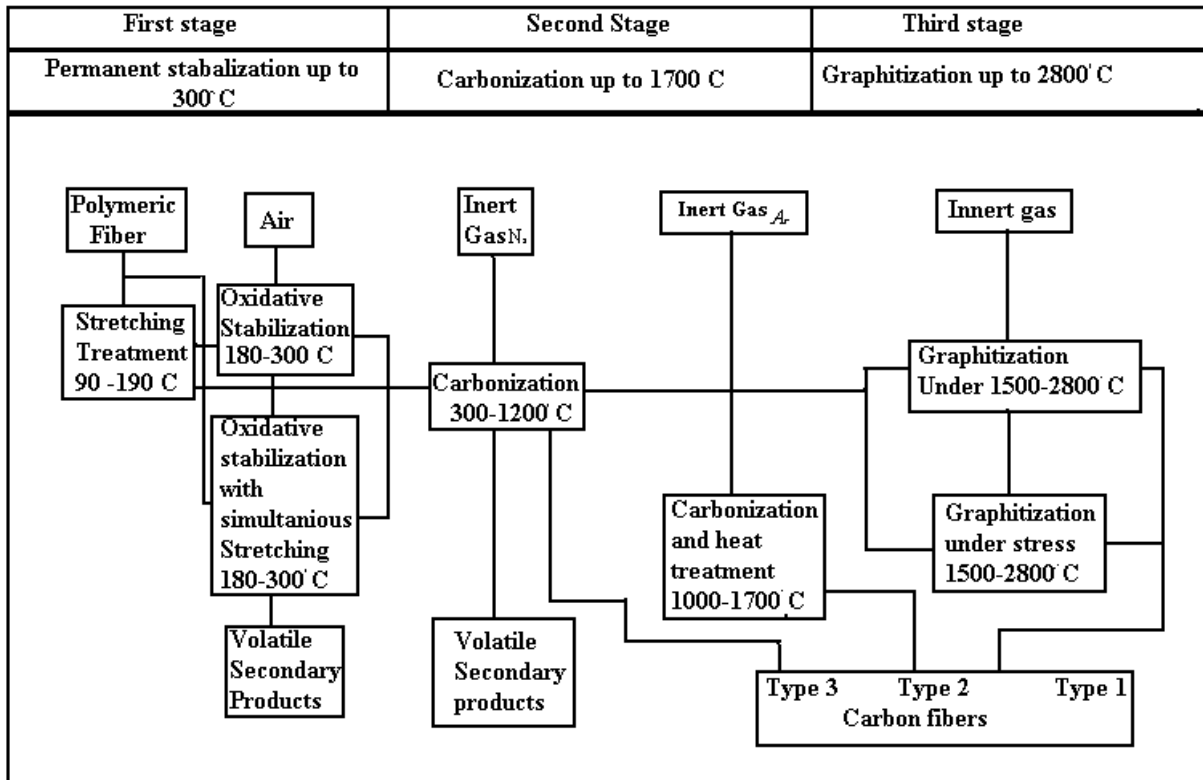


Figure 2-1: Schematic representation of carbon fiber preparation from PAN fibers (6)

In Table 2-1 we enumerate the various advantages of carbon fibers and give examples of their application.

Table 2-1: Characteristics and Applications of Carbon Fibers (6)

Physical strength, specific toughness, light weight	Aerospace, road and marine transport, sporting goods
High dimensional stability, low coefficient of thermal expansion, and low abrasion	Missiles, aircraft brakes, aerospace antenna and support structure, large telescopes, optical benches, waveguides for stable high-frequency (GHz) precision measurement frames
Good vibration damping, strength, and toughness	Audio equipment, loudspeakers for Hi-fi equipment, pickup arms, robot arms
Electrical conductivity	Automobile hoods, novel tooling, casings and bases for electronic equipments, EMI and RF shielding, brushes
Biological inertness and x-ray permeability	Medical applications in prostheses, surgery and x-ray equipment, implants, tendon/ligament repair
Fatigue resistance, self-lubrication, high damping	Textile machinery, general engineering
Chemical inertness, high corrosion resistance	Chemical industry; nuclear field; valves, seals, and pump components in process plants
Electromagnetic properties	Large generator retaining rings, radiological equipment

2.1.3 Organic fibers

There are many types of organic fibers made throughout the world. The Nomex fiber was industrialized in 1960, the presence in its structure of Aramid molecules leads to a higher fusion temperature than polyamide fibers. Nomex fibers are used to manufacture some secondary part in the aeronautic industry because it doesn't have a high modulus and thus can't be used for structural applications (6).

Another configuration of aramid molecules is used to produce Kevlar fibers which were introduced in 1972 in the United States (6). They are made of highly oriented chains of poly-

paraphenylene terephthalamide molecules with strong inter-chain bonding. Their internal structure gives the resulting fiber very good thermal properties and also a very high modulus while being a very light material that makes it a material of choice in a variety of applications. Also, in the principal direction, chemical bonding is very strong whereas in other perpendicular directions Van der Waals bonds are a lot weaker and this explains why these fibers cannot be used in structural application to supports loads in directions other than the principal direction of the fiber (6).

One of the highest Young modulus we can find for these types of fibers is 280 GPa obtained in Zylon fibers. Organic fibers have a diameter ranging from 12 μm to approximately 30 μm (6).

2.2 Yarns types

The second step of the manufacturing process consists of grouping together the fibers in a linear assemblage to form a continuous tubular structure from called a yarn. Also, to hold the fibers together, they are impregnated with resin. There exist various yarn structures, each having different properties suited for various types of applications. Yarns may be composed of one or more continuous fibers, discontinuous chopped fibers and finally, two or more single yarns can be twisted together to form plied yarns. In the traditional textile industry, the filaments are twisted to provide good structural integrity and the ability to hold the shape. In contrast, in the forming of structural composites a softer yarn is desirable since it allows greater compaction and flattening and therefore greater total volume fraction of the fibers in the resulting composite, thus increasing its strength (6).

In this study, we will be concerned with multiple, continuous, untwisted fibers because they are simpler to study and because their mechanical properties are very close to the monofilament properties. Also, for structural composites the twisting of the filaments would reduce the axial stiffness of the yarns which is one of the most important properties we are looking for in a yarn.

The yarn's structure is characterized by several geometrical parameters which are (6):

- The number of filaments,
- The cross-sectional area (we will assume they have an elliptic shape),

- The yarn packing density, defined as the ratio of the fiber volume to the yarn overall volume.

Yarn structure plays a dominant role in the translation of fiber properties into various yarn properties. First, the mechanical properties of the yarns are mainly dictated by the fiber obliquity, which is the orientation of the filament relative to the yarn axis. Second, the way fibers are grouped together, called the fiber entanglement is also a very important consideration. An assemblage of chopped fibers is not as strong as a yarn made of untwisted monofilament. Typical filament to yarn strength translation efficiency in the previously presented yarn structures are listed in Table 2-2 (6).

Table 2-2: Geometrical parameters of the RVE to be defined in Abaqus

Yarn structure	Strength translation efficiency
Monofilament	100%
Multifilament: untwisted	98%
Multifilament: slightly twisted	95%
Multifilament: air jet texturized	85%
Multifilament: stretch texturized	85%

2.3 Fabric structure

The third step in textile structural composites manufacturing process consists in interlacing the yarns in a periodic configuration to form a flat sheet with a specific weave pattern. Fabric types are categorized by the orientation of the yarns and the weave pattern used to hold the yarns together. Three common fabric structures are shown in Figure 2-2. A weave pattern is defined by its representative volume element (RVE) which is its smallest repeating unit. Thus giving the description of the RVE is sufficient to describe the complete structure of a textile composite reinforcement. Among the family of textile reinforcements for composite materials the principal types of fabrics are detailed in following subsections (7).

2.3.1 Woven

Woven are produced by interlacing yarns in orthogonal directions. The warp yarn (0°) is interlaced in a rectangular pattern with the fill yarn (90°). The fabric integrity is maintained by

the mechanical interlocking of the crossing yarns. Drapability over a complex surface, surface smoothness and deformation stability of the fabric are controlled primarily by the weave style.

2.3.1.1 Plain weave (7)

Each warp yarn passes alternately under and over each fill yarn. The fabric is symmetrical, with good stability and reasonable porosity. However, it is the most difficult of the weaves to drape, and the high level of yarn crimp imparts relatively low mechanical properties compared with the other weave styles. With large yarns, this weave style gives excessive crimp and therefore it tends not to be used for very heavy fabrics.

2.3.1.2 Twill weave (7)

One or more warp yarns alternately weave over and under two or more fill yarns in a regular repeated manner. This produces the visual effect of a straight or broken diagonal 'rib' to the fabric. Superior wet out and drape is seen in the twill weave over the plain weave with only a small reduction in stability. With reduced crimp, the fabric also has a smoother surface and slightly higher mechanical properties.

2.3.1.3 Satin weave (7)

Satin weaves are fundamentally twill weaves modified to produce fewer intersections of warp and fill. The 'harness' number used in the designation (typically 4, 5 and 8) is the total number of yarns crossed and passed under, before the yarns repeats the pattern. Satin weaves are very flat, have good wet out and a high degree of drapability. The low crimp gives good mechanical properties. Satin weaves allow yarns to be woven in the closest proximity and can produce fabrics with a close "tight" weave. However, this weave displays low stability and its asymmetric nature needs to be considered. Bending and stretching in a satin weave ply are coupled because of exchange sites breaking symmetry and causing yarns to bend in an asymmetric way. Coupling between those two phenomenon will cause warping during cure because of thermal strains. Care must be taken in assembling multiple layers of these fabrics to ensure that stresses are not built into the component through this asymmetric effect.

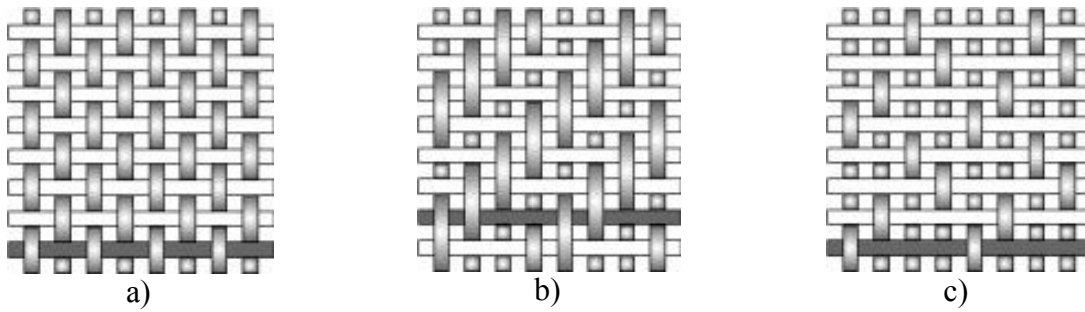


Figure 2-2: Representation of various weave patterns for textile reinforcements: plain weave a), twill weave b) and satin weave c) (7)

2.3.2 Other types of fabrics

2.3.2.1 Non crimp fabrics (7)

This type of fabric has a very low crimp of the yarns in each lamina. Yarns are ideally straight and each ply is arranged in various orientations best suited to support the loadings, this enable the designed part to fully exploit the yarn modulus. Each individual ply is then stitched together to optimize interlaminar bonds and thus reduce delamination. In consequence, the combination of unidirectional placement of yarns in multiple loading directions with consolidation by stitching leads to highly advantageous combination of properties. A visual example of such fabrics is shown in Figure 2-3.

Composite components of non crimp fabrics make it possible to ideally transmit the forces that arise in the stress direction using targeted fiber alignment. This makes reduced component weight despite identical mechanical values or higher loads for the same component weight compared to woven fabrics while displaying of low production costs.

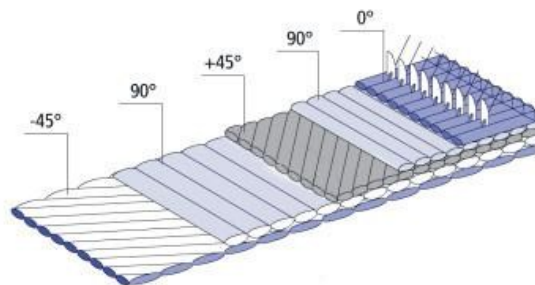


Figure 2-3: Non crimp fabric constituted of an assemblage of unidirectional plies stitched together (3)

2.3.2.2 3D Fabrics (7)

When the thickness of a composite part is large, the use of laminated composites is restricted by manufacturing problems and low out-of-plane resistance causing delamination. These problems have been solved by the design of the 3D fabric architecture which is presented in Figure 2-4. There are no yarns set in the transverse direction but through the thickness properties are very much improved. These reinforcements have significant applications in military hardware and are also used today to manufacture the fan blade of GE90 turbojet engine.

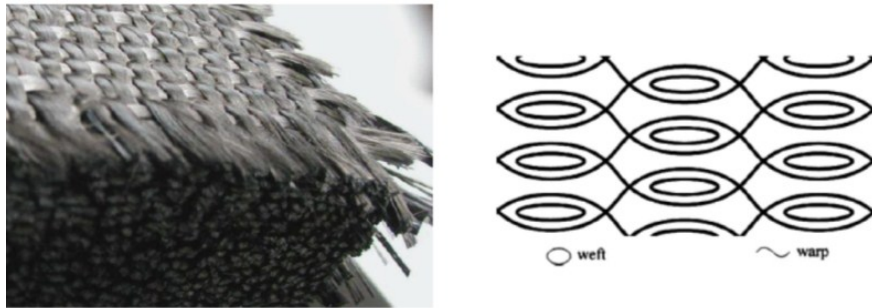


Figure 2-4: 3D fabric reinforcement (3)

2.4 Multi-scale nature of composite materials

As we already know, composite materials are usually composed of reinforcements and a matrix that hold the reinforcement in place. In the case of textiles, these reinforcements are an assemblage of yarns in a specific weave pattern and the yarns are constituted of filaments. Thus the overall composite inherits the properties of the filaments composing the yarns and also taking into account the specific pattern in which the yarns are organized. During an impact loading, the yarns undergo extension in their principal axis as well as small in-plane rotations; it is then important to characterize each of the phenomena taking place at a mesoscale level during an impact to assess the behavior of the composite under such loadings.

As we have seen before, composites are by definition multi-scale materials. We may distinguish three levels to investigate the mechanical response of the textile reinforcements during deformation. These scales have been studied in details and are used by many different researchers and hold their own significance; they are presented here in order of decreasing size.

Macroscopic scale is considered the level of the whole part at which we study the phenomenon, in our case it is the impact. It covers the dimensions from a few centimeters to decimeters and even meters. The models developed usually consider a simple equivalent media like a set of elements. The behavior at this level is highly dependent on the possible motions and interactions of yarns at the mesoscopic level; it is therefore determined by the deformation mechanisms at smaller scales. In the following pages we will go over the deformation mechanisms we have to understand fully before any work is done at the macro-scale.

Mesoscopic scale consists of yarns made of a few thousand of filaments; this scale is focused on the representative volume element of the fabric which is repeated continuously to make the fabric. Thus it is used to study on crossover and the yarn-yarn interactions. Finite element (FE) modeling of the textile at mesoscale level aims at determining the maximum details of both the reinforcement geometry and the stress-strain state. FE at this level is used to mesh a realistic geometrical model of the reinforcement internal geometry which represents actual volumes of the yarns. An example of the typical studied geometry and mesh is given in Figure 2-5.

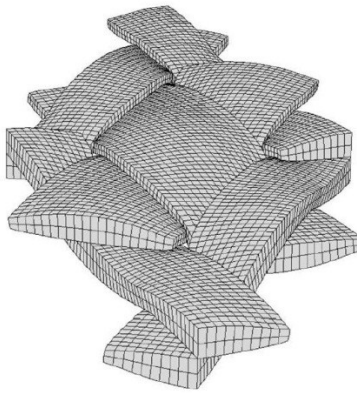


Figure 2-5: Deformed geometry of RUC at mesoscale level in plane shear (8)

In an FE model of this nature, the geometry and yarn properties are usually imported from a textile pre-processing program to generate the solid mesh. Typical studies have been conducted conjointly by Badel, Vidal-Salle and Boisse (8) and also Lomov et al. (9). Due to the large number of elements in these models, they require large CPU time (1).

Microscopic scale is the smallest of the three levels at which the textile reinforcements are studied. This scale is confined to the yarns and their composing filaments which diameters

ranging from approximately 5 μm to 50 μm . There exist some modeling studies at this scale by Durville (10), Vandeurzen (11) and Zhou (12) and the main problem is the very large number of contact elements which demand very large CPU time.

Because of the specific multi-scale nature of the textile reinforcements, different approaches have been developed to model the impact problem. These approaches exploit the three different scales presented above from a geometrical, analytical, or FE modeling perspective. We will discuss in greater details the work done on each of these approaches in chapter 3. The focus here is to present the specificities of the geometries, mechanical properties and deformation modes of fabrics; these concepts are crucial to the understanding of the modeling approaches to be adopted.

2.4.1 Observation of the fabric architecture

Many pictures of the textile structure are available throughout the literature. As part of our study we will start focusing on the plain weave as shown in Figure 2-6 taken from ref (13).

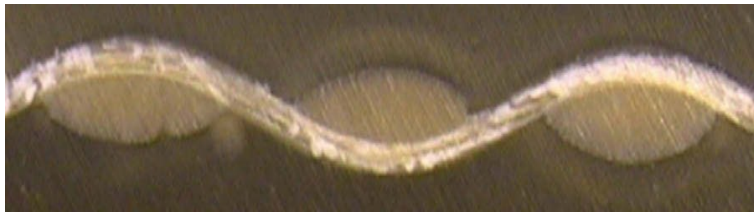


Figure 2-6: Microscale image of a plain weave showing the undulation of the yarns and their cross-sectional shape (13)

2.5 Mechanical properties of textiles reinforcements

Several deformation mechanisms take place inside the fabric and we will provide a summary of the main ones in the following paragraphs. Not every one of the following mechanisms will be taken into account in the user material subroutine to be presented later, but it is important to understand them if the subroutine is to be improved in further work by adding some of the mechanisms to better model the behavior of the fabric.

2.5.1 Deformation modes in the fabrics architecture (1)

There are two main types of deformation modes that will be briefly described here: in-plane deformations and out-of-plane deformations. In-plane deformations are caused by uniaxial and biaxial yarn extension and shear. Out-of-plane deformation is typically caused by transverse compaction of the yarns, bending etc.

2.5.1.1 Elongation in yarn principal direction (1)

When applying a load in the direction of the yarns, the fabric is being elongated in that direction. That elongation is usually very small and is attributed to the straightening of the yarns from their crimped initial state. This straightening may be caused by high deformation energies as it can be seen in figure 2-9.

2.5.1.2 In-plane shear (1)

Because of the weave pattern that is being used, large rotations of the warp and fill yarns are possible. They appear at the crossover points between the two perpendicular yarns because of the shearing effect. Indeed shearing is the principal in-plane deformation mechanism and the relative yarn rotation can be large even for small shearing loadings. Yarn rotation is happening until the angle between the yarns reaches the locking angle; at this point the fibers cannot freely rotate anymore as shown in Figure 2-7 taken from ref. (1).

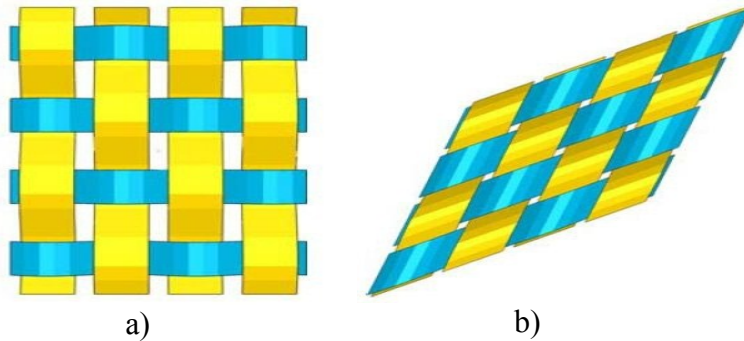


Figure 2-7: Fabric in uniaxial tensile deformation a) and in shear deformation b) (1)

2.5.1.3 Compression in yarn principal direction (1)

When the fabric is submitted to compressive load in the principal direction of either warp or fill yarns then buckling appears almost immediately. The yarns have a very poor compressive strength, thus the fabric also has very low compression properties.

2.5.1.4 Transverse compression (1)

When transverse compressive loads are applied to the fabric there is a flattening effect happening at the crossover points. The yarns are being compressed between one another and the cross-sectional area of each yarn is reducing, this is due to the fact that the filaments at the micro-scale level are being jammed against each other. It is important to mention at this point that the transverse compression of the ply is affecting its in-plane tensile and shear behavior since the contact areas between the fibers are increased by the compression load (1).

2.5.1.5 Bending (4)

A fabric's resistance in bending is very low because of the small cross-section of each yarn able to bear the load and also because of the sliding between warp and fill yarns. This very low bending resistance is interesting in the case of composite forming processes and often, in numerical analysis, the textile ply is modeled as a membrane element. However in some fabrics, the resistance in bending is not low enough to be considered negligible and in that case shell elements are used.

2.5.1.6 Locking (4)

The locking phenomenon happens when the in-plane shear of the fabric has brought the fabric in a situation where the angle between warp and fill yarns is less or equal the locking angle. At this point if the shear strain continues to grow over time, there will be a lateral compression of warp or fill yarns by the surrounding adjacent yarns. This causes a change in the yarns cross-sectional areas which in turn will change the mechanical properties of the whole fabric.

2.5.1.7 Cross-locking (4)

Cross-locking is a result of changes in the undulations of the yarns. For example, during biaxial tensile loadings, the yarns straighten and de-crimp and the jamming of warp and fill yarns against each other at the crossover leads to a cross-locking. In that situation, neither family of fibers is completely straighten and no matter how high the tensile load is, the yarns will stay undulated because of the locking at the crossover points.

2.5.2 Mechanical behavior of composites under various loadings

2.5.2.1 Behavior in biaxial tension (4)

Tensile tests on different types of fabrics in warp and fill directions have shown that the fabric has a non-linear behavior in tension. This behavior is especially non-linear at the beginning of the test where low tensions are applied but generate a relatively high deformation. There is a progressive stiffening taking place at first, followed by a linear response corresponding to the behavior of straightened yarns as shown in Figure 2-8.

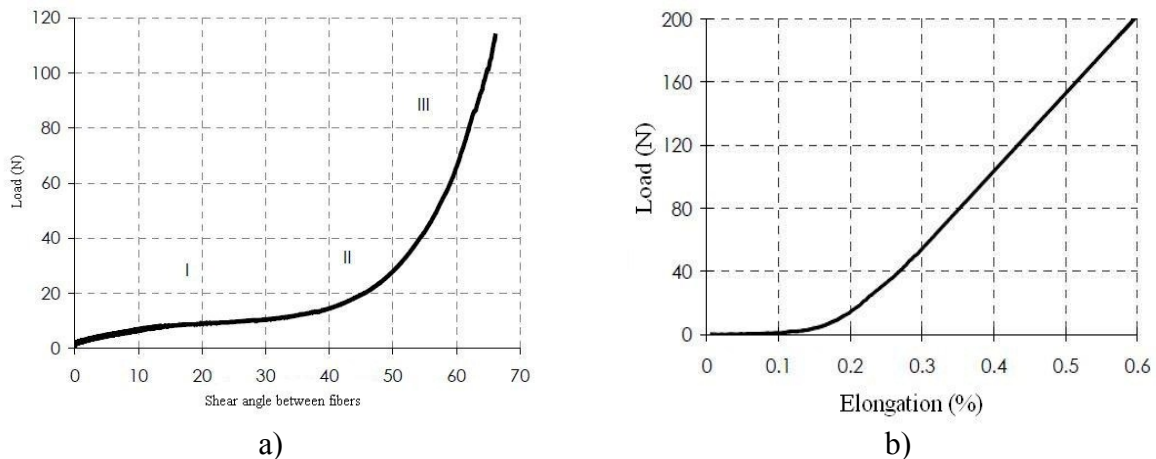


Figure 2-8: Response of characterizing loads on a plain weave fabric: shear response a) and tensile response b) (14)

The observed non-linearity is a consequence of the weave pattern which gives the yarns a natural tendency to undulate as they pass over and under the crossing yarns. Under tensile loading, the yarns progressively straighten and then elongate. In the case where warp yarns are submitted to loading while fill yarns are free, the warp yarns become totally straight and the fill yarns get more undulated.



Figure 2-9: Straightening of the yarns in case of uniaxial tension (14)

In other cases of combined loadings in the two main fabric directions, neither one yarn family nor the other is entirely straightened. In that case, the fabric achieves an equilibrium state. Thus

it appears clearly that the fill and warp yarns are interacting with each other throughout a uniaxial or biaxial tensile load.

In consequence, the non-linearity at the beginning of the loading process is due to geometrical considerations that can be seen at the scale of the representative volume element. It is caused by the change in the yarns undulations. Other phenomena also take place at the mesoscale level (4). First, under tensile loading, the cross-section of the yarns is reduced because of the elongation taking place. Second, yarns are transversally compressed against each other at the crossover points, yarns rearrange and this also has an effect on the yarns' sections.

2.5.2.2 In-plane shear behavior

Shear tests on textile reinforcement have shown that the fabric have a non-linear shear behavior which is characterized by three distinct and successive steps. The first step corresponds to a linear behavior characterized by a very low stiffness. The second step is where the non-linear behavior happens; it corresponds to progressive stiffening. Finally, the third step is an almost linear behavior with a relatively high stiffness compared to the two preceding steps. Shearing leads to rotations between the two yarn families, these rotations generate friction at crossovers between the yarns. Thus the low initial stiffness of step one is attributed to the initial friction happening at each crossover point during the rotation of the yarns (4).

The non-linear part corresponds to the progressive jamming of adjacent yarns when the voids between the yarns are progressively closed. When all the voids are being closed up, the fabric is considered in the locked state meaning it will no longer continue its shearing deformation in the plane. The quasi-linear phase in step 3 shows a very high shearing stiffness, this rises from the fact that the shearing deformation is limited because of the lateral compressibility of the yarns. In that particular zone, if the shearing loads continue to be applied the fabric will start showing wrinkles which really are out-of-plane deformations.

The non-linear behavior of the fabric in shearing observed at a macro-scale level rises from geometrical changes in the fabric at a mesoscale level. Important variations in the yarns placement, relative position, orientation and geometry are happening. Figure 2-10 shows the shearing effect causing a modification of yarn relative position from initial configuration shown

in Figure 2-10-a to final configuration shown in Figure 2-10-b; also there is an important change in the yarns cross-sectional area due to the lateral compression that occurs.

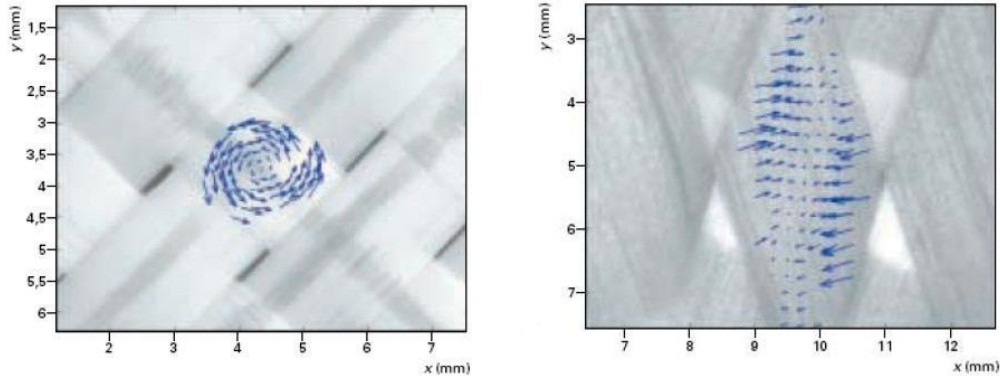


Figure 2-10 Shearing effects taking place at the mesoscale level at crossover where the yarns interact: a) initial configuration, yarn undeformed b) final configuration, yarn deformed (15)

The phenomena taking place at a mesoscale level are complex and much work has been done to capture their effects as we will see in chapter 3.

2.6 Conclusion

In this chapter, we went over the basics of fabric reinforced composites from their application to their constituents and various structure types. We mainly focused on the multi-scale nature of fabrics to get a clear understanding of the challenges we had to face at each level and fully grasp the importance of positioning our study at the right scale to capture the right deformation effects. Then, we overviewed and explained each phenomenon taking place in the fabric during its deformation such as yarn elongation, in-plane shear, bending, locking, transverse compression etc. Lastly, we tried to understand the basic behavior of a fabric under tensile and shear loads to get familiar with that type of loading and the deformations they lead to.

CHAPTER 3 - MODELING BALLISTIC FABRICS

Modeling woven fabrics is challenging due to the need to capture the fabric response at both the macroscopic scale of the fabric and the “mesoscale” of the yarns that compose the weave. In order to capture the dynamic behavior of fabrics, various modeling techniques have been developed and in this chapter we will present an extensive literature review of the different types of modeling approaches. Emphasis has been put on the unit-cell approach since it is the type of model that has been developed in this work and tested under impact loading using Abaqus.

3.1 Overview of ballistic fabric modeling techniques

Among the main computational analysis methods used to model ballistic fabric behavior, four main classes can be identified.

3.1.1 Finite-element analyses based on the use of pin-jointed orthogonal bars

The most notable studies in this category of analyses are those performed by Roylance and Wang (16), Shim et al. (17), Lim et al. (18), Shahkarami et al. (4). While the pin-jointed

orthogonal-bars based finite-element analyses have proven to be very efficient in approximating the dynamic behavior of woven fabrics, the discrete nature of the yarn models was associated with inherent oversimplifications that significantly limited the predictive capability of the analyses. In particular, important contributions associated with the weave architecture, surface-finish and friction governed yarn-to-yarn and layer-to-layer contacts (in multi-layer fabrics) could not be accounted for.

3.1.2 Detailed full-blown 3D continuum

Analyses using this method have been carried out by Shockey et al. (19), Duan et al. (20). While these analyses have proven to be powerful tools for capturing and elucidating the detailed dynamic response of single layer fabrics, they are computationally very demanding when applied to practical armor or engine containment casing systems which typically contains 30 to 50 fabric layers/plies.

3.1.3 Unit-cell based approach

This approach has been used extensively in order to derive the equivalent (smeared) continuum-level (membrane/shell) material models of textile composites from the knowledge of the mesoscale fiber and yarn properties, fabric architecture, and inter-yarn and inter-ply frictional characteristics. Among the most notable studies based on these analyses are those carried out by Kawabata et al. (21) who introduced simple analytical models to capture the uniaxial, biaxial and shear behavior of fabrics. Furthermore, Ivanov and Tabiei (22) proposed a micro-mechanical material model for a woven fabric (in which a visco-elastic constitutive model was used to represent the mechanical behavior of the yarns) for the use in non-linear finite-element impact simulations. In deriving the material model, Ivanov and Tabiei (22) considered the motion of the yarn-crossover point and developed a procedure for determining the equilibrium position of this point under the applied unit-cell strains. Recently, King et al. (23) proposed a new approach for deriving the continuum-level material model for fabrics based on the properties of the yarns and the weave architecture which involves the use of an energy minimization technique to establish the relationship between the configurations of the fabric structure to the microscopic deformation of fabric components. Similar unit-cell based

continuum-level membrane/shell material models have been developed by Boisse et al. (24) and Peng and Cao (25). Also, Shahkarami and Vaziri (2) proposed a similar but simpler model to that introduced by King et al. (23) and provided a detailed account of its incorporation into a material-model subroutine which can be readily coupled with commercial dynamic-explicit finite-element codes.

3.1.4 Higher-order membrane/shell

This approach is used to represent the dynamic response of fabric under ballistic loading conditions and overcome the aforementioned computational cost associated with the use of full 3D finite element analyses of the yarn/fabric structure. Among the studies falling into this category, the most notable is the one carried out by Scott and Yen (26). While the use of higher order membrane elements was found to be indeed advantageous computationally, it was never fully validated by comparing its results against either those obtained experimentally or those obtained using full 3D finite element analyses.

3.2 Analytical based modeling for the unit-cell method

Four main approaches using the unit-cell method may be encountered in the literature:

- The mesostructurally based analytical models proposed and refined by Pierce (27), Bejan and Poterasu (28), Warren and Sagar et al. (13).
- The simple analytical models first introduced by Kawabata (21) is introduced to capture the uniaxial, biaxial and shear behavior of fabrics while reducing the complexity of geometry description of the mesostructural models
- The micro-mechanical material model for a woven fabric proposed by Ivanov and Tabiei (22) in which a visco-elastic constitutive model was used to represent the mechanical behavior of the yarns. This material model has been used in non-linear finite-element impact simulations.

- A novel approach for unit cell continuum-level material model for fabrics based on the properties of the yarns and the weave architecture proposed by King et al. (23) and further improved by Shahkarami and Vaziri (2), Grujicic et al. (1).

3.2.1 Meso-structurally based analytical models

These models use mathematical equations to describe the geometry of a representative volume element of the fabric and to predict the mechanical response of the fabric and its components in specific modes of deformation. Such models can be valid only for uniaxial or biaxial tension of the fabric along the warp or fill family of directions, rotations and thus shear effects between yarns are not considered, hence the models are very limited in their predictions. The advantage of a meso-structural model can be used to quantify the homogenized material properties that will be used in continuum models.

In 1937, Peirce (27) proposed a model that provides the mathematical framework to describe the geometrical configuration of plain weave fabric having circular yarns. He based his description on the assumption that a yarn can be decomposed into undulated portions and straight portions as one can see in Figure 3-1.

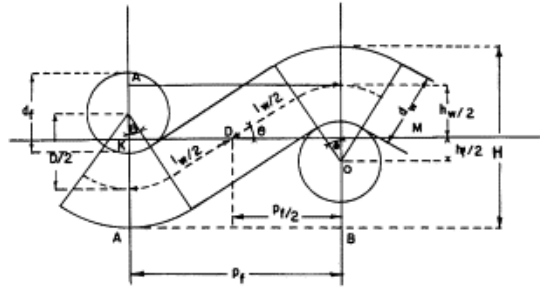


Figure 3-1: Geometry proposed by Peirce (27)

This model was the starting point used by many researchers to develop their own models taking into account further refinements like yarns with non-circular deformable cross sections.

To further present the process of describing the geometry of the lamina configuration we have taken the works of Liliana Bejan and V. F. Poterasu (28) as an example. Their work is restricted

to a two dimensional orthogonal balanced weave fabric. It features an idealized representation of a plain weave fabric lamina which is presented in Figure 3-2.

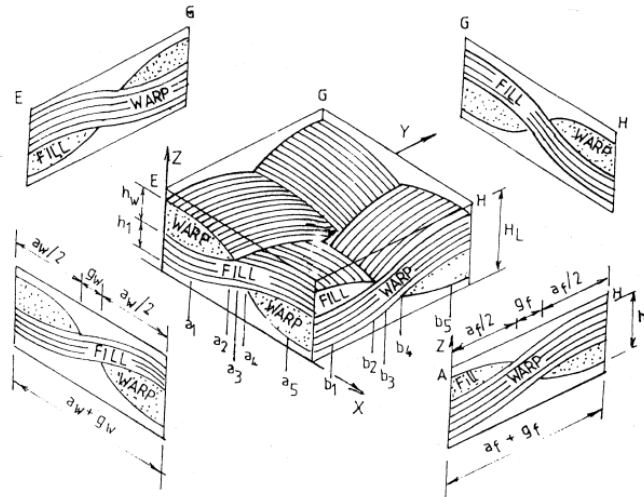


Figure 3-2: Geometrical representation of the plain weave fabric unit-cell used by Bejan and Poterasu (28)

From the macro-scale to a micro-scale, the unit cell consists of the interlacing region and of the gap region and then the interlacing region consists of the warp and fill yarns one over the other. The geometrical parameters chosen and used to describe this unit-cell are as follows:

- a_w (a_f) is the yarn width,
- h_w (h_f) the yarn thickness,
- g_w (g_f) the interyarn gap,
- u_w (u_f) the undulated length,
- h_t the fabric thickness, and h the lamina thickness.

Depending on the side from which you observe the representative unit cell, the authors have described two types of sections: sections E-A and sections A-H (they are presented graphically in Figure 3-3). This is to define the different zones used to describe the undulation of the yarns. Section E-A, for example, is divided into different zones marked by a_1 to a_5 . Similarly, the sections parallel to A-H are divided into different zones marked by b_1 to b_5 .

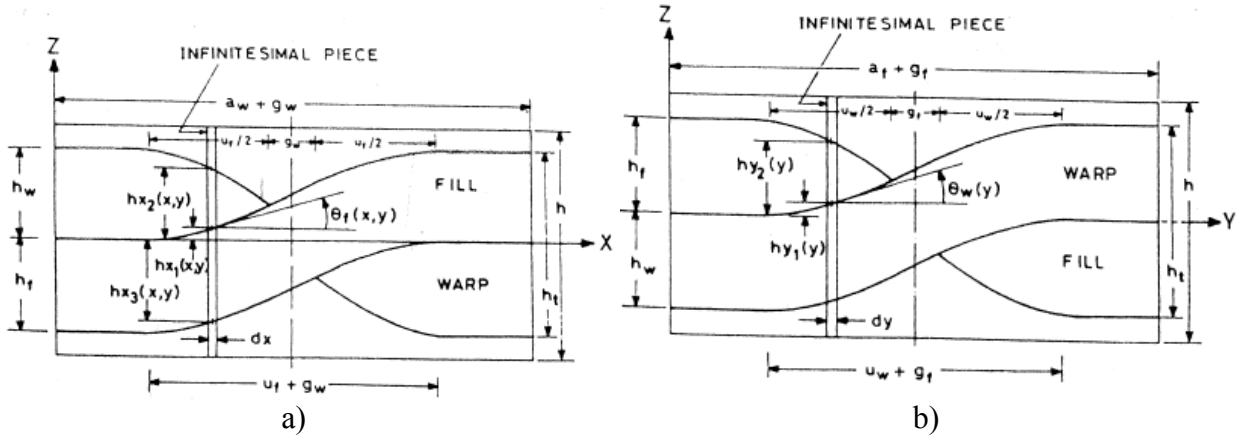


Figure 3-3: Section description: a) section E-A, b) section A-H

The expressions for a_1 to a_5 and b_1 to b_5 are as follows:

$$a_0 = 0; b_0 = 0 \quad (3.1)$$

$$a_1 = \frac{a_u - u_b}{2}; b_1 = \frac{a_b - u_u}{2} \quad (3.2)$$

$$a_2 = \frac{a_u}{2}; b_2 = \frac{a_b}{2} \quad (3.3)$$

$$a_3 = \frac{a_u - g_u}{2}; b_3 = \frac{a_b - g_b}{2} \quad (3.4)$$

$$a_4 = \frac{a_u}{2} + g_u; b_4 = \frac{a_b}{2} + g_b \quad (3.5)$$

$$a_5 = \frac{a_u + u_b}{2} + g_u; b_5 = \frac{a_b + u_u}{2} + g_b \quad (3.6)$$

$$a_6 = a_u + g_u; b_6 = a_b + g_b \quad (3.7)$$

The shape functions given below are given as an example of the geometrical description of the crossover used by Bejan and Poterasu (28) to define the configuration of the yarn in warp or fill direction are presented below:

$$h_{y1}(y) = \begin{cases} \frac{h_t}{2} - h_b, & 0 \leq y \leq b_1 \\ \left(1 + \sin\left((y - b_3) \frac{\pi}{u_u + g_b}\right)\right) \frac{h_t}{2} + \frac{h_t}{2} - h_b, & b_1 \leq y \leq b_5 \\ \frac{h_t}{2}, & b_5 \leq y \leq b_6 \end{cases} \quad (3.8)$$

$$h_{y1}(y) = \begin{cases} \frac{h_t}{2}, & 0 \leq y \leq b_1 \\ \left(\frac{h_t}{2} - h_{y1}(b_1)\right) \cos\left((y - b_1) \frac{\pi}{u_u}\right) + h_{y1}(b_2), & b_1 \leq y \leq b_2 \\ -\left(\frac{h_t}{2} - h_{y1}(b_2)\right) \cos\left((y - b_5) \frac{\pi}{u_u}\right) - h_{y1}(b_2), & b_4 \leq y \leq b_5 \\ -\frac{h_t}{2}, & b_5 \leq y \leq b_6 \end{cases} \quad (3.9)$$

As it is shown in this example, the geometrical description of a plain weave fabric unit cell is a complex task as it was carried out by Bejan and Poterasu (28).

Using previous works on geometry description, Warren (29) coupled it with the elastic beam theory to predict the response of yarns in uniaxial or biaxial tension taking into account a bending effect. Sagar et al. (13) employed a modified form of this geometry and used the principle of stationary potential energy to determine the fabric deformation resulting from an applied load. Warren and Sagar models (29), (13) are still limited in their prediction capabilities; since the models assume that the yarns remain orthogonal to one another, no in-plane rotation is allowed and thus it is not possible to account for shearing effects. Also, because of the complex geometries it is quite difficult to extend the model predictions to other types of loading without making overly simplifying assumptions.

3.2.2 Pin-jointed truss geometry

To overcome the problems and the demanding computations caused by the detailed geometry, other researchers have proposed simpler models to achieve greater mathematical simplicity and thus better computational efficiency. Kawabata et al. (21) was the first to propose the use of a

pin-jointed truss geometry to represent flexible fabric yarns that incorporates analytical models for the biaxial, uniaxial and shear deformation behaviors. His model is shown in Figure 3-4.

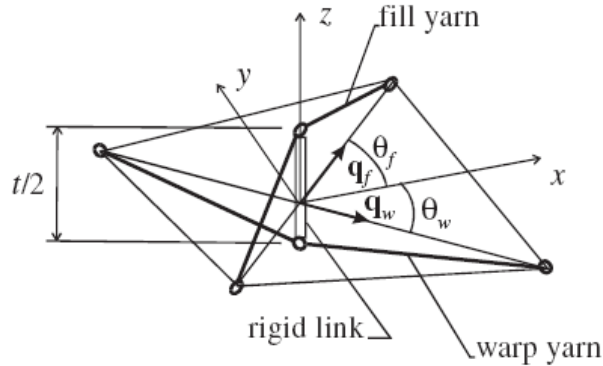


Figure 3-4: Pin-jointed truss geometry proposed by Kawabata et al. (11)

Since then, other works have been conducted to include other deformation behaviors. For example, Realff et al. (30) have modified Kawabata’s (21) model to include yarn flattening and consolidation due to yarn compaction. Other analyses of this type were performed by Roylance and Wang (16), Shim et al. (17), Lim et al. (18) and Shahkarami et al. (31). Pin-jointed orthogonal bars based FE analyses have proven to be very efficient in capturing the dynamic behavior of woven fabrics.

3.3 Continuum based modeling

The design of woven fabric systems is still largely based on empirical methods and experience. Modeling woven fabrics is challenging due to the need to capture the fabric response at both the macroscopic scale of the fabric and the “mesoscale” of the yarns that compose the weave. In fact, there is no widely accepted computational model for fabric deformation which is both computationally efficient and able to represent the behavior of the evolving structure of the fabric at the level of the individual yarns.

In the literature, either the fabric has been modeled at the level of the mesoscale, with detailed discretization of each fiber in the weave, or the fabric has been modeled at the continuum level, with phenomenological approaches, typically treating the fabric as an anisotropic continuum with two preferred material directions.

The continuum modeling approach, used by many researchers (32), (8) to capture the dynamic response of fabrics and fabric composites, is usually subdivided into 3D solid models and unit-cell shell models as illustrated in Figure 3-5 (a) and (b) respectively.

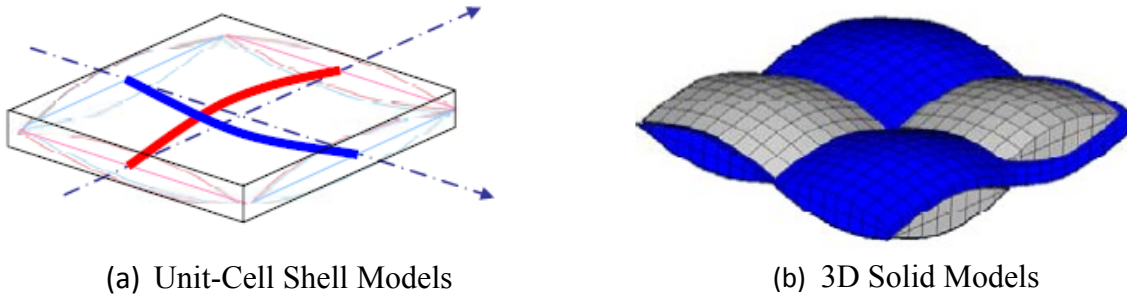


Figure 3-5: Continuum modeling approaches

3.3.1 3D solid models

This approach is focused on the numerical modeling to directly capture the fabric meso-structure. In consequence, every yarn in the fabric is modeled using solid continuum element with homogenized material properties. Using this approach, modeling a full ply is a tedious task because each yarn is represented as a solid model as it is shown in Figure 3-6.

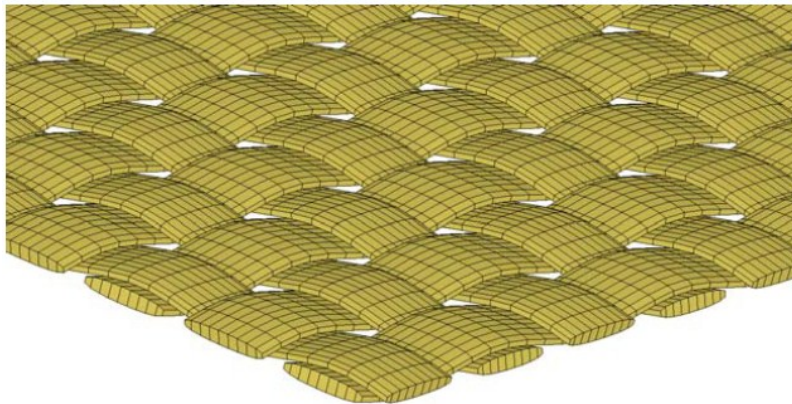


Figure 3-6: Full blown 3D modeling example

The difficult task here is both to set up the geometry in the finite element software and also to approximate the material properties for the yarns. This method has been used by Ng et al. (33), Boisse et al. (24) and Shockey et al. (19) among others and it has the advantage of capturing all yarn interactions and of providing a detailed description of yarn interactions at a mesoscale

level. However this method is very computationally demanding especially in analysis involving a multi-ply composite and therefore is usually limited to the prediction of the behavior of smaller systems. For example, it is used to gain insight into the mechanics of fabric deformation at a mesostructural level to estimate the homogenized material properties over a representative volume element. Furthermore, the constitutive behavior of each individual yarn will inevitably be a source of uncertainty as the yarns themselves are not homogeneous but composed of individual fibers. Detailing this complex morphology might require even more complex sub-modeling.

For 3D solid models, the discretization length scale is determined by the dimensions of the yarns and the weave pattern and thus multi-ply simulations are computationally prohibitive (31). Unit-cell shell models cannot be used to design fabrics based on the properties of the fibers and weave, and it is unsuitable for applications where the macroscopic response depends on the fabric's unique underlying mesostructure and its specific deformation mechanisms, such as fiber failure, crimp interchange, shear locking, or relative slip between the two yarn families. As such, without suitable models, the analysis and improvement of existing products and the development of new applications for woven fabrics is currently overly costly and time consuming.

3.3.2 Shell based unit-cell models

The principle of unit-cell shell based models is to homogenize the behavior of the underlying yarn structure to approximate the fabric in an anisotropic continuum having two preferred material directions. Homogenized formulations for textile reinforcement have been proposed by a number of researchers; Reese (34) considered an elastoplastic anisotropic continuum formulation, Xue et al. (35) and Shockey et al. (19) have proposed continuum models for woven composites. Work has also been done on knitted composites.

A continuum-level modeling technique for woven fabrics such as the ones developed by Shahkarami et al. (4) and King et al. (23) captures the macroscopic mechanical response of the fabric as well as the evolution of its mesostructure with deformation. An appropriate unit cell approximation, based on a pin-joined truss geometry, represents the weave architecture. The

configuration of the unit cell is determined by the macroscopic **deformation gradient** and the satisfaction of local equilibrium. The forces on the unit cell, and in turn the corresponding continuum level stresses, are calculated from physically motivated constitutive relations.

Unit-cell shell based continuum models typically allow greater computational efficiency and can easily be applied in multi-ply system models with good precision. The real challenge lies in the identification and characterization of the homogenized parameters to calibrate such models. There exist different manners to tackle the problem, for example, Xue et al. (35) relied on testing to determine material properties and Shockey et al. (19) used detailed 3D modeling of one crossover at mesoscale level.

The major handicap of this type of continuum modeling lies in the fact that most of the actual work in this field do not take into account the effects of the interactions between yarns. These interactions include crimp interchange, locking and resistance to relative yarn rotation. Crimp interchange is a mechanism by which the fabric elongates in one direction without notable yarn extension in that direction because of the yarn de-crimp mechanism that occurs while the crossing yarn in the perpendicular direction is retracting by becoming more undulated. Locking is a mechanism by which the fabric resists shear deformation as the yarns jam against each other. Relative yarn rotation is the dominant response of the fabric to in-plane shear which is a phenomenon that appears in many fabric applications including impact. Omission of these very important behaviors makes continuum models unsuitable for the general analysis of fabric systems where yarn interactions are important.

Because this work has been specifically focused on this approach, we will present it in greater details than the others. In section 3.4 we give a comprehensive review of the relevant literature and the shell based fabric unit-cell models is first presented, to highlight the strengths and shortcomings of the unit-cell models currently studied by other scientists.

3.4 Literature review on shell based unit-cell models

This approach combines the advantages of continuum modeling and analytical modeling. Mathematical relationships to evaluate the behavior of the fabric under specific loadings are incorporated in the anisotropic continuum medium to obtain a model that allows tracking of the

mesostructure's evolution as the continuum element deforms. It is interesting to note that in unit cell based modeling the yarns directions also evolve as the element deforms and so shearing effects can be precisely quantified.

In other words, one crossover is considered as being the representative volume element to which a simple geometrical model is associated to describe the evolution of the structure's deformation. This geometrical model, described by mathematical equations to capture the deformation effects is then implemented into a VUMAT that is embedded in a shell element that is none other than the anisotropic thin continuum medium. In that situation, during the numerical simulation, the displacements of the shell nodes translate into changes in the geometrical model allowing to calculate the forces in the yarns for the simple tension effect as well as other effects (yarn shearing, bending etc...). The process is described in Figure 3-7:

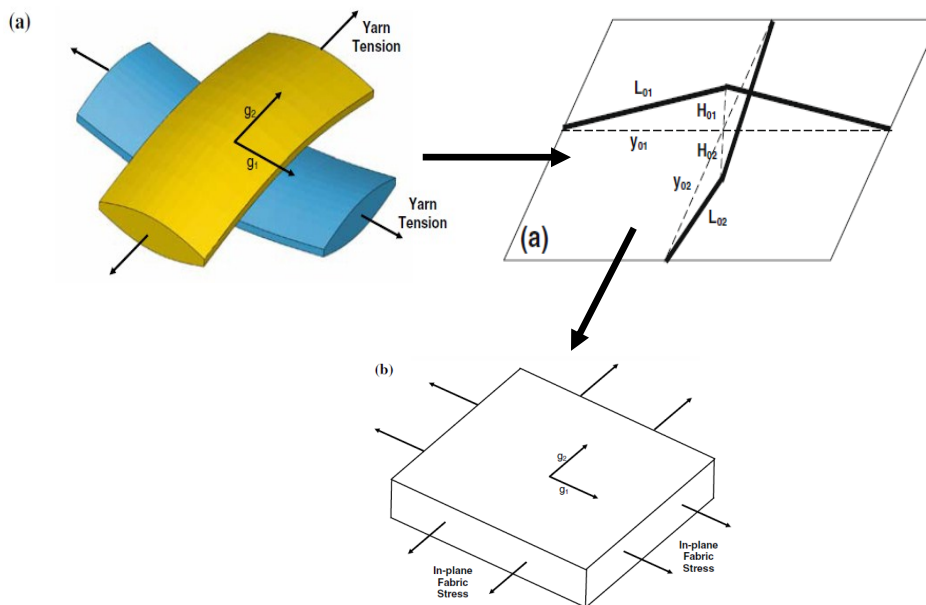


Figure 3-7: Unit-cell based modeling process from Grujicic et al (1)

Most fabrics possess a periodic geometry due to the specific pattern that the yarns are woven into, making them an excellent candidate for unit-cell analysis approach. Many researchers have tried to duplicate the mechanical response of fabrics into efficient membrane/shell elements. The elements developed are generally a continuum representation of the fabric through smearing the effects of warp and weft yarns into a two dimensional homogeneous material. While pin-jointed bar models of fabrics generally consider the response of warp and weft yarns

to be decoupled, shell/membrane elements can accommodate the biaxial behavior of the fabrics through implementation of appropriate constitutive models. This section includes a brief review of some of the unit-cell models that have employed shell/membrane elements as the basis to predict the fabric response.

Fabrics exhibit a non-linear structural response when stretched in the in-plane direction. Perhaps some of the earliest models of fabric crossover to capture the biaxial behavior of the fabrics response under extensional and shear deformation modes are those of Kawabata et al. (21). In a series of papers published in 1973, Kawabata et al. (21) presented simple analytical models to capture the biaxial and uniaxial behavior of symmetrically loaded yarn crossovers, as well as their shear response.

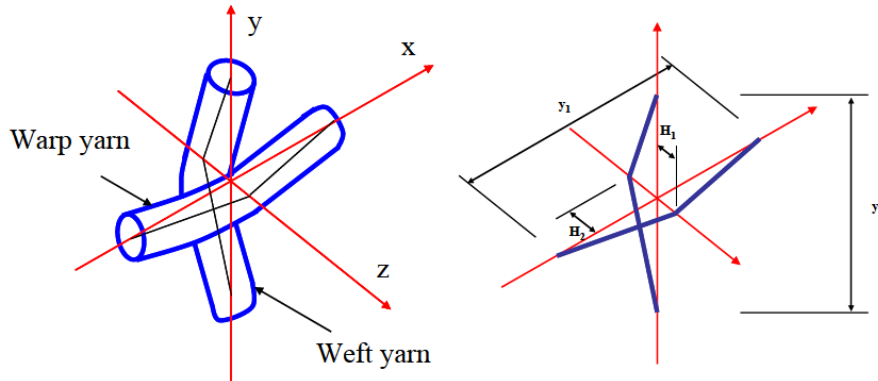


Figure 3-8: Illustration of the biaxial crossover model of a single plain weave fabric crossover with linear yarns originally developed by Kawabata et al. (21)

Considering a linear representation of the yarn centerlines shown in Figure 3-8, the equilibrium of the crossing yarns under biaxial extension was satisfied through balancing the yarns tensile forces with the contact force developed between them. Kawabata et al. (21) accommodated the transverse deformation of the yarns due to the inter-yarn contact force in determining the transverse position of the yarns satisfying the equilibrium of forces and compatibility of the deformations. This model was expanded in a subsequent paper (36) to incorporate the bending resistance of yarns, most dominant in the uniaxial extension of the fabrics. The model developed to capture the shear response of the fabric (37) is discussed in Section 4.3.2.

Since the early work of Kawabata et al. (21), many other studies have adopted a similar, if not identical, approach to capture the biaxial response of fabrics using finite element analysis

approach. Ivanov and Tabiei (22) developed a model that in their words was “a computational micro-mechanical material model for loosely woven fabric”, with a unit-cell consisting of a crossover with the yarns interacting under the applied displacements. The yarn material was considered to be visco-elastic and its response was modeled by a three-element spring/dashpot model and it was implemented in the shell element and used to simulate ballistic impact experiments on Kevlar fabric targets.

King et al. (23) published the details of a continuum-based model of a fabric unit-cell used to capture the deformational response of woven fabrics. The model relies on the selection of a representative model of weave geometry along with a constitutive relationship to capture the biaxial response of the fabric crossover. In this multi-scale approach, King et al. (23) adopted geometry similar to that of Kawabata et al. (21) to identify the in-plane extensional response of the yarns. The yarns were represented by an assembly of trusses pin-jointed together to make up the geometry of a certain weave. Other aspects of the fabric response such as lateral compression and bending of yarns were considered through individual springs in the unit-cell. With the knowledge of the macroscopic deformations and displacements of the fabric at any time, the internal forces can be calculated from the unique configuration of the yarns network by minimizing the energy stored in the system. King et al. (23) compared and obtained good agreement between the predictions of their numerical model and the laboratory data for a variety of different experiments. King’s model was further improved by Grujic et al. (1) works. Detailed mesoscopic model for biaxial analysis of fabric deformation during the forming process was developed by Boisse et al. (24). The initial geometry of yarns was represented by a combination of circular arcs and straight lines. The tensile response of the yarn was measured from simple tension tests. The model considered for transverse crushing law of the yarns was dependent on both the compressive state of the yarn and its axial tension. The friction between the yarns were considered implicitly to prevent relative sliding of the yarns, however, it was assumed that the frictional dissipative energy was too small compared to other energy components. Boisse et al. (24) used this model to predict the forming behaviour of a fabric with a square punch and die. They reported that their biaxial unit-cell model was in good agreement with the experimental data and the predictions of a 3D micromechanical unit-cell model they developed for the same purpose (discussed in Chapter 4).

Xue et al. (35) proposed a combined micro/macro-mechanical non orthogonal constitutive model to capture the large deformation behavior of the fabrics in the thermoforming process. The developed constitutive model considered details of the weave such as the dimensions of the yarns and the unit-cell, their material properties and the orientation of the yarns. The shear properties of the fabric were then obtained from a mechanistic analysis of the unit-cell and the tensile properties of the fabric were obtained from a simplified analytical model. The tensile model is based on incorporating the interaction of the crossing yarns through correlation parameters determined by performing fabric uniaxial tensile tests.

The continuum based fabric unit-cell models discussed above are just a few of many useful approaches to simulate the biaxial response of fabrics. The invaluable research and scientific development in the field of computational modeling of fabrics, some of which briefly discussed above, has been instrumental in the evolution of the approach presented in this thesis.

3.5 Shell fabric unit-cell formulation description

The 2D shell crossover model developed here is based on a continuum representation of the fabric unit-cells using shell elements following Shahkarami's work (4). The model captures the micromechanics of the yarns in the fabric through a smeared continuum approach. In establishing the basis of the model, it is assumed that the in-plane extensional mode of deformation is decoupled from the shearing mode. As a result, the constitutive relations developed for these two modes of deformation are derived separately. The following sections review the material models developed to capture the extensional and shearing response of a plain weave fabric unit-cell comprised of a single yarn crossover.

3.5.1 Simplifying assumptions

Several simplifying assumptions were made in the mathematical formulation. Firstly, the yarn profile of the woven fabric is assumed to be initially sinusoidal and remains sinusoidal at all times throughout the analysis. This assumption is based on the micrographic image of the yarns presented in Figure 3-9.



Figure 3-9: Cross-sectional micro-image of a plain weave fabric made of Kevlar fibers (2)

Secondly, the in-plane warp and fill displacements are assumed to be symmetrically applied at both yarn ends, this will prevent any sliding between the two crossing yarns and impedes the in-plane movement of the contact point. The in-plane displacement of the contact point is thus not allowed.

Thirdly, there is no friction between the contacting yarns so that contact force at any point of the yarn is perpendicular to the surface of the yarns. As the yarns interact a contact force develops between them while stretching occurs under applied displacement. The mechanics of the crossover point that we use only take into account the resulting force acting at the center-point of the crossover.

Fourth, it is assumed, based on the physical behavior of the fabric, that the out-of-plane stiffness of the fabric is insignificant compared to their in-plane stiffness. This is due to the fact that the bending stiffness is very low as is the shear stiffness.

Fifth, the extensional and shear responses of the fabric are totally decoupled and therefore in the user-defined material subroutine described in this work they are treated separately. This is explained in the sections to come.

3.5.2 In-plane extensional response

Plain weave fabrics exhibit strong biaxial behavior when extended in their plane. An analytical model is developed here to capture this biaxial response considering the interaction of warp and weft yarns at fabric crossovers. The model presented here is inspired by Kawabata's linear crossover model (21) with further expansion to accommodate the non-linear geometry of the yarns.

The model is based on tracking the location of the yarn centerlines (with geometries illustrated in Figure 3-10), as the two yarns interact under the applied displacements. The initial geometry of each yarn centerline is determined by its initial crimp value, obtained from the laboratory measurements.

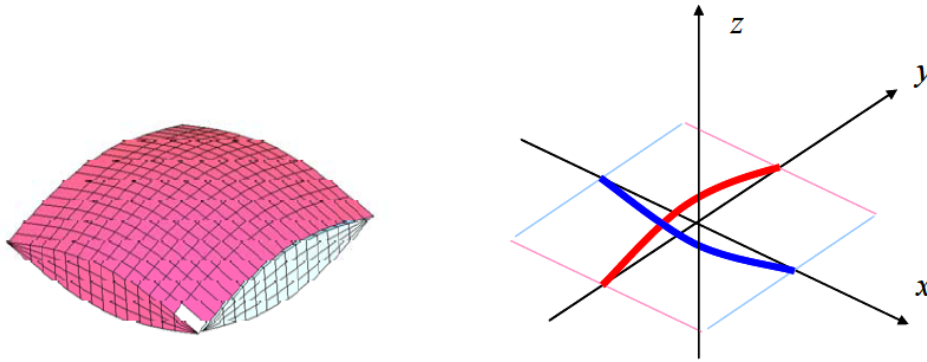


Figure 3-10: 3D finite element mesh of a single fabric crossover (left) and the equivalent mathematical representation of the yarns by their centerlines (right).

The analytical model developed here is aimed to capture the interaction of the warp and weft yarns and to determine their in-plane extensional response.

3.5.3 Shear Response

A distinctive attributes of plain weave fabrics is their unconventional shear behavior. Due to the specific arrangement of the yarns in the weave structure, the fabric can shear easily up to a certain locking angle where the compacted yarns resist further shearing. Many scientists in the textile industry and in the field of textile composites manufacturing have studied this behavior, some of which are reviewed here.

Kawabata et al. (21) introduced a semi-empirical model to capture the shear deformation response of fabrics. Usually the information obtained from the picture frame tests is used to set up a shear model for the plain weave fabric. The overall shear behavior of fabrics under biaxial tensile and shear deformations was approximated based on utilizing a linear empirical relationship to estimate the torque required to change the angle between the crossing yarns. The unknown parameters in this empirical relationship, comprised of a frictional and an elastic component, were calibrated through experimental measurements.

Prodromou and Chen (38) studied the relationship between the shear angle and wrinkling of textile composite performs. They performed frame shear tests on glass fabrics with plain weave, four and eight harness satin weaves. Their experimental results showed that two distinct regions can be distinguished on the load versus shear angle response of the fabrics: prior to locking where the trellis mechanism dominates the response and post-locking where the fabric starts to wrinkle out-of-plane due to high shear modulus in the fabric. They found that more conformable weaves such as satin would reach the shear locking at larger deformations, as is also the case for smaller yarn size at a given yarn count. The shear tests performed by Prodromou and Chen (38) indicated that the relative motion of the yarns at the centre of a fabric crossover does not occur during the trellising, meaning that the crossing yarns can effectively be considered pinned. Based on these observations, Prodromou and Chen (38) proposed a method for calculating the locking angle. In their proposed pin-jointed model, they assumed that shear locking occurs when the space between the parallel yarns closes, and moved on to calculate the locking angle by setting the distance between the yarns of the deformed fabric equal to their width. Based on the results obtained from this mechanistic pin-jointed model, they concluded that other factors not considered such as friction and changes in the yarn width and their spacing can result in a different measured locking angle compared to the predicted value.

McBride and Chen (39) proposed a pin-jointed shear model that would consider the geometry of the fabric unit-cell with sinusoidal yarn shapes during the shearing deformation. In this model, transverse yarn compaction was included as a deformation mechanism in addition to the trellising. The model predictions of yarns width and fiber volume fraction as a function of shear angle showed good agreement with the observed values, despite the inaccuracies stemming from other factors not accounted for, such as friction and fiber waviness within a yarn.

The model presented in this study is motivated by the two models of Prodromou and Chen (38) and McBride and Chen (39). A trellis mechanism is considered where the shear response of a crossover is subdivided into three distinct regions. Initially, due to the presence of gaps between parallel yarns, the lone resisting mechanism against shearing is considered to be friction, leading to a very small initial shear modulus (referred to here as zone I). Further shearing of the unit-cell would give rise to the shear modulus, as the yarns start to interact and compact each

other transversely (zone II). Eventually, the compaction of the yarns reaches a maximum value, after which the shear modulus is at its maximum and further shearing deformation of the fabric would lead to wrinkling (zone III). The information obtained from the picture frame tests are used to set up a shear model for the plain weave fabric.

3.6 Governing equations of the model

Some of the basic equations and assumptions used to track the principal deformations effects that occur inside the geometrical structure (such as yarn tension, yarn bending, yarn crossover contact and yarn locking) will be described in this section.

3.6.1 Tension (4)

When both yarns are intact and under tension the in-plane normal strains in both directions are positive and there is a non-zero contact force between the yarns at the crossover. The effect of the contact and the yarn equilibrium must be taken into account before computing the yarn tensions. A simple procedure is used for the calculation of yarn tensions using the yarn contact force at the crossover enabling us to obtain the yarn centerline heights (denoted H_i). The truss element lengths L_i can therefore be calculated using the representative volume element half-length (denoted y_i) as such (see figure 3.8):

$$L_i = \sqrt{y_i^2 + H_i^2} \quad (3.10)$$

It follows that the tensions T_i within the truss members is described by the following equation:

$$T_i = K_i(L_i - L_{0,i}) \quad (i = 1,2) \quad (3.11)$$

where subscript 0 is used to denote the initial (undeformed) quantity, and K_i is the yarn-stiffness constant taken, in our case, from the 3D model of the crossover which is detailed in Chapter 5. It is assumed that truss members have no ability to support compressive axial loads. The full procedure for calculating yarn tension is covered in great detail in Chapter 6.

3.6.2 Shearing (4)

Following Shahkarami's thesis work, the fabric geometry changes from its initial state to deformed state are schematically shown in Figure 3-11. As the fabric shears, the warp-to-weft

angle β decreases from its original value, denoted β_0 , thus reducing the spacing between the adjacent parallel yarns. This distance, denoted u , is shown in Figure 3-11. The relationship between the shear angle and yarn spacing can be derived from the fabric deformed geometry, as:

$$\sin \beta = \frac{u}{L} \quad (3.12)$$

where L is the side-length of the fabric in picture frame shear test. The presence of in-plane gap, p , between adjacent yarns in the undeformed configuration allows the fabric to shear freely to a certain angle, β_1 . At this angle, the inter-yarn gap diminishes and the parallel yarns start to get in contact with each other. Angle β_1 can be calculated as:

$$\sin \beta_1 = \frac{u_0 - p}{L} \quad (3.13)$$

where u_0 is the initial distance between the yarns. Further shearing of the fabric leads to gradual compaction of the yarns, up to an angle β_2 , where the yarns reach their maximum compaction. This angle can be calculated from the following equation:

$$\sin \beta_2 = \frac{u_2}{L} \quad (3.14)$$

where u_2 corresponds to the yarns spacing at maximum compaction. In order to calculate u_2 , certain assumptions need to be made. It is assumed that the fabric thickness, as reported in many other studies, remains more or less constant and is decoupled from the shear deformation. Based on this assumption, it is concluded that the amplitude of the sine function representing the yarn profiles remains constant during shear. It is further assumed that the yarn cross-sectional shape becomes elliptical at the point of full compaction. In reality, the yarn compaction would not be uniform along its length due to the localized interaction of the crossing yarns and their specific configuration in a highly sheared fabric. To account for this effect, an area reduction factor, denoted K_s , is considered which results in a yarn packed area that can be estimated from the formula below that can be derived using the schematic of the yarns in the sheared unit cell shown in Figure 3-11:

$$A_p = K_s A_s = \pi u_2 \frac{t}{2} \quad (3.15)$$

The values of u_2 calculated from the above equation can be substituted in equation (3.14) to determine the locking angle β_2 . Using the locking angles β_1 and β_2 , the corresponding shear strains γ_1 and γ_2 can be determined.

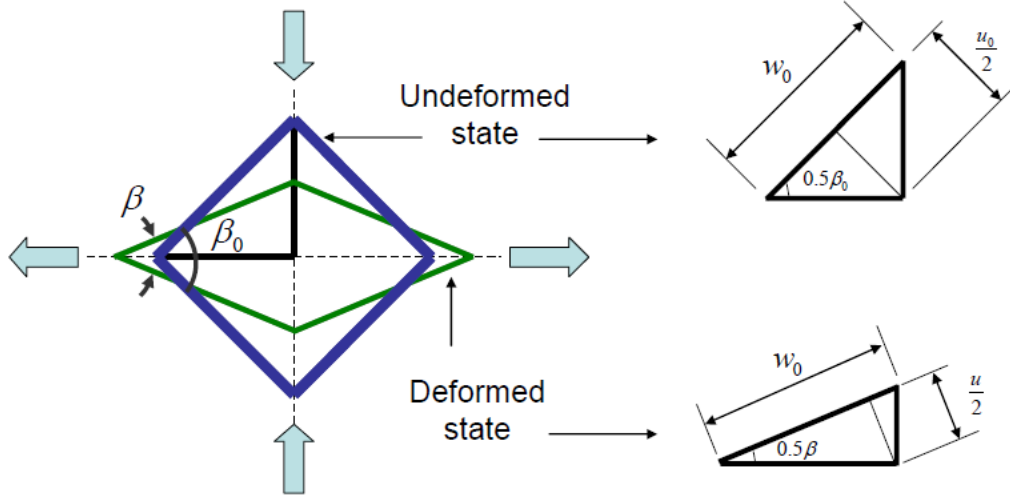


Figure 3-11: Shear model representation

The shear stress-strain relationship is formulated such that the instantaneous shear strain γ is related to the secant shear modulus G by the function defined by:

$$G = \begin{cases} G_1 & \text{si } 0 < \beta \leq \beta_1 \\ G_1 + \frac{G_2 - G_1}{\beta_2 - \beta_1} (\beta - \beta_1) & \text{si } \beta_1 < \beta \leq \beta_2 \\ G_2 & \text{si } \beta \geq \beta_2 \end{cases} \quad (3.16)$$

3.6.3 Yarns crossover contact (4)

Yarn/yarn interactions and yarn cross-sectional area changes at the crossover points are accounted for through the use of a non-linear, axial “interference” spring whose contact force, F_c , versus yarn contact overclosure d_c , relation is defined by the following constitutive relation:

$$F_c = \frac{b d_c}{a - d_c} \quad (3.17)$$

where a and b are constants that need to be calibrated through 3D modeling of a fabric crossover and the interference, d_c , is defined as a difference between the sum of the initial crimp amplitudes and the sum of the current crimp amplitudes.

3.6.4 Yarn bending (1)

The yarn-bending moment, M_{bi} , is assumed to depend linearly on the change in yarn crimp angle, $\beta_i - \beta_{0,i}$, so that the constitutive relation for the rotational springs attached at the truss-member pin joints is defined as:

$$M_{bi} = K_{bi}(\beta_i - \beta_{0,i}) \quad (i = 1,2) \quad (3.18)$$

where K_{bi} is the bending stiffness. To account for different amounts of permanent set in the yarns, appropriate values should be assigned to the reference crimp angle $\beta_{0,i}$.

3.6.5 Yarn locking (1)

Before a constitutive relation for the locking trusses is proposed, it must be recognized that the yarn cross section is typically an oblate ellipse.

- Yarn cross-sectional area changes associated with the crossover-point interference, discussed above, are taking place primarily in the direction of the minor axis of the yarn cross-section (i.e., in the fabric through-the thickness direction).
- In the case of yarn locking, these changes take place in a direction parallel to the yarn cross-section major axis. Consequently, the locking response is expected to be more compliant than the yarn crossover-interference response. To account for this difference, a power-law relation is used to describe the locking force, $F_{L,i}$, versus locking interference, $I_{L,i} = d_{0,i} - d_i$, where $d_{0,i}$ is the locking-truss length where the locking first time takes place.

$$F_{L,i} = \begin{cases} 0 & \text{if } I_{L,i} \leq 0 \\ K_d (I_{L,i})^c & \text{if } I_{L,i} > 0 \end{cases} \quad (3.19)$$

where K_d and c are the ‘‘locking’’ material parameters.

Among the most notable studies were those carried out by Kawabata et al. (21) Furthermore, Ivanov and Tabiei (22) proposed a micromechanical model for a woven fabric to use in impact

simulations. Interestingly, they introduced a procedure to determine the position of equilibrium of the crossover and to study its evolution under applied strain. Therefore the crimp interchange mechanism is accounted for because knowing the position on that particular point enables one to calculate the crimp for each fiber.

Boisse et al. (24) successfully developed a four-node finite element for textile composite forming applications. Recently King et al. (23) proposed a new model to derive the continuum-level material model for fabrics based on an energy minimization technique. This technique establishes the relationship between the configuration of the fabric structure and the microscopic deformation of fabric components. Boisse et al. (24) and Peng and Cao (25) have also developed such models. Finally, Shahkarami and Vaziri (2) have created a similar model to the one proposed by King et al. (23) only simplified but fully integrated in commercial dynamic-explicit finite element softwares by using the VUMAT user subroutine. It is upon Shahkarami's equations that we based our Abaqus VUMAT subroutine that has been used in all our numerical tests.

3.7 Conclusion

In this chapter, a brief literature review was performed in order to get acquainted with different types of methodologies used to model the dynamic behavior of ballistic fabrics subjected to simple loadings aimed at capturing specific deformation mechanism (shear, bending etc...). Despite many attempts to develop effective models for fabric behavior, there is no widely accepted model that can predict the response of fabric in every type of application. Indeed, the models do not capture all the important aspects of fabric deformation largely because the requirements for fabric models differ with each specific application.

In this work, a continuum level modeling technique for woven fabrics such as the one used by Shahkarami et al (2) and King et al (23) which captures the macroscopic response of the fabric as well as the evolution of its mesostructure with deformation in a single efficient modeling step is used. Both the 3D solid models and the unit-cell shell models are employed to develop a fabric crossover material model that is implemented in the commercial nonlinear finite element fully explicit solver code Abaqus through its VUMAT subroutine facility. The implementation

is done so that the material model can be used with Abaqus S4R shell element with hard contact. In addition to displacement degrees of freedom, degrees of freedom representing the crimp amplitude of each yarn family are defined in order to solve for the configuration of the fabric unit cell at each step in time. The accuracy of the model is verified by comparing the simulation results with the experimental results provided by Shahkarami et al (2). The fabric model is used to simulate projectile impact on single plies of plain-weave Kevlar. Direct comparisons are made with experimental data obtained from available literature (ELVS data).

CHAPTER 4 - DESCRIPTION OF THE MAIN TOOLS

4.1 Explicit Dynamic FE formulation

An explicit dynamic analysis is computationally efficient for the analysis of large models with relatively short dynamic response times and for the analysis of extremely discontinuous events which is the case in our impact models. Explicit solutions are especially suited for problems where a small time step is required because of:

- **Material non linearity.** A high degree of non-linearity requires very small time step for accuracy.
- **Large geometric nonlinearity.** Contact and friction algorithms can introduce instabilities and a small time step is needed for accuracy and stability.
- **Material or geometric non-linearity combined with large displacements.**
- **Large models.** Explicit methods have also increasing advantage over implicit methods for large models containing several thousand elements.

In explicit codes, by using the principle of virtual work, internal and external forces are summed at each node and the discrete equations of motion become:

$$M\ddot{u} + f_{int} = f_{ext} \quad (4.1)$$

where M is the mass matrix and the displacement and its derivatives are denoted by u and $\ddot{\cdot}$. f_{int} and f_{ext} are respectively the internal and external force vectors. Explicit methods do not require matrix decomposition or matrix solutions since M is usually lumped and division by the nodal mass yields the nodal acceleration. Instead, a loop is carried out for each time step as shown in Figure 4-1. The algorithm is however conditionally stable and therefore the maximum permissible time step is the time for an acoustic wave to travel through the material.

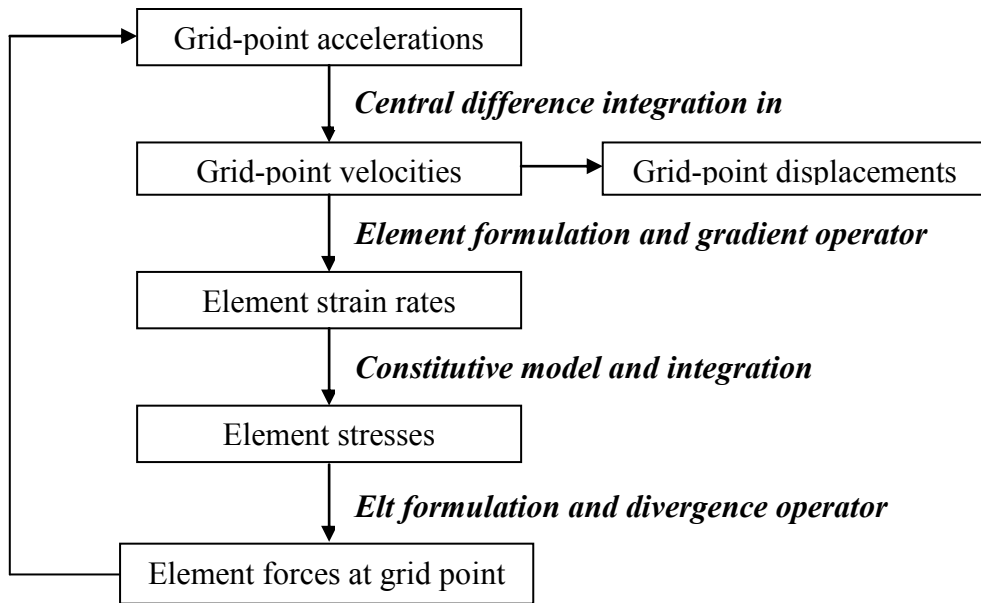


Figure 4-1: Explicit integration scheme loop

4.1.1 Central difference integration rule

In Abaqus/Explicit, the explicit integration scheme is based on the central difference integration rule of the equation of motion for the body considered. A key to the computational efficiency of the explicit procedure is the use of diagonal element mass matrices because the inversion of the mass matrix that is used in the computation for the accelerations at the beginning of the increment is trivial. Equation 4.1 thus becomes:

$$M\ddot{u} = f^{ext} - f^{int} \quad (4.2)$$

$$\ddot{u} = \frac{1}{M}(f^{ext} - f^{int}) \quad (4.3)$$

The explicit procedure requires no iterations and no tangent stiffness matrix and there is no need of solving a coupled system of equations.

The integration rule is based on the following explicit equations [Abaqus/Explicit user guide]:

$$\dot{u}^{(i+\frac{1}{2})} = \dot{u}^{(i-\frac{1}{2})} + \frac{\Delta t^{(i+1)} + \Delta t^{(i)}}{2} \ddot{u}^{(i)} \quad (4.4)$$

$$u^{(i+1)} = u^{(i)} + \Delta t^{(i+1)} \dot{u}^{(i+\frac{1}{2})} \quad (4.5)$$

where \dot{u} is the velocity and \ddot{u} is the acceleration. Equation 4.4 means that the kinematic state is advanced using known values of $\dot{u}^{(i-\frac{1}{2})}$ and $\ddot{u}^{(i)}$ from the previous increment. Unless the initial values (at time $t = 0$) of velocity and acceleration are specified by the user, they are set to zero. We assert the following condition:

$$\dot{u}^{(+\frac{1}{2})} = \dot{u}^{(-\frac{1}{2})} + \frac{\Delta t}{2} \ddot{u}^{(0)} \quad (4.6)$$

The central difference operator is not self-starting at $i = 0$ because the value of the mean velocity $\dot{u}^{(-\frac{1}{2})}$ needs to be defined. Substituting equation 4.4 in equation 4.5 yields the following definition of $\dot{u}^{(-\frac{1}{2})}$.

$$\dot{u}^{(-\frac{1}{2})} = \dot{u}^{(0)} - \frac{\Delta t^{(0)}}{2} \ddot{u}^{(0)} \quad (4.7)$$

4.1.2 Time step control

The control of the time increment can be either defined by the user or set to automatic mode. In the latter case, Abaqus/Explicit loops through the elements to update the stresses and determines a new time step Δt by taking the smallest of the set of time increments calculated for each one of the N elements of the model such as:

$$\Delta t^{i+1} = \alpha_f \cdot \min(\Delta t_{elt\ 1}, \Delta t_{elt\ 2}, \Delta t_{elt\ 3}, \dots, \Delta t_{elt\ N}) \quad (4.8)$$

For stability reasons, the scale factor α_f is multiplied on the smallest found time step. This factor is usually set to 0.9.

In Abaqus explicit code, the time step for each shell element is estimated based on the smallest characteristic length of the shell elements L_c in the analysis and on the speed of sound inside the considered material c_s such as:

$$\Delta t \cong \frac{L_c}{c_s} \quad (4.9)$$

From the knowledge of Young's modulus E , Poisson's ratio ν and the material density ρ , we can calculate the speed of sound in the material which is given by:

$$c_s = \sqrt{\frac{E}{\rho(1 - \nu^2)}} \quad (4.10)$$

Knowing the length of the four edges of each shell element denoted $L_{i=1,2,3,4}$ and the area A_s of the element, we can obtain the characteristic length of a shell element using the following formula:

$$L_c = \frac{A_s}{\max(L_1, L_2, L_3, L_4)} \quad (4.11)$$

4.2 Constitutive law of the model

As we have seen in the literature review provided in Chapter 3, the multi-scale nature of the reinforcements allows discrete as well as continuous approaches. In discrete approaches also called mesoscale approaches each yarn is modeled individually thus this approach is limited to small domain study. The continuous approach considers the fibrous material as a continuum. The yarns are not continuous when considered at a microscopic scale but it may be considered continuous in average at a macroscale level. The constitutive model of this continuum has to convey the very specific mechanical behavior of the fibrous reinforcement during the deformation and also has to take finite strain into account because fabric deformations usually involve large shear angles. Among continuous models of mechanical behavior at large strain,

rate constitutive equations relating stress and strain rates (also called hypoelastic laws) are widely used (4).

The hypoelastic approach uses a rotated frame in which the objective summation of stress increments is performed. Rotations classically used are the ones from the polar decomposition of the deformation gradient tensor (Green Naghdi objective derivative) (4) or the corotational frame rotation (Jaumann objective derivative). The constitutive operator calculations are performed in the corresponding rotated frame (Green Naghdi's frame or corotational frame). The components of this operator in this frame are obtained from its specific form in the yarn frame by a change of base.

These rotations are mean values of the material rotations and are well adapted for finite strain calculations of isotropic media, and particularly metals. In the case of fibrous media, the yarn orientation does not follow the orientation of the previously mentioned frames.

For example, let's observe the fibrous media presented in Figure 4-2 where f is the unit vector in the fiber direction.

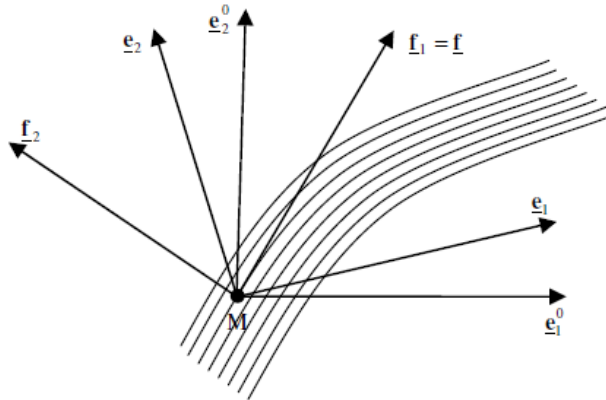


Figure 4-2: Initial frame e_{0i} , rotated frame e_i and yarn frame f_i in the case of unidirectional yarns

Frame e_i denotes the orthonormal frame formed by the initial basis vectors e_{0i} rotated by the rotation Q . e_i is the rotated frame. The direction of the vector f is in general not constant in e_i . Since it is a material direction, the initial yarn direction f_0 is transformed by F the gradient tensor into $f = f_1$, while e_i is rotated by Q (see Figure 4-2).

In case of fibrous materials, the constitutive tensor C is oriented by f which is varying in the rotated frame. The mechanical behavior of fibrous media is thus directly related to the orientation of the yarn which is a material direction. To take into account and solve that particular aspect two approaches have been developed for fibrous media within the hypoelastic formulation.

The first one, which is the most frequently used (4) is based on the objective derivative of Green Naghdi (or Jauman's one) and the corresponding rotated frame (as proposed by FE codes). Using this approach is convenient, its principal advantage lies in the direct use of the rotated frame of the commercial codes (Green Naghdi's or corotational). These codes provide the user with the whole set of quantities necessary for the incremental computation using this frame.

The second approach consists in using another objective derivative defined from the yarn rotation and has been used by Badel et al. (40) in his works. According to his paper (40) the rotated frame used in the hypoelastic law follows the yarn rotation better than the Green-Naghdi frame. Indeed objective derivative of Green-Naghdi uses a rotation that fits the matter only in average which is precise enough for isotropic materials or for anisotropic material that can be assumed to be oriented by this rotated frame. However in the case of fibrous materials under load cases leading to finite strain in the material it may lead to a rotation discrepancy between the material directions and the computed Green-Naghdi directions. The results obtained give satisfying results to some tests on fibrous materials undergoing finite strains. The analysis of a woven unit cell submitted to large in-plane performed using the approach based on the yarn rotation shows that numerical results are in good agreement with a shear picture frame experimental test. According to Badel et al. (40), this fiber frame approach preserves the objectivity and thus yields greater accuracy as well as better computational stability. The paper even goes further stipulating that "only this approach is correct to simulate fibrous media undergoing finite strains". We will detail this very interesting method in the following sections.

Because of its integrated nature with Abaqus, the hypoelastic approach with Green-Naghdi objective derivative has been used in this work. At this point it is important to mention that two methods described above will be explored for the case of in-plane yarn displacements because

this is what the VUMAT presented in this work was coded for. Also this will simplify the equations, putting more emphasis on the algorithm.

4.3 Description of the Green-Naghdi hypoelastic approach

The rate constitutive equations (or hypoelastic laws) are widely used in FE codes (41):

$$\sigma^{\nabla} = \mathbf{C} : \mathbf{D} \quad (4.12)$$

where σ^{∇} is an objective derivative of the Cauchy stress tensor σ and \mathbf{D} is the strain rate deformation tensors. These two dual tensors are usually considered as eulerian variables for the strain rate and the stress in the continuum mechanics. The aim of the objective derivative is to avoid spurious results induced by rigid body rotations in $\dot{\sigma} = \frac{d\sigma}{dt}$, the time derivative of σ , if these are not properly handled. It can be seen as a derivative for an observer who is fixed with respect to the matter. Several objective rates addressing this issue have been developed and are available in technical literature. However the rotational objective derivatives are the most commonly used for simplicity reasons.

If a rotation operator \mathbf{Q} is used to define a frame that will be called “rotated frame”, the objective derivative is then the derivative for an observer fixed in this rotated frame and can be written as :

$$\sigma^{\nabla} = \mathbf{Q} \cdot \left(\frac{d}{dt} (\mathbf{Q}^T \cdot \sigma \cdot \mathbf{Q}) \right) \cdot \mathbf{Q}^T \quad (4.13)$$

If we introduce the corresponding spin such as:

$$\mathbf{\Omega} = \dot{\mathbf{Q}} \cdot \mathbf{Q}^T \quad (4.14)$$

we can write the objective Cauchy stress derivative as:

$$\sigma^{\nabla} = \dot{\sigma} + \sigma \cdot \mathbf{\Omega} - \mathbf{\Omega} \cdot \sigma \quad (4.15)$$

The rotation operator \mathbf{Q} can be written in two ways depending on the chosen objective derivative. For example in the case of the Green-Naghdi objective derivative, the rotation operator \mathbf{Q} is taken as the rotation tensor \mathbf{R} obtained from the polar decomposition of the gradient tensor \mathbf{F} written as follows:

$$\mathbf{F} = \mathbf{R} \cdot \mathbf{U} \quad (4.16)$$

4.3.1 Updating current constitutive axes

For woven composite materials, the constitutive tensor \mathbf{C} is oriented always along the fiber directions; hence it is essential to update the current fiber direction so that the constitutive laws could be used properly. The necessary steps to carry out that update are described below. But since the implementation details are given in chapter 6, here only a brief overview is given in this section. Considering e.g. a plane stress problem as shown in Figure 4-3, the Green-Naghdi axes are rotated by \mathbf{R} which is the rotation tensor obtained from polar decomposition of gradient as such:

$$\mathbf{R} = \mathbf{F} \cdot \mathbf{U}^{-1} \quad (4.17)$$

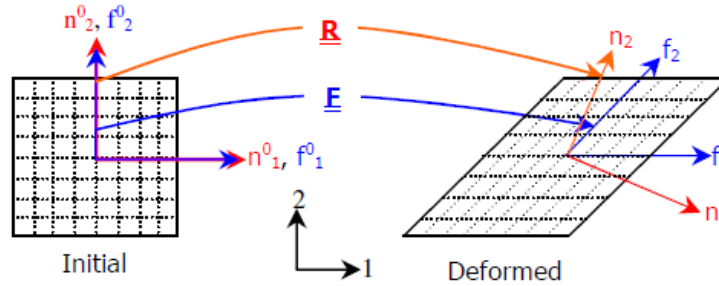


Figure 4-3: An element with simple shear under plane stress showing Green-Naghdi (\mathbf{n}) and Fiber Frames (\mathbf{f}) before and after deformation (41)

The Green-Naghdi axes denoted hereafter by \mathbf{e}_i are updated as:

$$\mathbf{e}_1 = \frac{\mathbf{R} \cdot \mathbf{e}_1^0}{\|\mathbf{R} \cdot \mathbf{e}_1^0\|} \quad \mathbf{e}_2 = \frac{\mathbf{R} \cdot \mathbf{e}_2^0}{\|\mathbf{R} \cdot \mathbf{e}_2^0\|} \quad (4.18)$$

Where \mathbf{e}_1^0 and \mathbf{e}_2^0 are the Green-Naghdi axes from the previous time increment equivalent respectively to \mathbf{n}_1 and \mathbf{n}_2 in Figure 4-3. Also the yarn directions need to be updated. They are obtained from the deformation gradient tensor \mathbf{F} as:

$$\mathbf{f}_1 = \frac{\mathbf{F} \cdot \mathbf{f}_1^0}{\|\mathbf{F} \cdot \mathbf{f}_1^0\|} \quad \mathbf{f}_2 = \frac{\mathbf{F} \cdot \mathbf{f}_2^0}{\|\mathbf{F} \cdot \mathbf{f}_2^0\|} \quad (4.19)$$

Note that f_i^0 and e_i^0 are assumed to coincide initially. Once both directions of yarn axes f_i and GN axes e_i are determined, it is then possible to transform strain increment from current software working axes (GN) to yarn frame. Since the two yarn directions do not remain orthogonal after deformation, it is necessary to generate a new local orthogonal frame where each one of the two yarn axes will be defined.

4.3.2 Transforming strains and stresses between GN frame and yarn frame

This transformation necessitates the knowledge of two angles at each increment. The first angle is θ_1 between the vectors e_1 and f_1 and the second one is θ_2 between the vectors e_2 and f_2 . The computation of these specific angles is detailed in chapter 6. Let us denote by $[\theta]$ the transformation matrix between the Green-Naghdi axes and yarn axes, it is written at each time increment as follow:

$$[\theta]_i = \begin{bmatrix} \cos\theta_i & \sin\theta_i \\ -\sin\theta_i & \cos\theta_i \end{bmatrix} \quad (4.20)$$

Abaqus gives the strains in the Green-Naghdi frame and so the strain in the yarn directions is defined as:

$$[\varepsilon]_{f_i} = [\theta]_i^T [\varepsilon]_{e_i} [\theta]_i \quad (4.21)$$

Stresses along yarn directions are computed using the constitutive tensor in the yarn direction and the transformed yarn direction strains from the previous equation:

$$[\sigma]_{f_i} = [C]_{f_i} [\varepsilon]_{f_i} \quad (4.22)$$

And finally the stresses are transformed to the Green-Naghdi Frame: the default bases of stress calculation in Abaqus/Explicit.

$$[\sigma]_{e_i} = [\theta]_i [\sigma]_{f_i} [\theta]_i^T \quad (4.23)$$

The above formulations are implemented in the user subroutines VUMAT of Abaqus/Explicit. Since two methods of calculations are proposed in this article, only one fiber direction is updated for two sets of elements with unidirectional fibers oriented differently whereas both directions are updated with two directions of material orientation in the same set of elements.

4.3.3 Computation algorithm for the hypoelastic GN approach

The implementation of the Green-Naghdi approach using Abaqus' VUMAT user subroutine is described in this section. The methods to be used in other finite element codes that let the user write the constitutive equations at finite strain should be very similar. At each time step n the code provides the following matrices:

$$[F^{n+1}]_{e_i^0}; [U^{n+1}]_{e_i^0}; [\sigma^n]_{e_i^n}; [\Delta\varepsilon]_{e_i^{n+1/2}}$$

The user subroutine has to return the stress state at the end of the step: $[\sigma^{n+1}]_{e_i^{n+1}}$. Since F and U are given at time $n + 1$, it is needed to work at the end of step configuration instead of mid step configuration. The implementation of both above approaches using the VUMAT user subroutine in Abaqus is explained later. The performed steps of the computations are given below.

Step-1: Compute the inverse matrix of the right stretch tensor: $[U^{n+1}]_{e_i^0}^{-1}$

Step-2: Compute the polar rotation matrix:

$$[R^{n+1}]_{e_i^0} = [F^{n+1}]_{e_i^0} [U^{n+1}]_{e_i^0}^{-1} \quad (4.24)$$

Step-3: Compute the current work basis e_i^{n+1} from e_i^0 and $[R^{n+1}]_{e_i^0}$ using the equation below:

$$e_i^{n+1} = [R^{n+1}]_{e_i^0} \cdot e_i^0 \quad (4.25)$$

Step-4: Compute the current material basis f_i^{n+1} from e_i^0 and $[F^{n+1}]_{e_i^0}$ using the equation below:

$$f_i^{n+1} = [F^{n+1}]_{e_i^0} \cdot e_i^0 \quad (4.26)$$

Step-5: Compute the rotation (we restricted our explanation to in-plane rotations) and base change matrix $[\theta]_{e_i^{n+1}}$ such as:

$$[\theta]_{e_i^{n+1}} = \begin{bmatrix} \cos\theta_i & \sin\theta_i \\ -\sin\theta_i & \cos\theta_i \end{bmatrix} \quad (4.27)$$

where θ_i is the angle between the vectors e_i and f_i ($i=1,2$).

Step-6: Obtain ΔR which represents the rotation between configuration at $t = n + 1$ and $t = n + \frac{1}{2}$

$$\Delta R = R^{n+1} \cdot \left(R^{n+\frac{1}{2}}\right)^T \quad (4.28)$$

Step-7: Compute the corresponding transformation $T_{\Delta R}$:

$$T_{\Delta R}(S) = \Delta R \cdot S \cdot \Delta R^T \quad (4.29)$$

Step-7: Derive $\left[T_{\Delta R}\left(C^{n+\frac{1}{2}}\right)\right]_{e_i^{n+1}}$ from $[C]_{f_i^{n+\frac{1}{2}}}$ which is the constitutive matrix expressed in the rotated frame as such:

$$\left[C^{n+\frac{1}{2}}\right]_{e_i^{n+\frac{1}{2}}} = \Delta R \cdot [C^{n+1}]_{e_i^{n+1}} \cdot \Delta R \quad (4.30)$$

Step-8: Update the stress tensor and return it to Abaqus:

$$[\sigma^{n+1}]_{e_i^{n+1}} = [\sigma^n]_{e_i^n} + \left[T_{\Delta R}\left(C^{n+\frac{1}{2}}\right)\right]_{e_i^{n+1}} [T_{\Delta R}(\Delta \varepsilon)]_{e_i^{n+1}} \quad (4.31)$$

4.3.4 Computation algorithm for Badel's fiber frame (FF) approach

Badel's algorithm [] is described in detail in this section.

Step-1: Compute the inverse matrix of the right stretch tensor: $[U^{n+1}]_{e_i^0}^{-1}$

Step-2: Compute the polar rotation matrix:

$$[R^{n+1}]_{e_i^0} = [F^{n+1}]_{e_i^0} [U^{n+1}]_{e_i^0}^{-1} \quad (4.32)$$

Step-3: Compute the current work basis e_i^{n+1} from e_i^0 and $[R^{n+1}]_{e_i^0}$ using the equation below:

$$e_i^{n+1} = [R^{n+1}]_{e_i^0} \cdot e_i^0 \quad (4.33)$$

Step-4: Compute the current material basis f_i^{n+1} from e_i^0 and $[F^{n+1}]_{e_i^0}$ using the equation below:

$$f_i^{n+1} = [F^{n+1}]_{e_i^0} \cdot e_i^0 \quad (4.34)$$

Step-5: Compute the rotation (we restricted our explanation to in-plane rotations) and base change matrix $[\theta]_{e_i^{n+1}}$ as such:

$$[\theta]_{e_i^{n+1}} = \begin{bmatrix} \cos\theta_i & \sin\theta_i \\ -\sin\theta_i & \cos\theta_i \end{bmatrix} \quad (4.35)$$

where θ_i is the angle between the vectors e_i and f_i ($i=1,2$).

Step-6: Derive the material strain increment from the code's strain increment:

$$[T_{\Delta R}(\Delta\varepsilon)]_{f_i^{n+1}} = [\theta]_{e_i^{n+1}}^T [T_{\Delta R}(\Delta\varepsilon)]_{e_i^{n+1}} [\theta]_{e_i^{n+1}}^T \quad (4.36)$$

Step-7: Update the material stress tensor:

$$[\sigma^{n+1}]_{f_i^{n+1}} = [\sigma^n]_{f_i^n} + \left[T_{\Delta R} \left(C^{n+\frac{1}{2}} \right) \right]_{f_i^{n+1}} [T_{\Delta R}(\Delta\varepsilon)]_{f_i^{n+1}} \quad (4.37)$$

Step-8: Return the stress tensor in the work basis of the code:

$$[\sigma^{n+1}]_{e_i^{n+1}} = [\theta]_{e_i^{n+1}} [\sigma^{n+1}]_{f_i^{n+1}} [\theta]_{e_i^{n+1}}^T \quad (4.38)$$

4.4 Shell element description

Shell elements are used to model structures in which one dimension, the thickness, is significantly smaller than the other dimensions. Conventional shell elements use this condition to discretize a body by defining the geometry at a reference surface. In this case the thickness is defined through the section property definition. Conventional shell elements have displacement and rotational degrees of freedom. In ABAQUS an element behavior is characterized by five parameters:

- Family (continuum, shell, beam, truss, membrane, rigid or connector elements)
- Degrees of freedom (directly related to the element family)
- Number of nodes
- Formulation (mathematical theory or variational formulation used to define the element's behavior)
- Integration (numerical techniques used to integrate various quantities over the volume of each element, so as to allow for a complete generality in material behavior)

We have been using the S4R shell element in our works which has 4 nodes and uses a reduced integration scheme. We will present some aspects of its formulation in the following paragraphs as well as the integration particularities for this element.

4.4.1 S4R overview

The S4R element is a general purpose, conventional shell element that is valid for thick and thin shell problems and that allows for transverse shear deformation. It uses thick shell theory as the shell thickness increases and use discrete Kirchhoff thin shell elements as the thickness decreases. The transverse shear deformation becomes very small as the shell thickness decreases. Elements of type S4R account for finite membrane strains and arbitrarily large rotations; therefore, they are suitable for large-strain analysis which is why we chose this element for our analyses.

4.4.2 S4R formulation

An element's formulation refers to the mathematical theory used to define the element's behavior. All our work has been done in Lagrangian setting thus the shell element follows the deformation of the material.

At a given stage in the deformation history of the shell, the position of a material point in the shell is denoted \mathbf{x} and defined by [see Abaqus/Explicit theory manual for details]:

$$\mathbf{x}(s_i) = \bar{\mathbf{x}}(s_\alpha) + \bar{f}_{33}(s_\alpha) t_3(s_\alpha) s_3 \quad (4.39)$$

where s_α are local surface coordinates that are assumed to be orthogonal. s_3 is the coordinate in the thickness direction. The subscript i and other Roman subscripts range from one to three. Subscripts α and other lowercase Greek subscripts which describe the quantities in the reference surface of the shell range from one to two. In the above equation t_3 is the normal to the reference surface of the shell. If we consider that in the thickness, the increase factor \bar{f}_{33} is assumed to be independent of s_3 and neglecting derivatives of \bar{f}_{33} with respect to s_β we obtain the in-plane and out-of-plane gradient of the position vector as:

$$\frac{\partial x}{\partial s_\beta} = \frac{\partial \bar{x}}{\partial s_\beta} + \overline{f_{33}} \frac{\partial t_3}{\partial s_\beta} s_3, \quad \frac{\partial x}{\partial s_3} = \overline{f_{33}} t_3 \quad (4.40)$$

In the deformed state, we define local and orthonormal shell directions t_i such that:

$$t_i \cdot t_j = \delta_{ij}, \quad t_i t_j = [Id] \quad (4.41)$$

where δ_{ij} is the Kronecker delta and $[Id]$ is the identity tensor of rank 2. Summation convention is used for repeated subscripts. The in-plane components of the gradient of the position are thus obtained by projecting the gradient equation 4.19 in the tangent plane as:

$$f_{\alpha\beta} = t_\alpha \cdot \frac{\partial x}{\partial s_\beta} \quad (4.42)$$

where t_α is the normal to reference surface α . If we define the reference surface deformation gradient $\overline{f_{\alpha\beta}}$ as:

$$\overline{f_{\alpha\beta}} = t_\alpha \cdot \frac{\partial \bar{x}}{\partial s_\beta} \quad (4.43)$$

and the reference surface normal gradient $B_{\alpha\beta}$ as:

$$B_{\alpha\beta} = t_\alpha \cdot \frac{\partial t_3}{\partial s_\beta} \quad (4.44)$$

It is now possible to express the gradient of position in terms of reference surface deformation gradient and the reference surface normal gradient defined before so as to obtain:

$$f_{\alpha\beta} = \overline{f_{\alpha\beta}} + B_{\alpha\beta} \overline{f_{\alpha\beta}} s_3 \quad (4.45)$$

In the reference configuration we denote the position of a material point by X (\bar{X} for the reference surface) and the direction vectors by T_i , which yields to:

$$X(S_i) = \bar{X}(s_\alpha) + T_3(s_\alpha) s_3 \quad (4.46)$$

The gradient of the position vector is:

$$\frac{\partial X}{\partial s_\beta} = \frac{\partial \bar{X}}{\partial s_\beta} + \frac{\partial T_3}{\partial s_\beta} s_3, \quad \frac{\partial X}{\partial s_3} = T_3 \quad (4.47)$$

And, if we assume the in-plane direction vectors follow the surface coordinates, we get the in-plane components of the deformation gradient in the reference configuration:

$$f_{\alpha\beta}^0 = \delta_{\alpha\beta} + B_{\alpha\beta}^0 s_3 \quad (4.48)$$

Where $B_{\alpha\beta}^0$ is the original reference surface normal gradient defined by eqn 4.28 as:

$$B_{\alpha\beta}^0 = T_\alpha \cdot \frac{\partial T_3}{\partial S_\beta} \quad (4.49)$$

4.4.2.1 Deformation gradient

We already have obtained an expression for the deformation gradient in the reference surface, and we have assumed that the thickness change is constant:

$$\bar{F}_{\alpha\beta} = \bar{f}_{\alpha\beta} \quad \text{and} \quad \bar{F}_{33} = \bar{f}_{33} \quad (4.50)$$

At other points in the shell we obtain for the in-plane component

$$F_{\alpha\beta} = \bar{F}_{\alpha\beta} + s_3 \bar{F}_{\alpha\beta} B_{\alpha\beta} \quad (4.51)$$

which leads to :

$$F_{\alpha\beta} = (\bar{f}_{\alpha\gamma} + \bar{f}_{33} s_3 B_{\alpha\gamma})(\delta_{\gamma\beta} + s_3 B_{\gamma\beta}^0)^{-1} \quad (4.52)$$

Neglecting terms of order $(s_3)^2$ then yields the simplified relation:

$$F_{\alpha\beta} = \bar{F}_{\alpha\beta} + S_3(\bar{f}_{33} B_{\alpha\beta} - \bar{f}_{\alpha\gamma} B_{\gamma\beta}^0) \quad (4.53)$$

We can write equation 4.32 as the product of a finite-membrane deformation and a bending perturbation:

$$\begin{aligned} F_{\alpha\beta} &= [\delta_{\alpha\gamma} + s_3(\bar{f}_{33} B_{\alpha\delta} \bar{h}_{\delta\gamma} - \bar{f}_{\alpha\delta} B_{\delta\varepsilon}^0 \bar{h}_{\varepsilon\gamma})] \bar{f}_{\gamma\beta} \\ &= [\delta_{\alpha\gamma} + s_3(\bar{f}_{33} b_{\alpha\gamma} - \bar{f}_{\alpha\delta} b_{\delta\varepsilon}^0 \bar{h}_{\varepsilon\gamma})] \bar{f}_{\gamma\beta} \end{aligned} \quad (4.54)$$

If we assume that the deformation (strain and rotation) due to bending is small then,

$$s_3(\bar{f}_{33} b_{\alpha\gamma} - \bar{f}_{\alpha\delta} b_{\delta\varepsilon}^0 \bar{h}_{\varepsilon\gamma}) \ll 1 \quad (4.55)$$

We finally obtain:

$$F_{\alpha\beta} \approx \delta_{\alpha\gamma} \overline{f_{\gamma\beta}} \quad (4.56)$$

4.4.2.2 Membrane strain increment

The membrane strain increment follows from the incremental stretch tensor ΔV , whose components follow from the incremental deformation gradient $\Delta \overline{f_{\alpha\beta}}$ by the polar decomposition.

$$\Delta \overline{f_{\alpha\beta}} = \Delta \overline{V_{\alpha\gamma}} \Delta \overline{R_{\gamma\beta}} \quad (4.57)$$

Let $\overline{f_{\alpha\beta}}^t$ and $\overline{f_{\alpha\beta}}^{t+\Delta t}$ be the deformation gradient at the beginning and the end of the increment, respectively. By definition:

$$\overline{f_{\alpha\beta}}^{t+\Delta t} = \Delta \overline{f_{\alpha\delta}} \overline{f_{\delta\beta}}^t \quad (4.58)$$

The incremental deformation gradient follows as:

$$\Delta \overline{f_{\alpha\beta}} = \Delta \overline{f_{\alpha\delta}}^{t+\Delta t} \left(\overline{f}^{t-1} \right)_{\delta\beta} \quad (4.59)$$

Since $\Delta \overline{R_{\gamma\beta}}$ are the components of an orthogonal matrix, the square of the incremental stretch tensor can be obtained by:

$$\Delta \overline{f_{\alpha\gamma}} \Delta \overline{f_{\beta\gamma}} = \Delta \overline{V_{\alpha\gamma}} \Delta \overline{V_{\beta\gamma}} = \sum_{i=1}^2 (\Delta \lambda_i)^2 a_\alpha^i a_\beta^i \quad (4.60)$$

Where λ_i are incremental principal stretches and a_α^i are corresponding principal directions. The logarithmic strain increment is then:

$$\Delta \epsilon_{\alpha\beta} = \sum_{i=1}^2 \ln(\Delta \lambda_i) a_\alpha^i a_\beta^i \quad (4.61)$$

The average material rotation increment is defined from the polar decomposition:

$$\Delta \overline{R_{\alpha\beta}} = \sum_{i=1}^2 \frac{1}{\Delta \lambda_i} a_\alpha^i a_\beta^i \Delta \overline{f_{\gamma\beta}} \quad (4.62)$$

This, due to the choice of the element basic directions leads to:

$$\Delta \overline{R_{\alpha\beta}} \approx \delta_{\alpha\beta} \quad (4.63)$$

4.4.2.3 Transverse shear treatment

Several interpolation schemes have been proposed to avoid shear-locking, which typically arises as the thickness of a plate or shell goes to zero. Here we employ an assumed strain method based on the Hu-Washizu principle. For reduced integration quadrilateral and triangular shell elements that can be used for both implicit and explicit integration, this assumed strain method needs to be modified.

We summarize below the assumed strain method used with fully integrated elements, followed by the modifications required for the one-point integration plus stabilization used in Abaqus/Explicit.

4.4.2.4 Construction of the assumed strain field

Consider a typical isoparametric finite element, as depicted in Figure 4-4, and denote by A, B, C, D the set of midpoints of the element boundaries.

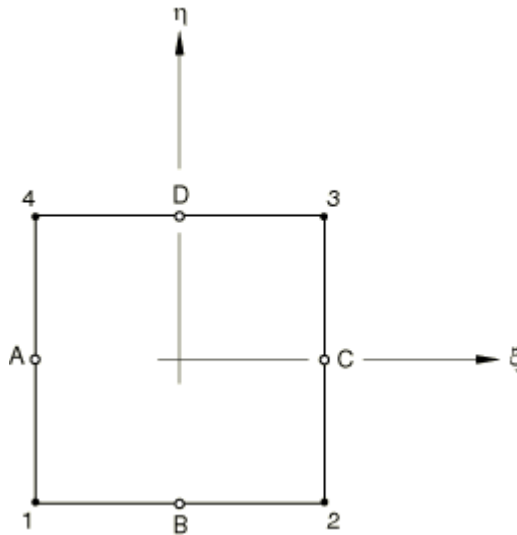


Figure 4-4: Notation for the assumed strain field on the standard isoparametric element.

The following assumed transverse shear strain field is used:

$$\begin{aligned}\bar{\gamma}_1 &= \frac{1}{2}[(1 - \eta)\gamma_1^B + (1 + \eta)\gamma_1^D] \\ \bar{\gamma}_2 &= \frac{1}{2}[(1 - \eta)\gamma_2^A + (1 + \eta)\gamma_2^C]\end{aligned}\tag{4.64}$$

where

$$\begin{aligned}\gamma_2^A &= t^A \cdot \bar{x}_2^A - T^A \cdot \bar{X}_2^A & \gamma_1^B &= t^B \cdot \bar{x}_1^B - T^B \cdot \bar{X}_1^B \\ \gamma_2^C &= t^C \cdot \bar{x}_2^C - T^C \cdot \bar{X}_2^C & \gamma_1^D &= t^D \cdot \bar{x}_1^D - T^D \cdot \bar{X}_1^D\end{aligned}\tag{4.65}$$

are the covariant transverse shear strains evaluated at the midpoints of the element boundaries. In the above transverse shear strain definitions, the use of uppercase letters indicates quantities in the reference configuration and the use of lowercase letters indicates the deformed configuration. For readability we have removed subscript 3 from the director field. Making use of the bilinear element interpolation, it follows that:

$$\begin{aligned}\bar{x}_2^A &= \frac{1}{2}(\bar{x}_4 - \bar{x}_1) & \bar{x}_1^B &= \frac{1}{2}(\bar{x}_2 - \bar{x}_1) \\ \bar{x}_2^C &= \frac{1}{2}(\bar{x}_3 - \bar{x}_2) & \bar{x}_1^D &= \frac{1}{2}(\bar{x}_3 - \bar{x}_4)\end{aligned}\tag{4.66}$$

where \bar{x}_I , for $I=1,2,3,4$, are the reference surface position vectors of the element nodes.

By making use of the assumed strain field along with the update formulae for the director field, the assumed covariant transverse shear field can be written concisely in matrix notation. Recall the director field update equation and the corresponding linearized director field:

$$t_{t+\Delta t} = \exp[\widehat{\Delta\phi}] \cdot t_t \implies \delta t = \delta\phi \times t\tag{4.67}$$

It follows from the element interpolation that:

$$\begin{aligned}\delta t^A &= \frac{1}{2}(\delta\phi_4 - \delta\phi_1) \times t^A & \delta t^B &= \frac{1}{2}(\delta\phi_2 - \delta\phi_1) \times t^B \\ \delta t^C &= \frac{1}{2}(\delta\phi_3 - \delta\phi_2) \times t^C & \delta t^D &= \frac{1}{2}(\delta\phi_3 - \delta\phi_4) \times t^D\end{aligned}\tag{4.68}$$

We now define the following vectors to be able to express the linearized transverse shear strain where $\bar{\gamma}$ is the transverse shear strain field:

$$\bar{\gamma} = \begin{Bmatrix} \bar{\gamma}_1 \\ \bar{\gamma}_2 \end{Bmatrix} \quad \delta \bar{x} = \begin{Bmatrix} \delta \bar{x}_1 \\ \delta \bar{x}_2 \\ \delta \bar{x}_3 \\ \delta \bar{x}_4 \end{Bmatrix} \quad \delta \phi = \begin{Bmatrix} \delta \phi_1 \\ \delta \phi_2 \\ \delta \phi_3 \\ \delta \phi_4 \end{Bmatrix} \quad (4.69)$$

Then, the linearized transverse shear strain is:

$$\delta \bar{\gamma} = \begin{Bmatrix} \delta \bar{\gamma}_1 \\ \delta \bar{\gamma}_2 \end{Bmatrix} = \bar{B}_{sm} \delta \bar{x} + \bar{B}_{sb} \delta \phi \quad (4.70)$$

where \bar{B}_{sm} is the in-plane part of the strain/deformation operator:

$$\bar{B}_{sm} = \frac{1}{4} \begin{bmatrix} -(1-\eta)t^{B^T} & (1-\eta)t^{B^T} & (1-\eta)t^{D^T} & -(1-\eta)t^{D^T} \\ -(1-\xi)t^{A^T} & -(1-\xi)t^{C^T} & (1-\xi)t^{C^T} & (1-\xi)t^{A^T} \end{bmatrix} \quad (4.71)$$

Define the four vectors:

$$\begin{aligned} \eta_2^A &= t^A \times \bar{x}_2^A & \eta_1^B &= t^B \times \bar{x}_1^B \\ \eta_2^C &= t^C \times \bar{x}_2^C & \eta_1^D &= t^D \times \bar{x}_1^D \end{aligned} \quad (4.72)$$

Then the rotation or bending part of the strain/displacement operator is written:

$$\bar{B}_{sb} = \frac{1}{4} \begin{bmatrix} (1-\eta)\eta_1^{B^T} & (1-\eta)\eta_1^{B^T} & (1-\eta)\eta_1^{D^T} & (1-\eta)\eta_1^{D^T} \\ (1-\xi)\eta_2^{A^T} & (1-\xi)\eta_2^{C^T} & (1-\xi)\eta_2^{C^T} & (1-\xi)\eta_2^{A^T} \end{bmatrix} \quad (4.73)$$

4.4.2.5 Constitutive relations

A St. Venant-Kirchhoff constitutive model for the Kirchhoff curvilinear components of the resultant transverse shear force is written in terms of the transverse shear strains as:

$$\begin{Bmatrix} Q^1 \\ Q^2 \end{Bmatrix} = C_s \begin{Bmatrix} \bar{\gamma}_1 \\ \bar{\gamma}_2 \end{Bmatrix} \quad (4.74)$$

where C_s is the transverse shear stiffness in curvilinear coordinates. For a single isotropic layer we get:

$$C_s = \frac{5}{6} G_s h \begin{bmatrix} A^{11} & A^{12} \\ A^{21} & A^{22} \end{bmatrix} \quad (4.75)$$

The matrix $[A^{\alpha\beta}]$ is the inverse of the metric $[A_{\alpha\beta}]$, where metric components in the reference configuration $A_{\alpha\beta}$ are defined by the inner product:

$$A_{\alpha\beta} = \bar{X}_\alpha \cdot \bar{X}_\beta \quad (4.76)$$

The Cauchy or true transverse shear force components in the shell orthonormal coordinate system $\{q^1, q^2\}^T$ are calculated with the coordinate transformation $f_\alpha^a = \partial s^\alpha / \partial \xi^a$ as:

$$q = \begin{Bmatrix} q^1 \\ q^2 \end{Bmatrix} = \frac{A}{a} \begin{bmatrix} f_1^1 & f_2^1 \\ f_1^2 & f_2^2 \end{bmatrix} \begin{Bmatrix} Q_1 \\ Q_2 \end{Bmatrix} \quad (4.77)$$

where A is the element's reference area and a is the current area.

4.4.3 In-plane displacement hourglass control

The in-plane displacement hourglass control is applied in the same way as in the Abaqus/Explicit membrane elements. The hourglass strains are defined by:

$$z_\alpha = \frac{\partial \bar{x}}{\partial S_\alpha} \cdot \bar{x}^I \gamma^I - \frac{\partial \bar{X}}{\partial S_\alpha} \cdot \bar{X}^I \gamma^I = \frac{\partial \bar{x}}{\partial S_\alpha} \cdot \bar{x}^I \gamma^I - T_\alpha \cdot \bar{X}^I \gamma^I \quad (4.78)$$

where γ^I is the hourglass mode. This mode is obtained by making the “regular” hourglass mode $\Gamma^I = \{1, -1, 1, -1\}$ orthogonal to the homogeneous deformation mode in the undeformed shape of the element. This last condition can be written as:

$$\gamma^I = \Gamma^I - \Gamma^J X^J \cdot T_\beta \frac{\partial N^I}{\partial S_\beta} \quad (4.79)$$

Observe that:

$$T_\alpha \cdot \bar{X}^I \gamma^I = T_\alpha \cdot \bar{X}^I \Gamma^I - \Gamma^J \bar{X}^J \cdot T_\alpha = 0 \quad (4.80)$$

and consequently:

$$z_\alpha = \frac{\partial x}{\partial S_\alpha} \cdot \bar{x}^I \gamma^I \quad (4.81)$$

This expression can be worked out further. We define the projected nodal coordinates:

$$S_\alpha^I = T_\alpha \cdot \bar{X}^I \quad (4.82)$$

and the projected element area:

$$A = \frac{1}{2} [(S_1^3 - S_1^1)(S_2^4 - S_2^2) + (S_1^2 - S_1^4)(S_2^3 - S_2^1)] \quad (4.83)$$

The hourglass mode can then be written in the form:

$$\begin{aligned} \gamma^1 &= \frac{1}{A} [S_1^2(S_2^3 - S_2^4) + S_1^3(S_2^4 - S_2^2) + S_1^4(S_2^2 - S_2^3)] \\ \gamma^2 &= \frac{1}{A} [S_1^3(S_2^1 - S_2^4) + S_1^4(S_2^3 - S_2^1) + S_1^1(S_2^4 - S_2^3)] \\ \gamma^3 &= \frac{1}{A} [S_1^4(S_2^1 - S_2^2) + S_1^1(S_2^2 - S_2^4) + S_1^2(S_2^4 - S_2^1)] \\ \gamma^4 &= \frac{1}{A} [S_1^1(S_2^3 - S_2^2) + S_1^2(S_2^1 - S_2^3) + S_1^3(S_2^2 - S_2^1)] \end{aligned} \quad (4.84)$$

The hourglass stiffness is chosen equal to:

$$K_h = (r_F G) \frac{\partial N^I}{\partial S_\beta} \frac{\partial N^I}{\partial S_\beta} hA \quad (4.85)$$

where G is the shear modulus and r_F is a small number chosen to be 0.005 in Abaqus/Explicit/Standard and 0.05 in Abaqus/Explicit/Explicit. When the hourglass control is based on assumed enhanced strain, the artificial stiffness factor is replaced by coefficients derived from a three-field variational principle. The hourglass force Z conjugates to z is then equal to:

$$Z_\alpha = K_h z_\alpha \quad (4.86)$$

For virtual work we need the first variation of the hourglass strain. From the expression for the strain follows immediately:

$$\delta z_\alpha = \frac{\partial \bar{x}}{\partial S_\alpha} \cdot \delta \bar{x}^I \gamma^I + \frac{\partial \delta \bar{x}}{\partial S_\alpha} \cdot \bar{x}^I \gamma^I \quad (4.87)$$

Note that the second term is not accounted for in the initial configuration since $\bar{X}^I \gamma^I = 0$. The second variation is needed for the Jacobian. From the first variation follows right away:

$$d\delta z_\alpha = \frac{\partial d\bar{x}}{\partial S_\alpha} \cdot \delta \bar{x}^I \gamma^I + \frac{\partial \delta \bar{x}}{\partial S_\alpha} \cdot d\bar{x}^I \gamma^I \quad (4.88)$$

The second variation does not contribute in the initial configuration since initially $Z_\alpha = 0$.

4.4.4 Rotational hourglass control

The expressions for the curvature change, the transverse shear constraints, and the drilling mode constraints still leave three non-homogeneous rotational modes unconstrained. These modes correspond to zero rotation at the mid-edges and zero gradient at the centroid. Hence, they correspond to the familiar $\Gamma^I = \{1, -1, 1, -1\}$ hourglass pattern. To pass curvature patch tests exactly, it is necessary to use orthogonalized hourglass patterns as derived for in-plane hourglass control.

4.4.5 Parametric interpolation

The position of the points in the shell reference surface is described in terms of discrete nodal positions with parametric interpolation functions noted $N^I(\xi_\alpha)$. The functions are continuous, and ξ_α are non-orthogonal, non-distance measuring parametric coordinates. For the reference surface positions one, thus, obtains:

$$\bar{X}(\xi_\alpha) = N^I(\xi_\alpha)\bar{X}^I \quad (4.89)$$

The gradients of the position with respect to ξ_β are:

$$\frac{\partial \bar{X}}{\partial \xi_\beta} = \frac{\partial N^I}{\partial \xi_\beta} \bar{X}^I \quad (4.90)$$

Note that uppercase Roman superscripts such as I denote nodes of an element and that repeated superscripts imply summation over all nodes of an element. Now consider the original configuration. The unit normal to the shell reference surface is readily obtained as:

$$T_3 = \frac{\frac{\partial \bar{X}}{\partial \xi_1} \times \frac{\partial \bar{X}}{\partial \xi_2}}{\left| \frac{\partial \bar{X}}{\partial \xi_1} \times \frac{\partial \bar{X}}{\partial \xi_2} \right|} \quad (4.91)$$

Subsequently, we define two orthonormal tangent vectors T_α and distance measuring coordinates S_α along these vectors. The derivatives of these coordinates with respect to ξ_β follow from:

$$\frac{\partial \bar{S}_\alpha}{\partial \bar{\xi}_\beta} = T_\alpha \cdot \frac{\partial \bar{X}}{\partial \bar{\xi}_\beta} = T_\alpha \cdot \bar{X}^I \frac{\partial N^I}{\partial \bar{\xi}_\beta} \quad (4.92)$$

The gradient of $\bar{\xi}_\alpha$ with respect to S_β is readily obtained by inversion:

$$\frac{\partial \bar{\xi}_\alpha}{\partial S_\beta} = \left[\frac{\partial \bar{S}_\alpha}{\partial \bar{\xi}_\beta} \right]^{-1} \quad (4.93)$$

which makes it possible to obtain the gradient operator:

$$\frac{\partial N^I}{\partial S_\beta} = \frac{\partial N^I}{\partial \bar{\xi}_\alpha} \frac{\partial \bar{\xi}_\alpha}{\partial S_\beta} \quad (4.94)$$

The original reference surface normal gradient is obtained from the nodal normals T_3^I with:

$$B_{\alpha\beta}^0 = T_\alpha \cdot T_3^I \frac{\partial N^I}{\partial S_\beta} \quad (4.95)$$

Since the original reference surface normal gradient is obtained by taking derivatives with respect to orthogonal distance measuring coordinates, we will call $B_{\alpha\beta}^0 = b_{\alpha\beta}^0$ the original curvature of the reference surface.

Orientation update and curvature change are discussed in details in Abaqus/Explicit theory manual (41).

4.4.6 The rate of virtual work

To obtain an expression for the rate of virtual work, we first write the virtual work equation in terms of the reference volume:

$$\delta \Pi = \int_{V^0} \tau_{\alpha\beta} \delta \varepsilon_{\alpha\beta} dV^0 = \int_{A^0} \int_h \tau_{\alpha\beta} \delta \varepsilon_{\alpha\beta} dS_3 dA^0 \quad (4.96)$$

where $\tau_{\alpha\beta}$ is the Kirchhoff stress tensor, related to the Cauchy or true stress tensor via:

$$\tau_{\alpha\beta} = J \sigma_{\alpha\beta} \quad (4.97)$$

The rate of change then becomes:

$$d\delta\Pi = \int_{A^0} \int_h (d^\nabla \tau_{\alpha\beta} \delta\varepsilon_{\alpha\beta} + \tau_{\alpha\beta} d^\nabla \delta\varepsilon_{\alpha\beta}) dS_3 dA^0 \quad (4.98)$$

Here d^∇ indicates that the rates are taken in a material, corotational coordinate system. The terms involving stress rates are related to the material behavior. We assume constitutive equations of the form:

$$d^\nabla \tau_{\alpha\beta} = J C_{\alpha\beta\gamma\delta} d\varepsilon_{\delta\gamma} \quad (4.99)$$

Substituted in the expression $d\delta\Pi$ and transformed back to the current configuration, this yields:

$$d\delta\Pi = \int_{A^0} \int_h (\delta\varepsilon_{\alpha\beta} C_{\alpha\beta\gamma\delta} d\varepsilon_{\delta\gamma} + \sigma_{\alpha\beta} d^\nabla \delta\varepsilon_{\alpha\beta}) \bar{f}_{33} dS_3 dA \quad (4.100)$$

Consistent with the derivation of the virtual work equation itself, we neglect terms of the order $d\bar{f}_{33} S_3 \delta\kappa_{\alpha\beta}$. Hence, the rate of virtual work can be written as:

$$d\delta\Pi = \int_{A^0} \left[\int_h (\delta\bar{\varepsilon}_{\alpha\beta} + \bar{f}_{33} S_3 \delta\kappa_{\alpha\beta}) C_{\alpha\beta\gamma\delta} (\delta\bar{\varepsilon}_{\gamma\delta} + \bar{f}_{33} S_3 d\kappa_{\alpha\beta}) \bar{f}_{33} dS_3 + N_{\alpha\beta} d^\nabla \delta\bar{\varepsilon}_{\alpha\beta} + M_{\alpha\beta} d^\nabla \delta\kappa_{\alpha\beta} \right] dA \quad (4.101)$$

Hence one needs to compute the second variation of the membrane strain $d^\nabla \delta\bar{\varepsilon}_{\alpha\beta}$ and of the curvature strain $d^\nabla \delta\kappa_{\alpha\beta}$.

4.4.7 Numerical integration

S4R elements use a reduced integration scheme and there is only one point of integration in this Abaqus/Explicit element which is integrated numerically.

From the virtual work expression the volume integral will be replaced by a summation:

$$\int_V \sigma : \delta D dV \rightarrow \sum_{i=1}^n \sigma_i : \delta D_i V_i \quad (4.102)$$

where n is the number of integration points in the element and V_i is the volume associated with integration point i . Abaqus/Explicit will use either “full” or “reduced” integration. For full integration the number of integration points is sufficient to integrate the virtual work expression

exactly, at least for linear material behavior. All triangular and tetrahedral elements in Abaqus/Explicit use full integration. Reduced integration can be used for quadrilateral and hexahedral elements; in this procedure the number of integration points is sufficient to integrate exactly the contributions of the strain field that are one order less than the order of interpolation. The (incomplete) higher-order contributions to the strain field present in these elements will not be integrated.

The advantage of the reduced integration elements is that the strains and stresses are calculated at the locations that provides optimal accuracy, the so-called Barlow points. A second advantage is that the reduced number of integration points decreases CPU time and storage requirements. The disadvantage is that the reduced integration procedure can admit deformation modes that cause no straining at the integration points. These zero-energy modes make the element rank-deficient and cause a phenomenon called “hourglassing”.

For reduced-integration elements the transverse shear force components need to be evaluated at the center of the elements. Consider π_s the transverse shear contribution to the internal energy:

$$\pi_s = \frac{1}{2} \int \bar{\gamma} \cdot C_s \cdot \bar{\gamma} dA \quad (4.103)$$

The reference area measure dA is written in terms of the isoparametric coordinates as

$dA = J d\xi d\eta$, where $J = \sqrt{A_{11}A_{22} - (A_{12})^2}$ and $A_{\alpha\beta}$ are the components of the reference surface metric in the undeformed configuration.

This transverse shear energy can be approximated in many ways to produce one point integration at the center of the element plus hourglass stabilization. It is important that this treatment yields accurate representation of transverse shear deformation in thick shell problems and provide robust performance for skewed elements. The treatment should collapse smoothly to a triangle, which should be insensitive to the node numbering during collapse; that is, the triangle's response should not depend on the nodal connectivity. For an entire mesh of triangular elements, the treatment should give convergent results (that is, the element should not lock). Furthermore, the high frequency response of the transverse shear treatment should be controlled so that transverse shear response does not dominate the stable time increment for explicit

dynamic analysis (including for skewed triangular or quadrilateral geometries). All of these requirements are embodied in the following transverse shear treatment.

Define the transverse shear strain at the center of the element (the homogeneous part) and the “hourglass” transverse shear strain vectors as:

$$\bar{\gamma}_0 = \frac{1}{2} \begin{Bmatrix} \gamma_1^B + \gamma_1^D \\ \gamma_2^A + \gamma_2^C \end{Bmatrix} + \gamma_{cc} \begin{Bmatrix} c_\xi \\ c_\eta \end{Bmatrix} \quad \text{and} \quad \gamma_{hg} = \begin{Bmatrix} \gamma_{bf} \\ \gamma_{cc} \end{Bmatrix} \quad (4.104)$$

The element distortion coefficients c_ξ and c_η are constants determined by the element reference geometry. For geometries with constant Jacobian transformation we have $c_\xi = c_\eta = 0$. The components of the hourglass strain vector γ_{hg} are defined in terms of the edge strains as:

$$\gamma_{bf} = -\Gamma_A \gamma_2^A + \Gamma_B \gamma_1^B + \Gamma_C \gamma_2^C - \Gamma_D \gamma_1^D \quad (4.105)$$

and,

$$\gamma_{cc} = -\gamma_2^A + \gamma_1^B + \gamma_2^C - \gamma_1^D \quad (4.106)$$

The coefficients $\Gamma_A, \Gamma_B, \Gamma_C, \Gamma_D$ are constants determined from the reference geometry of the element. For rectangular elements $\Gamma_A = \frac{1}{2}, \Gamma_B = -\frac{1}{2}, \Gamma_C = \frac{1}{2}, \Gamma_D = -\frac{1}{2}$ and γ_{bf} can be identified as the strain associated with the rotational deformation pattern. We call γ_{cc} the deformation pattern that resembles the sweeping over the element normals in a circular pattern. We defined the reference element area to be A_0 . The transverse shear energy can be approximated as a center point value plus a stabilization term:

$$\pi_s = \frac{1}{2} A_0 \bar{\gamma}_0 \cdot C_{s0} \cdot \bar{\gamma}_0 + \frac{1}{2} A_0 \gamma_{hg} \cdot H \cdot \gamma_{hg} \quad (4.107)$$

where C_{s0} is the transverse shear stiffness evaluated at the center of the element and the hourglass stiffness H is the diagonal matrix

$$H = \frac{C_{s0}^{eff}}{12} \begin{bmatrix} 1 & 0 \\ 0 & 0.001 \end{bmatrix} \quad (4.108)$$

The effective stiffness C_{s0}^{eff} is the average direct component of the transverse shear stiffness.

$$C_{s0}^{eff} = \frac{(C_{s0}^{11} + C_{s0}^{22})}{2} \quad (4.109)$$

The formulation of the homogeneous part of the transverse shear has two contributions: the average edge strain across the element, plus the element distortion term. The average strain treatment is essentially the same as that for the assumed strain formulation of MacNeal and others presented earlier, with expressions evaluated at the center of the element ($\xi = 0$ and $\eta = 0$). The details of this part are omitted; only the element distortion term is presented in detail.

The variation of the homogeneous transverse shear strain can be written:

$$\delta\bar{\gamma}_0 = \bar{B}_{sm0}\delta\bar{x} + \bar{B}_{sb0}\delta\phi + \bar{B}_{ccd}\delta\bar{x} + \bar{B}_{ccr}\delta\phi \quad (4.110)$$

where \bar{B}_{sm0} and \bar{B}_{sb0} are \bar{B}_{sm} and \bar{B}_{sb} evaluated at the center of the element. The stabilization term has a similar formulation. The variation of the hourglass strain is:

$$\delta\gamma_{hg} = \bar{B}_a\delta\bar{x} + \bar{B}_r\delta\phi \quad (4.111)$$

4.5 Conclusion

In this chapter, we overviewed the principal numerical tools that we have to use in all our work. First we gave the basics of explicit dynamic formulation and computation process that is used by Abaqus. The VUMAT subroutine description was explained to provide a framework in which we have to set our model computations. In this description we put emphasis on the updating of the Green-Nahgdi frame as well as the yarns orientation. Also it was crucial to understand what variables were passed into the VUMAT to feed our computations and how we should return our results to Abaqus. We ended by focusing especially on the S4R shell element in this chapter. The formulation of S4R in explicit dynamic with reduced integration was given in great details, it is the core of our work and our VUMAT is tailored to be used in conjunction with this particular element.

CHAPTER 5 - DEVELOPMENT AND TESTING OF THE 3D CROSSOVER MODEL

The goal of the present model development and testing is to capture the biaxial tensile and compressive response of a representative unit cell (RUC) of a plain weave fabric in order to obtain equivalent material parameters to be fed into the biaxial tensile and compressive response of an equivalent representative smeared shell element. Specific parameters which are geometry and material dependent are needed to be used afterward as inputs data for the VUMAT subroutine. First a virtual testing approach is thus used in order to obtain the E, Nu and G values from the FE analysis. Simple virtual uniaxial and shear tests are used to determine the required parameters and numerical results obtained are compared with experimental values given by Shahkarami et al (4). Essentially, using these preliminary tests to obtain the numerical values of E, Nu and G , the intent was to validate the behavior of the RUC before moving on to stage of obtaining two fundamental parameters a and b (to be defined in the following pages) describing the compressive behavior of the representative unit cell. They are found by using a virtual transverse compression test.

And then experimental data used by Shahkarami et al (4) was used to ensure good model accuracy and to validate the response of the model for further testing. Since our goal was not to use a very refined model, we therefore only modeled the yarn geometry according to the examples of representative unit cells shown in the literature (4) and we implemented the Kevlar mechanical properties using Abaqus. This type of analysis is not weave-dependent so it can be applied to any weave structure provided that the right representative volume element is chosen.

5.1 Model basics

The model is based on the representation of a single yarn crossover in which the yarns are modeled by using an 8-node brick element with reduced integration available in Abaqus element library. First the geometry is created in the Abaqus/CAE software and then the meshing was applied on it automatically by Abaqus.

To correctly define the geometry of a yarn, we made some basic assumptions regarding the longitudinal profile of the yarn and its cross-section. These assumptions derive from the study of micro-images of the plain weave fabric that can be found in reference (2). As a result, first it is assumed that the cross-sectional shape of the yarn is mostly lenticular although many authors also use the elliptical section type. Also, it is assumed that the yarn longitudinal profile follows a sinusoidal path. In his work, Durville (10) has described the yarns as exhibiting a variation of the cross-sectional area and shape along its longitudinal path. This issue was not taken into account in our simulation since it is a more complex problem to handle. We wanted to keep a simple model because dealing with a very refined model will not lead to a meaningful change regarding the values and parameters we want to extract from the model. This is also why we considered that the fill and warp yarns have the same geometrical properties. Finally, we assumed that while under tensile loading, the change in cross-sectional shape of a yarn is negligible.

The key to the success in modeling a 3D yarn crossover unit cell is to capture the true response of each individual yarns composing the crossover as well as the specific interaction phenomenon between them. This translates into the fact that not only the geometry must be properly accounted for but also that the mechanical properties we use are valid. In finite

element analysis, the lack of meaningful mechanical properties may cause instabilities that lead to spurious modes of deformation. Therefore, if the results that one could extract from these virtual tests and that are to be fed in the VUMAT program are inaccurate this would cause inaccuracies in the results given by the shell element. Spurious modes usually appear for strongly orthotropic material as are the Kevlar yarns. Boisse et al. (24) state that “because some rigidities are nearly equal to zero, some numerical instabilities often appear and this can be avoided by Hourglass control”. In other words, the lack of sufficient shear stiffness for example will often lead to unstable element shapes especially if reduced integration elements are to be used as in our model. As such a problem was encountered, it was found that a possible solution is to use the hourglass-control stiffness contribution to the element stiffness which would eliminate the associated hourglass modes of deformation. However, the induced hourglass energy should be kept to a small amount compared to the total energy of the model.

Throughout the literature review, the following mechanical considerations have been retained and taken into account while defining the 3D models:

- First, the yarns exhibit a high axial stiffness in tension and can support almost no load in compression because buckling appears instantly.
- Secondly, the lack of bonding between the fibers that constitute the yarn translates into near zero shearing or bending stiffness in the yarn.
- Lastly, the presence of voids between fiber bundles and their possible relative motion leads to an extremely complex non-linear response.

The yarns show strong overall orthotropic characteristics and their behavior can be considered isotropic in the transverse direction in Abaqus. In our model, we assumed that the axial and transverse responses of the yarns are completely decoupled and we therefore set the Poisson’s ratio to a very low value.

5.2 3D model definition of the unit cell

5.2.1 Geometrical definition

The geometric properties were taken from the document detailing the input parameters of Shahkarami’s LS-Dyna based UMAT model (42) which studied the plain weave fabric made of Kevlar reinforcements. In his work, two different set of geometrical properties for the fill and warp yarns were considered, but in our case, the two crossing yarns having the same geometry will be considered. In the next paragraphs, two key aspects of the yarn geometry are described in details: (i) the yarns’ centerline profile and (ii) their cross-sectional shape.

The profile of the centerline is given by equation 5.1 from reference (4) and is shown in Figure 5-1.

$$f(x_i) = h_i \cdot \cos\left(\frac{\pi}{2w_i} x_i\right) \quad (5.1)$$

Where h_i is the height of the yarn centerline at the center of the unit cell which is the point where the yarns cross each other at $x_i=0$.

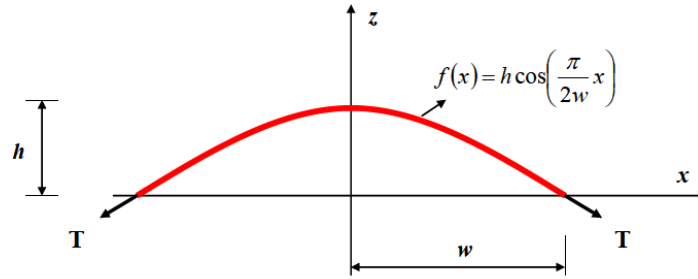


Figure 5-1: Cosine-based shape of an arbitrary yarn in a plain weave fabric (4)

The unit-cell half width is denoted by w_i (in mm) and can be calculated from the thread count of the crossing yarns m_j (in threads/mm) using:

$$2w_i = \frac{1}{m_i} \quad (5.2)$$

The initial value of h_{0i} can be calculated mathematically from the crimped length of the yarn called S_i depending on the unit-cell’s total length x in equation 5.3:

$$S_i = 2 \int_0^{w_i} \sqrt{1 + \left(\frac{\pi h_i}{2w_i}\right)^2 \sin^2\left(\frac{\pi}{2w_i}x\right)} dx \quad (5.3)$$

Knowing the value cr_i , of crimp observed in the fabric, the initial length of the yarn is given by:

$$S_{0i} = 2w_i(1 + cr_i) \quad (5.4)$$

Using equation 5.3 and 5.4 we obtain the non-linear equation needed to solve for the value of h_{0i} (4):

$$w_i(1 + cr_i) = \int_0^{w_i} \sqrt{1 + \left(\frac{\pi h_i}{2w_i}\right)^2 \sin^2\left(\frac{\pi}{2w_i}x\right)} dx \quad (5.5)$$

A Maple program was created (shown in Appendix A) in order to calculate the result of this equation given the thread count per millimeter of the type of yarn used and the crimp of the fabric. Each calculated value is summarized in Table 5-1.

From the value of h_i , it is then possible to evaluate the thickness of the yarn and therefore the total thickness of the shell element. If we assume that the point where the two fibers come in contact is located at $z=0$ then we can consider that the value h_i is half the yarn's thickness. Therefore the yarn thickness has a value of $2h_i$ and the shell thickness is $4h_i$.

Table 5-1: Geometrical parameters of the RVE defined in Abaqus/CAE

Properties	Values
Thread count per inch	27
Crimp (for 2% take 0.02)	0.0421
Yarn width (mm)	0.9407
Initial value of h_i (mm)	0.12495
Yarn thickness (mm)	0.2499
Unit-cell length (mm)	0.9407
Shell thickness (mm)	0.4998

These values were used in Maple to plot the yarn’s cross-sectional curve using the sinusoidal function 5.1 to obtain the profile shown in Figure 5-2.

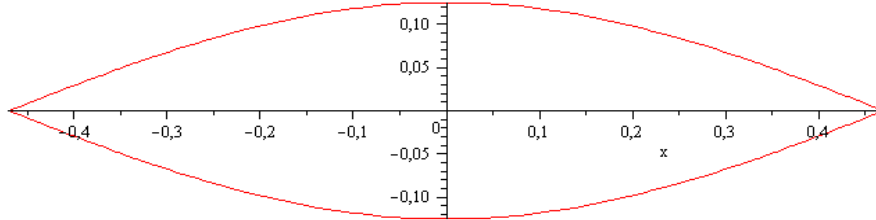


Figure 5-2: Initial lenticular shape of the yarns’ cross-sectional area

Using this shape plotted in Maple, we extracted the coordinates of a set of 20 key points to be exported in Abaqus/CAE for the generation of CAD geometry. One should also mention that this lenticular shape has led to the creation of a mesh displaying distorted element. The distorted elements were located at extremities of the cross-section where the sinusoidal curves intersect. Therefore, these sharp edges have been trimmed to obtain a line edge instead of sharp one, thus allowing Abaqus to generate a regular solid element mesh without distorted elements at each end of the yarn’s cross-section as it can be seen in Figure 5-3.

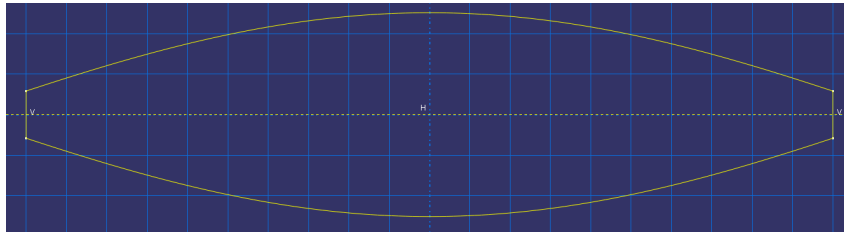


Figure 5-3: Modified lenticular shape of the yarns’ cross-sectional area

The next step in creating the yarn geometric model is to define the undulation path which can also be represented by a sinusoidal path given by equation 5.1. Using the same formula as the one defining the yarn cross-section has the advantage of generating a yarn that can easily be assembled within Abaqus. Consequently, instead of having a small area of contact between the two yarns, we obtain contact over a large surface which is what researchers have been observing. Ultimately the yarn three-dimensional geometry presented in Figure 5-4 is obtained.

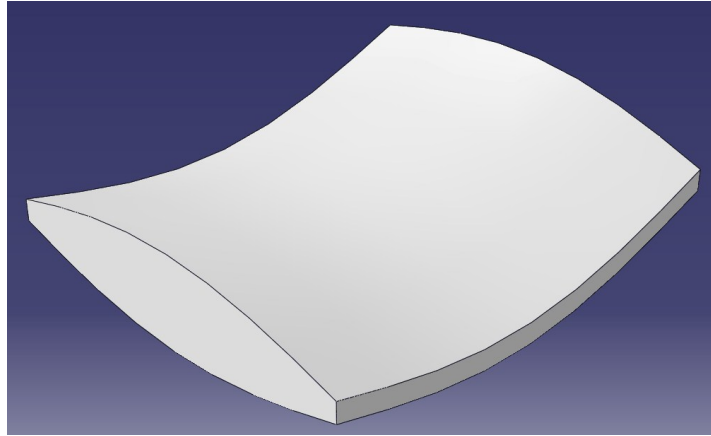


Figure 5-4: Undulated shape of one yarn in Abaqus

Shahkarami (4) introduces a gap parameter to define the distance between two adjacent yarns of the same family. In order to simplify the problem, this gap parameter has been set to zero throughout this work.

5.2.2 Mechanical definition of the model

The mechanical definition of the yarns' behavior is quite easy to set up. In Abaqus, we defined a purely linear-elastic orthotropic (or more precisely transversely isotropic) material with a unique material direction being aligned with the yarn axis direction. The properties of Kevlar yarns used can be found in the work of Grujicic (1). These values match the ones used in the LS-Dyna user material model input file of Shahkarami (42). These properties are summarized in Table 5-2.

Table 5-2: Mechanical parameters of the RVE defined in Abaqus/CAE

Properties	Values
Young modulus in longitudinal direction of the yarn, E_{11} (GPa)	96.0
Young modulus in transverse direction of the yarn, E_{22} (GPa)	3.28
Young modulus in transverse direction of the yarn, E_{33} (GPa)	3.28
In-plane shear / transverse shear modulus G_{12}, G_{23}, G_{13} (GPa)	3.28
Poisson ratio, $\nu_{12}, \nu_{23}, \nu_{13}$	0
Density, ρ (g/mm ³)	1,44

The Young modulus of the two transverse normals, the shear moduli and the Poisson ratios are set to low values. This is because of the fibers bundled within the yarns are only weakly coupled with each other (4). Furthermore, in the numerical tests we conducted on the crossover model, these values have very little influence on the results considering the deformation modes we want to probe. Also, we could not set these values to zero as we would obtain instabilities during the analysis and non-physical deformation of the finite elements; therefore these values are taken to be very small compared to the axial stiffness.

Having tried multiple boundary conditions cases to correctly constrain the yarns, we finally selected the following one as being the best at limiting the yarns' displacements without generating unwanted strains or stresses inside the model.

- The first yarn we need to constrain is the one on which we apply the forced displacement of 0,01 millimeters. This displacement is along direction one of the unit cell, meaning it is applied on one extremity of the moving yarn (i.e. to the cross sectional surface of the yarn in Abaqus model) along its principal direction. All other displacements in the remaining directions of space and all rotations at the two extremities are not allowed and hence they are set to zero.
- The other yarn is also constrained at its extremities. First, displacements are authorized in direction two which is the direction along that yarn's length. Other displacement in the two other directions of space and all rotation are not allowed, they are set to zero.

During the application of the displacement, we observed an extension of the yarn on which the forced displacement is applied. It leads to a straightening of that yarn and the occurrence of a tension inside it. The curvature of the overlapping yarn's centerline is increasing because it is pushed by the straightening of the first yarn. The contact point between the crossing yarns is moving out of the plane.

Finally, the contact between the fibers is modeled using the 'general contact' option available in Abaqus.

5.3 Testing of the fabric unit-cell

The 3D crossover model made of solid elements has to be tested in order to obtain the mechanical parameters to be implemented in the user subroutine. The crossover model created in Abaqus is presented in Figure 5-5.

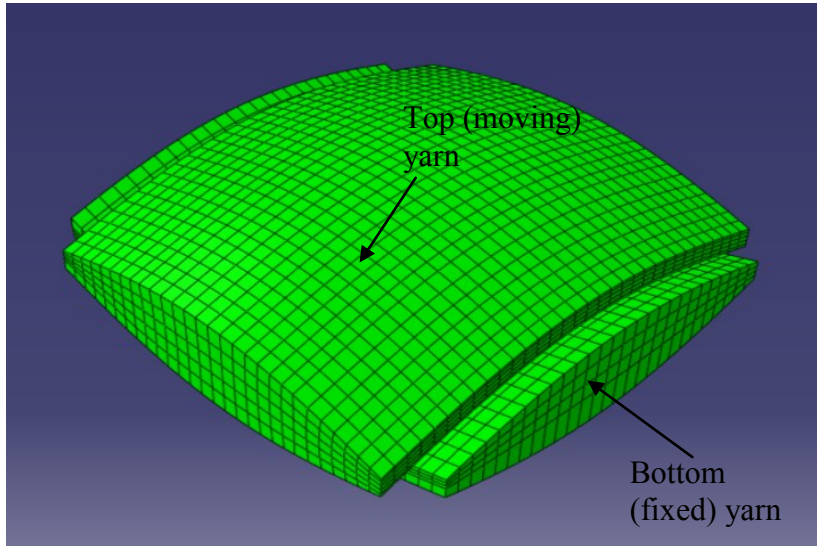


Figure 5-5: Crossover model in Abaqus

The mechanical parameters to be determined are:

- Young modulus in direction 1: E_1 ,
- Young modulus in direction 2: E_2 ,
- In-plane Poisson's ratio: ν_{12} ,
- Compression parameters a and b.

We have subjected the unit-cell geometry to a uniaxial traction test, a transverse compression test and a shear test; the details of the behavior of the unit cell in each case are given in the next paragraphs.

5.3.1 Extensional response of the unit-cell

This test is meant to measure the extensional response of the unit cell. This is done on only one direction at a time. Since the model is totally geometrically symmetric, only one test has been

carried out. Obviously the results we obtain in the direction we tested (direction 1) apply for the other direction (direction 2). A visualization of the undeformed and deformed configuration is presented in Figure 5-6 and puts emphasis on the displacements.

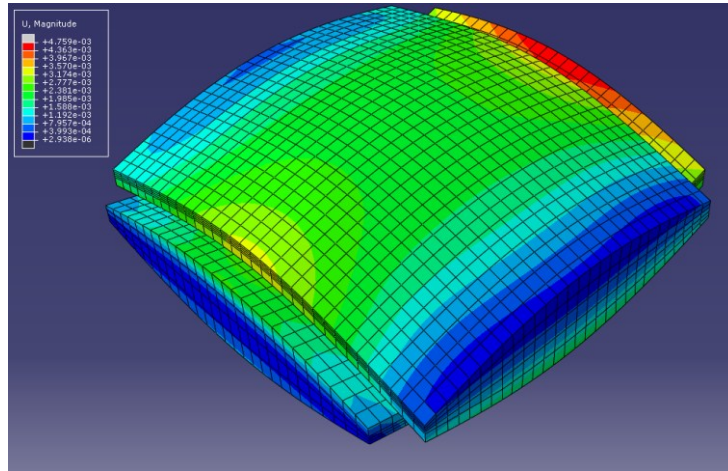


Figure 5-6: Biaxial extension of the crossover (magnitude of displacements U)

In Figure 5-6 we extracted the displacement magnitude, we can observe that the maximum displacement value appears at the end of the yarn where the displacement boundary condition is applied. Also the displacements are large at the middle portion of the yarns (in green in Figure 5-6) and this is because of the new equilibrium position of the contact surface. In this case, because the non-zero displacement boundary condition is applied on one yarn and the other yarn ends are fixed in space the point of equilibrium moves out of plane. Thus, during the analysis the moving yarn is straightening while the other one is bending. Figure 5-6, showing the magnitude of the displacements, enables us to verify that the simple predicted crossover behavior is reproduced by the software.

We choose to select the results from elements selected at the middle of the yarn and remove those affected by the boundary conditions at the end of each yarn. This method was chosen to give us the opportunity to verify that the values for strain and stress are globally correct on the yarn. From these results we plotted the curve presented in Figure 5-7. The red curve shows the best fit with respect to the blue curve showing the numerical results taken from the 3D crossover model. R^2 is the correlation coefficient between the two curves.

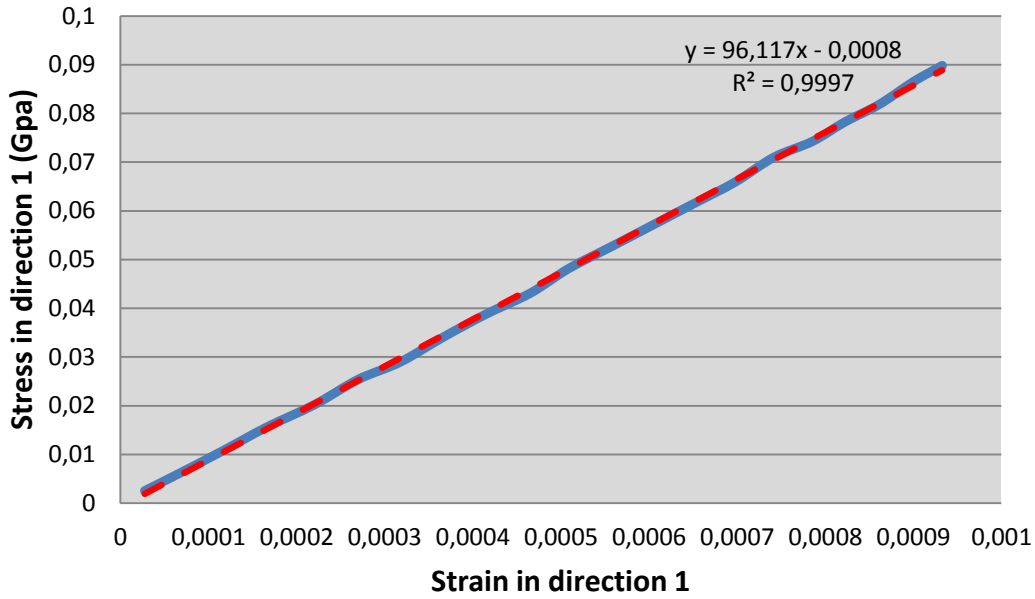


Figure 5-7: Stress-strain relationship in direction one for the 3D crossover

According to the theory, the engineering Young modulus in direction one is given by the following equation:

$$E_1 = \frac{\sigma_1}{\varepsilon_1} \quad (5.6)$$

This shows that the engineering modulus to be assigned as a VUMAT input in this direction is 96,117 GPa which is, as expected, a value very close to the yarn modulus. Then, we calculated the in-plane Poisson's ratio by extracting from the model the strains in both directions one and two. Poisson ratio is given by equation:

$$\nu = -\frac{\varepsilon_2}{\varepsilon_1} \quad (5.7)$$

This enabled us to plot the strain in direction two versus the strain in direction 2 as shown in Figure 5-8.

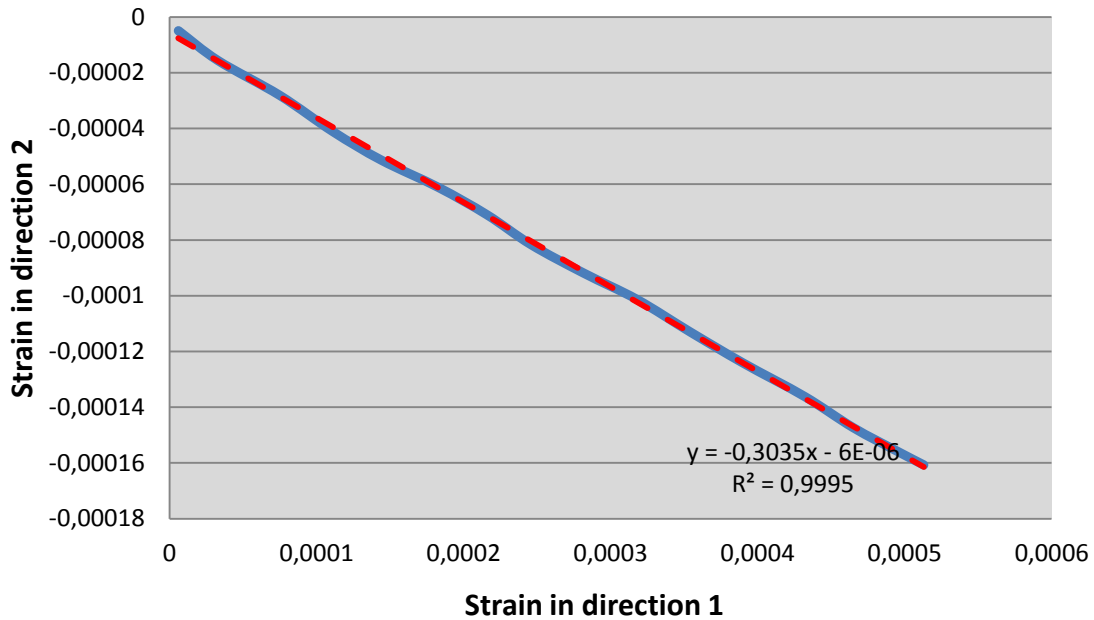


Figure 5-8: Strain relationship for Poisson ratio

Finally, we obtain a Poisson's ratio for the unit cell of approximately 0.30 which will be used as an input for the VUMAT.

5.3.2 Transverse compression of the unit cell

The boundary conditions here are simpler to set up than in the previous model. Indeed, for the two yarns' extremities, the only displacements authorized are along each yarn's principal direction. The application of the compression force along the transverse direction is done by creating a rigid surface in Abaqus on the top of the 3D crossover model on which we apply a maximum force of 3000 mN that will compress the yarns. Another rigid surface is defined under the crossover point to support the compression that is applied.

The model created in Abaqus to model the compression of the yarns is shown in Figure 5-9.

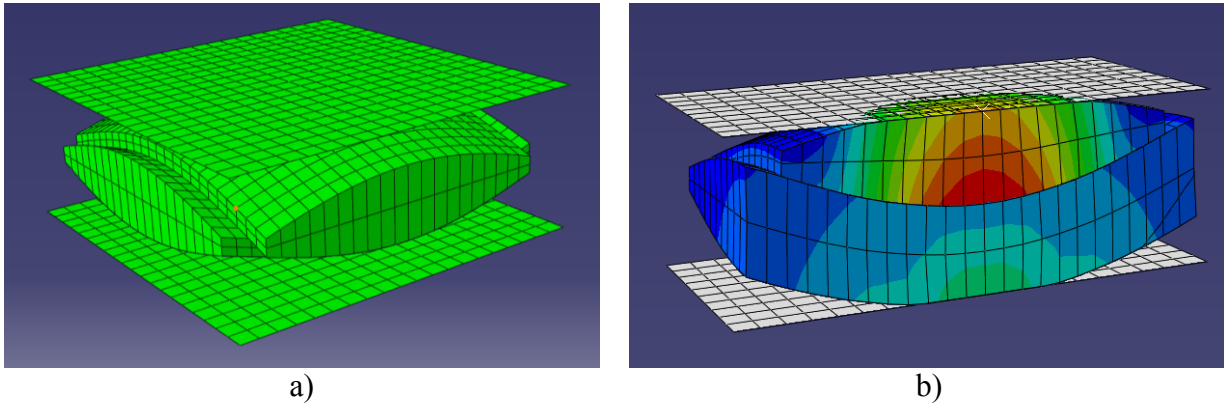


Figure 5-9: a) Compression model of the crossover in Abaqus b) Graphical results for the strains during the compression test

We extracted the contact force F_c between the yarns at the middle of the crossover and we also extracted the mean relative compression height d_c of the yarns. The transverse compression of the yarns is described in our user material subroutine model by the following function provided in the works of Grujicic et al. (32):

$$F_c = \frac{b d_c}{a - d_c} \quad (5.8)$$

Therefore, we need to obtain the values of parameters a and b from our 3D model to be able to use this equation in the VUMAT subroutine. When the two values are extracted from the FEA as described before and plotted against each other we obtain the following numerical experimental curve displayed in blue in Figure 5-10.

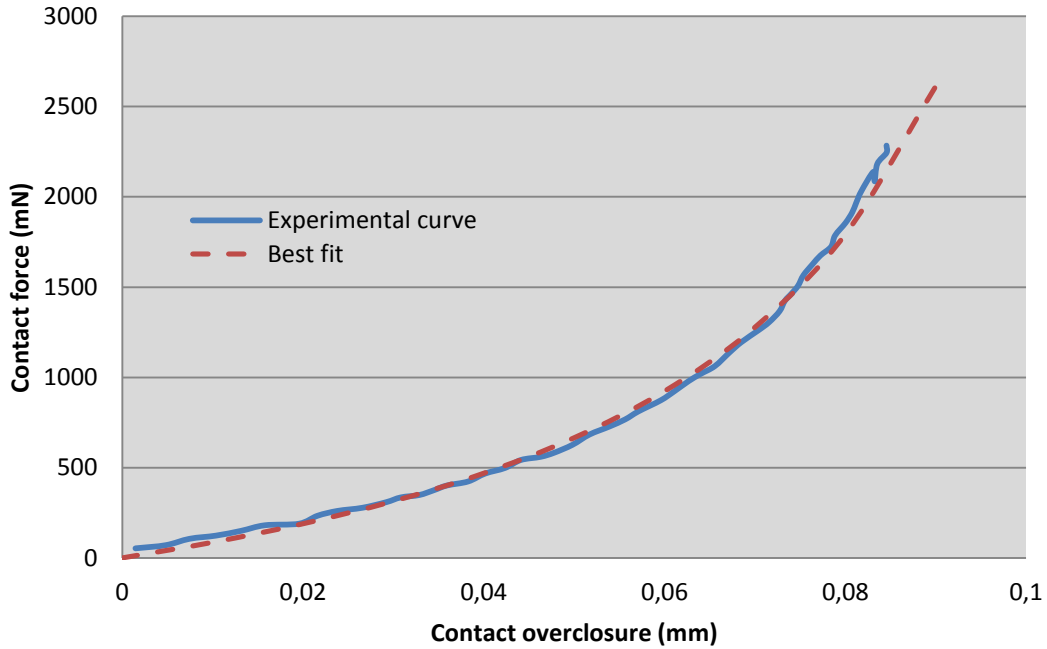


Figure 5-10: Transverse compaction characterization of the 3D crossover

Using the Maple program presented in Appendix A, we were able to obtain the following values for parameters a and b. Parameter a has a value of 0.12389 mm and parameter b is 984.32 mN. Plotting the theoretical red curve in Figure 5-10 based on the analytical function given by Grujicic against the experimental curve obtained from the FEA extractions, we can see that there is a very good correlation between them.

5.3.3 Shear behavior of the unit cell

Shear behavior of the model has been tested but could not return any useful results. This is due to a number of unanswered questions about the analysis setup in the literature. We based the modeling of this test on the works of Grujicic et al. (1) and compared our results to the ones he obtained. We pinpointed the following three problems concerning the definition of the analysis that may cause our results to be different from his results.

Firstly, since our model is geometrically different from the one used in Grujicic's works (1), the contact area is also different which obviously leads to a discrepancy between the two results. Indeed, the shear modulus is extremely dependent on the contact surface. Moreover, as the

analysis progress, the contact surface between the yarns is also changing and this is a phenomenon that is difficult to quantify.

Secondly, we do not know the maximum angle of rotation that has been used in Grujicic's analysis. The shear behavior is indeed a complex phenomenon to quantify and to reproduce in finite element analysis. Because the fiber is rotating in plane around the crossover point, then if the rotation continues, we may have the problem that the two yarns will ultimately tend to become parallel and jam with each other. In that situation the yarns will require a large force to further displace them. In the 3D model created for this work we manually adjusted the boundary condition forcing the rotation of the yarns to limit their rotation up to the point where the yarns started to jam against each other.

Finally, the shear modulus also depends on the transverse compaction of the yarns at the crossover point as will be seen in chapter 6. In our model, we made the assumption that the yarns had to stay in contact at the crossover point.

Because of these uncertainties, we could not produce a valid simulation without making abusive assumptions about our model. In consequence, the shear modulus law given in Shahkarami et al. (31) was taken. It is presented in greater details in chapter 6.

5.4 Conclusions

The 3D unit-cell model of the RUC proves to be very powerful in predicting the behavior of one crossover in simple loading cases. We tested it for simple loading and obtained results regarding material properties (Young modulus) to calibrate the VUMAT subroutine. This is due to the wealth of geometry and material details it is able to take into account. But because it is aimed to be used at a very small scale, it is quite inefficient for representing large engineering systems. It is thus used to calibrate the VUMAT subroutine that will be used in conjunction with a shell element as it is discussed in the next chapter.

CHAPTER 6 - DEVELOPMENT OF THE FABRIC UNIT-CELL CROSS-OVER MATERIAL MODEL SUBROUTINE

This chapter is concerned with the development of a constitutive material model for a smeared (equivalent) shell element that capture the biaxial response of the fabric unit-cell and that performs similarly as the 3D yarn crossover model of the previous chapter. The shell element takes advantage of a meso-mechanical model of the fabric crossover and can be classified as being between the simple pin-jointed cable model and the detailed 3D fabric crossover model of the fabric unit-cell both in terms of complexity and efficiency. The developed shell element based crossover model will thus be able to capture many details of the weave and yarns that the pin-jointed bar model would overlook, while it is significantly more efficient numerically compared to the 3D fabric crossover model. This chapter thus discusses the details of the User Material Model (VUMAT) development to provide the constitutive relationship for the smeared shell element that represents a fabric unit-cell. While developing the VUMAT for the shell element, several simplifying assumptions have been made based on the physical behavior of a fabric. In particular since fabrics generally have very low bending and shear stiffness, it is

assumed that their out-of-plane stiffness is negligible compared to their in-plane stiffness. The in-plane extensional and shear responses of the fabric are assumed decoupled and treated separately based on the mathematical models developed in the preceding sections. A meso-mechanical model of fabric crossover is thus developed and implemented as a constitutive material model for an efficient shell element in ABAQUS-Explicit to capture the biaxial response of a fabric unit-cell.

6.1 VUMAT subroutine description

As Abaqus/Explicit help file on this subject is very extensive; we will only present here an overview of what this Abaqus/Explicit tool enables one to do. We will outline the principal built-in variables we had to use in the process of developing the user material subroutine. Also, some technical insights from the knowledge we gained working with this routine will be given. Further details on how the routine was designed and how our mathematical model was integrated to fit the routine's framework are discussed in chapter 6.

6.1.1 Generalities on the subroutine

A VUMAT user subroutine is used to define the mechanical constitutive behavior of the material that would be used in a dynamic analysis in Abaqus/Explicit module. It provides the framework and the methodology to create a material model that is not already present in Abaqus/Explicit material model library. Simply put, the VUMAT consists of a Fortran sub-program that is called by the finite element software for blocks of material calculation points for which the material is defined in the user subroutine. The subroutine can roughly be divided into five main parts:

- **Complete variable definition.** This concerns the declaration and description of all the variables to set up the framework of the subroutine. Also we find a description of all the state variables that we use to do the necessary calculations. Finally all the material parameters are defined to fit the subroutine's nomenclature. Material parameters are described to help the user find his way inside the program and finally each one is affected a value that is read from Abaqus/Explicit.

- **Computations for initialization.** It is a small part of the program used by Abaqus/Explicit mainly to check on the constitutive relation and then calculate the equivalent material properties. This is done to ultimately compute the initial elastic wave speed in the material.
- **Reading the variables that are passed in by Abaqus/Explicit.** At this point we need to read and store all the necessary information from Abaqus/Explicit input file that will be fed into the mathematical model to calculate the new state of the material. Since fabric model must be used in nonlinear geometric context, in our case we need to use the right stretch tensor $[U]$ and the deformation gradient from the previous step $[F]$ as well as some user defined state variables as it is explained in details in chapter 6.
- **Computing the new material state.** This is the core of the routine because it is mainly constituted of the mathematical equations of our model. It also includes a local Newton-Raphson solution scheme.
- **Transform and return the results to Abaqus/Explicit.** After the update of material state we have to translate the results we obtain from the model into the Green-Naghdi frame used by Abaqus/Explicit to read the updated stress.

At this point it is interesting to note that for debugging purposes we coded inside the program a number of operations to verify the validity of the results given by some key computations. All the output results at various steps of the computation are stored in a text file allowing the user to follow almost step by step the intermediate results given by the model.

6.1.2 Material point deletion

This is a very important feature available in VUMAT that we used to delete the damaged shell elements from the analysis. Indeed, material points that satisfy a user-defined failure criterion can be removed permanently. We had to define a specific state variable (state variable 30 in our case) controlling the element deletion flag. The deletion state variable should be set to a value of one or zero. A value of one indicates that the material point is active while a value of zero indicates that Abaqus/Explicit should delete the material point from the model and set the stresses in the element to zero. The structure of the block of material points passed to user

subroutine VUMAT remains unchanged during the analysis and deleted material points are not removed from the block. Abaqus/Explicit will pass zero stresses and strain increments for all deleted material points. Once a material point has been flagged as deleted, it cannot be reactivated.

As we discussed before, most fabrics exhibit a periodic geometry of yarn interlacings, thus making them good candidates for unit-cell analysis approach. Many researchers like Kawabata et al. (21), King et al. (23), Ivanov and Tabiei (22) have tried to incorporate the mechanical response of fabrics in efficient membrane or shell elements. The material model for the smeared shell elements that has been developed, assume for simplicity a balanced plain weave architecture and hence the crossover point as having two principal directions, naturally taken into account in the model development. Generally these elements are a continuum representation of the fabric into a two dimensional homogeneous material.

Pin-jointed bar models usually consider that the warp and fill responses are decoupled but continuum, unit-cell based membrane/shell elements can reproduce the biaxial behavior of the fabrics if the proper constitutive model is implemented. The actual implementation is performed in Abaqus/Explicit through its VUMAT facilities provided by the software. The goal here is to present a simple model capable of capturing the biaxial and uniaxial behavior of symmetrically loaded yarn crossovers, as well as their shearing response. Considering a linear representation of the yarn centerlines, the equilibrium of the crossing yarns under uniaxial or biaxial extension is achieved by balancing the tensile forces taking place in the yarns with due account of the contact forces developed between the yarns. In fact, using the contact force between the yarns, it is possible to determine the position of the contact point along the transverse z axis. Then, using the position of the 2 deformable yarns contact point and the yarns extensions, one can determine the tensile force induced in each yarn. The model is thus based on tracking the location of the contact point between the yarns. It is aimed at capturing the interactions of warp and fill yarns to determine their in-plane extensional response. The details of the computations involved in the VUMAT are presented in this chapter.

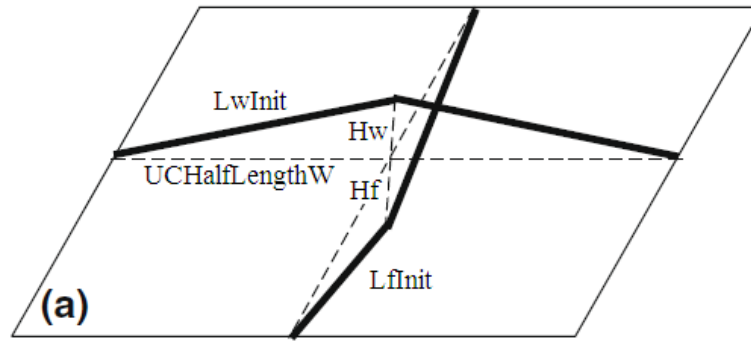


Figure 6-1: Trellis mechanism in initial undeformed configuration

Figure 6-1 shows the basic trellis mechanism in the undeformed configuration that is used to model the behavior of the crossover as described in the works of Grujicic (1) which is the starting point of the VUMAT. The deformed configuration of this structure is shown in Figure 6-2.

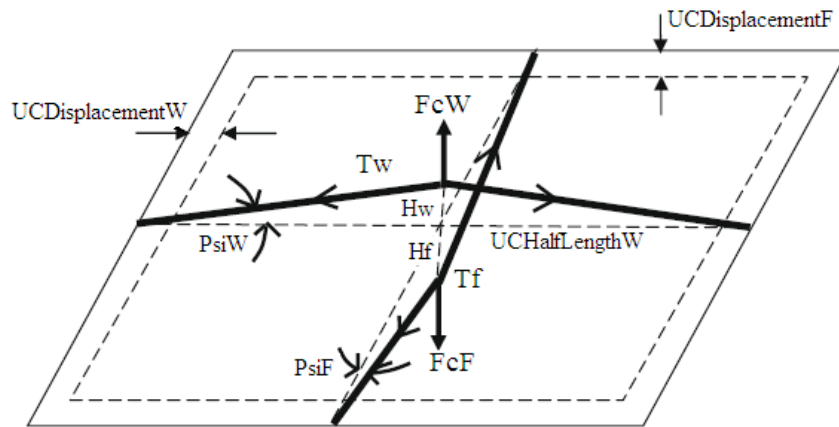


Figure 6-2: Trellis mechanism in deformed configuration

The principle is quite simple, when the yarn cross-over model is subjected to biaxial extension for example, it gets elongated in its two principal directions corresponding to the two yarn directions and contact forces appear at the crossover point. The contact forces are called F_{cW} for warp yarns and F_{cF} for fill yarns and the height of the yarns centerline H_W and H_F decreases because of the transverse compaction. Also, during compaction, the angles Ψ_{iF} and Ψ_{iW} decrease. Once the yarns are fully compacted and the shell element gets elongated again then the beam elements representing the behavior of the yarns are subjected to tensions T_F and T_W appearing in each yarn. Using a basic beam formula we can relate the extension of the beam and

the tension developing inside it as it is explained in later. In order to facilitate the understanding of the computational process used, the reader is referred to Figure 6-3 extracted from Shahkarami (2) that illustrates the geometry of the yarn crossover before and after deformation by symmetrically applied displacements along the two crossing yarn directions.

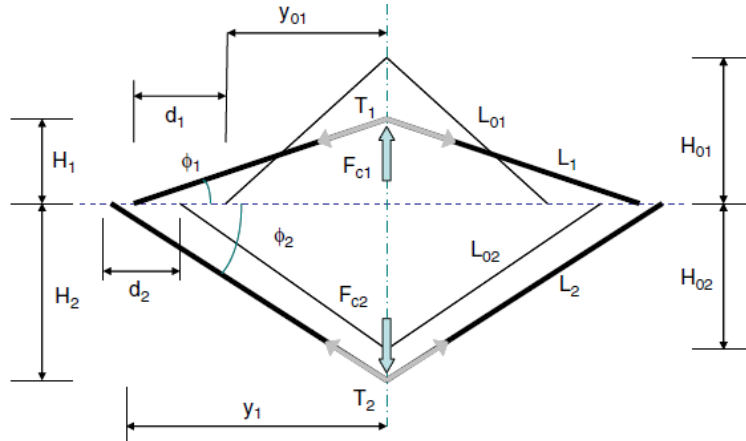


Figure 6-3: Geometry of the yarn crossover before and after deformation by symmetrically applied displacements along the two crossing yarn directions. Both yarns are shown on the same plane (1)

6.2 User subroutine computations

6.2.1 Using the VUMAT in Abaqus

Interfacing Abaqus main engine with the user material subroutine is quite easy since the software gives the framework needed to define the material. At each time step Abaqus passes to the user subroutine the element strain increments evaluated at the shell element integration point in a local Green-Naghdi coordinate system. It is thus required to compute the updated Cauchy stresses in the local material frame (yarn direction) inside the VUMAT, express the results in the element Green-Naghdi frame and return them to Abaqus for continuation of the analysis.

The main goal here is to develop an efficient shell element whose behavior can be compared to that of a yarn crossover. This shell element takes advantage of a meso-mechanical pin jointed cable model of the fabric crossover and is able to capture the compression of the yarns at the crossover point.

This section provides all the information about the development of the user material model providing the mathematical framework to be used in the routine. In setting up the VUMAT, the

main objective is to use the strain increments that are passed into the subroutine to calculate at each time step the extension and rotation of the warp and weft yarns that are required for computing the stresses based on the tensile and shear behavioral equations.

6.2.2 Short description of the VUMAT's built-in variables

This paragraph explains to the reader the meaning of the main variables imposed by the subroutine framework. Doing so it will be much easier to understand the program presented in appendix B.

A user subroutine VUMAT is used to define the mechanical constitutive behavior of the material that would be used in a dynamic analysis in Abaqus/Explicit module. It provides the framework and the methodology to create a material model that is not already present in Abaqus/Explicit material model library. Simply put, the VUMAT consists of a Fortran sub-program that is called by the finite element software for blocks of material calculation points for which the material is defined in the user subroutine. Our subroutine can roughly be divided into five main parts:

- **Complete variable definition.** This concerns the declaration and description of all the variables to set up the framework of the subroutine. Variables are classified into either input variables, known at the beginning of the time step and output variables that are updated by the subroutine and returned to Abaqus at the end of the time step. All the material parameters are defined to fit the subroutine's nomenclature and are input variables (each one is affected a value that is read from Abaqus/Explicit), together with state variables available at old time and either computed or updated at current time step that we use to do the necessary calculations. Material parameters are described to help the user find his way inside the program; material parameters or user defined state variables (such as Green-Naghdi frame or fiber orientation vectors) that evolve with the material deformation must be updated.
- **Computations for initialization.** It is a small part of the program used by Abaqus/Explicit mainly to check on the constitutive relation and then calculate the

equivalent material properties. This is done to ultimately compute the initial elastic wave speed in the material.

- **Reading the variables that are passed in by Abaqus/Explicit.** At this point we need to read and store all the initial material properties from Abaqus/Explicit input file, information that will be fed into the mathematical model which computes the new state of the material. In addition to the material properties ABAQUS provides kinematics information at the beginning and at the end of the time step which include the deformation gradient from the previous step and current step [F], the right stretch tensor [U] from previous and current time step as well as the strain increment. User defined state variables are also available at the beginning of the increment and must be updated as it is explained later.
- **Computing the new material state.** This is the core of our routine because it is mainly constituted of the mathematical equations of the model. If non-linear equations are required to update the state variables, a local Newton-Raphson solution scheme can be used.

The complete list of all variables is given in the VUMAT help file but here we selected the most important ones:

- **stressNew.** This is the stress tensor at each material point at the end of the increment. This is a variable that has to be defined in order for the subroutine to return information to Abaqus/Explicit after the computations of the model are done. As we said earlier, the Cauchy stresses must be given in the Green-Naghdi frame for Abaqus/Explicit to interpret them correctly.
- **stateNew.** It refers to all user defined state variables that are updated during the computations of the model and returned to Abaqus/Explicit. By default we decided to output all of them so Abaqus/Explicit can store them in the result file along with the updated stresses. This allowed us to thoroughly check all the detailed results.

- **stateOld.** As the variable before, it refers to the state variables computed and returned to Abaqus/Explicit during the previous time increment. They are passed into the subroutine for further updating.
- **stepTime.** This is the value of time since the beginning of the step. We did not modify or use this variable in any way since it is controlled directly by Abaqus/Explicit.
- **totalTime.** This is the value of the total time since the beginning of the analysis. The time at the beginning of the step is given by the totalTime value minus the stepTime value. We had to read and test this value; if it is equal to zero then the subroutine is using the initialization part of the program. If it is different from zero than the material model part of the program is used to update the stresses etc.
- **props.** All the user-defined material properties input in Abaqus/Explicit guest user interface are read and stored in this array.
- **strainInc.** This is the continuum strain increment tensor at each material point that has to be used by the model to update stress based on the geometrical state of the crossover.
- **stretchOld.** It corresponds to the stretch tensor [U] at each material point at the beginning of the increment defined from the polar decomposition of the deformation gradient:

$$F = R \cdot U \quad (6.1)$$

- **stretchNew.** It corresponds to the stretch tensor [U] at each material point at the end of the increment. This variable does not have to be updated by the user.
- **defgradOld.** This is the deformation gradient tensor at each material point at the beginning of the increment which is used to assemble tensor [F].
- **defgradNew.** This is the deformation gradient tensor at each material point at the end of the increment. This variable does not have to be updated by the user.

6.2.3 Initial rigidity matrix

In order for Abaqus to initialize the computations we need to provide it with an initial stiffness matrix. From this matrix it will automatically calculate a stable time step for the dynamic analysis which is a crucial parameter for the explicit analysis to run properly. This computation of the stiffness matrix is performed when the condition of a total analysis time is zero (totalTime=0) meaning that this operation should be performed as the first calculation of the analysis. Otherwise the time increment will not be computed and the analysis will return an error.

The form of this matrix is a well-known result from continuum mechanics if we assume an initial orthotropic material and is thus computed as:

$$[C] = \begin{bmatrix} \frac{E_w}{1 - \nu_{12}^2} & \frac{E_f \nu_{12}}{1 - \nu_{12}^2} & 0 \\ \frac{E_f \nu_{12}}{1 - \nu_{12}^2} & \frac{E_f}{1 - \nu_{12}^2} & 0 \\ 0 & 0 & G \end{bmatrix} \quad (6.2)$$

Where parameters E_w, E_f, ν_{12}, G are passed into the VUMAT as material parameters and therefore they can readily be used to define the matrix.

6.2.4 VUMAT computation steps

The knowledge of the unit-cell stretches in the two main in-plane directions along the yarns and the knowledge of the angle between these directions is essential for the determination of the forces developed in the crossover. In order to follow the extension and rotation of the yarns, two vectors are attached to virtual yarns at the initiation of the analysis. This initial configuration is constantly updated through the analysis using the deformation gradient provided by Abaqus at the beginning of each time step. Indeed the two yarn directions do not remain orthogonal after deformation. This has been presented in detail in Chapter 4.

The updating process of the material direction vectors, which is performed by VUMAT prior to the computations of the yarns extensions and shear behavior, will be discussed in further details

in the following sections. The steps involved in this process are given below and they are performed at each time increment.

Step-1: read and store the stretch tensor $[U]$ and the deformation gradient tensor $[F]$ provided by Abaqus:

$$\begin{array}{ll} U(1,1) = \text{stretchOld}(k,1) & F(1,1) = \text{defgradOld}(k,1) \\ U(2,2) = \text{stretchOld}(k,2) & F(2,2) = \text{defgradOld}(k,2) \\ U(1,2) = \text{stretchOld}(k,4) & F(1,2) = \text{defgradOld}(k,4) \\ U(2,1) = \text{stretchOld}(k,4) & F(2,1) = \text{defgradOld}(k,4) \end{array}$$

If this is the first increment performed then initializes the warp and fill yarn vectors initial coordinates as:

$$\begin{array}{ll} fW_x\text{Init} = \text{one} & e1_x\text{Init} = \text{one} \\ fW_y\text{Init} = \text{zero} & e1_y\text{Init} = \text{zero} \\ fF_x\text{Init} = \text{zero} & e2_x\text{Init} = \text{zero} \\ fF_y\text{Init} = \text{one} & e2_y\text{Init} = \text{one} \end{array}$$

If this is not the first increment performed then read the previous vector orientation for the warp and fill yarns as well as for the Green-Naghdi frame that have been stored at the end of the previous increment.

$$\begin{array}{ll} fW_x\text{Old} = \text{stateOld}(k,1) & e1_x\text{Old} = \text{stateOld}(k,5) \\ fW_y\text{Old} = \text{stateOld}(k,2) & e1_y\text{Old} = \text{stateOld}(k,6) \\ fF_x\text{Old} = \text{stateOld}(k,3) & e2_x\text{Old} = \text{stateOld}(k,7) \\ fF_y\text{Old} = \text{stateOld}(k,4) & e2_y\text{Old} = \text{stateOld}(k,8) \end{array}$$

Also one has to read in the damage status of each yarn and the yarn total extension. These informations have been stored at the end of the previous time step in state variables.

AllongTotWOld = stateOld(k,16)

fail_flagW = stateOld(k,19)

AllongTotFOld = stateOld(k,17)

fail_flagF = stateOld(k,20)

Step-2: compute the inverse of the right stretch tensor $[U]^{-1}$. This is a simple operation that we will not develop here.

Step-3: compute the rotation matrix $[R]$ from the knowledge of the deformation gradient tensor and the inverse of the right stretch tensor just calculated.

$$[R] = [F] \cdot [U]^{-1} \quad (6.3)$$

Step-4: compute the new Green-Naghdi frame (e_1, e_2) from the initial frame at the beginning of the analysis and the rotation tensor just calculated :

$$\{e\}_{new} = [R] \cdot \{e\}_{old} \quad (6.4)$$

Step-5: compute the new yarn frame. The deformation gradient enables us to update the material frame (f_W, f_F) throughout the analysis at each time step; it is used to obtain updated material orientation vectors as:

$$\begin{aligned} \{f_W\}_{new} &= \frac{\mathbf{F} \cdot f_{W_{init}}}{\|\mathbf{F} \cdot f_{W_{init}}\|} \\ \{f_F\}_{new} &= \frac{\mathbf{F} \cdot f_{F_{init}}}{\|\mathbf{F} \cdot f_{F_{init}}\|} \end{aligned} \quad (6.5)$$

Step-6: compute the angles θ_1, θ_2 between the updated yarn orientation vectors and the updated Green-Naghdi frame unit vectors.

$$\begin{aligned} \cos \theta_1 &= \frac{\|e_1 \cdot f_W\|}{\|e_1\| \cdot \|f_W\|} \\ \sin \theta_1 &= \frac{\|e_1 \times f_W\|}{\|e_1\| \cdot \|f_W\|} \\ \cos \theta_2 &= \frac{\|e_2 \cdot f_F\|}{\|e_2\| \cdot \|f_F\|} \\ \sin \theta_2 &= \frac{\|e_2 \times f_F\|}{\|e_2\| \cdot \|f_F\|} \end{aligned} \quad (6.6)$$

Step-7: compute the shear angle between the updated warp and fill yarns orientation vectors. Also the initial shear angle from the initial vectors is computed by the routine to verify that it gave us a result of 90 degrees initially.

$$\cos \theta_{init} = \frac{\|f_{W_{init}} \cdot f_{F_{init}}\|}{\|f_{W_{init}}\| \cdot \|f_{F_{init}}\|} \quad (6.7)$$

$$\cos \theta_{new} = \frac{\|f_{W_{new}} \cdot f_{F_{new}}\|}{\|f_{W_{new}}\| \cdot \|f_{F_{new}}\|}$$

Step-8: compute the transformation matrix used to transform the results from the Green-Naghdi frame to the material frame using transformation matrices $[T_1]$ and $[T_2]$.

$$\begin{aligned} [T_1] &= \begin{bmatrix} \cos \theta_1 & -\sin \theta_1 \\ \sin \theta_1 & \cos \theta_1 \end{bmatrix} \\ [T_2] &= \begin{bmatrix} \cos \theta_2 & -\sin \theta_2 \\ \sin \theta_2 & \cos \theta_2 \end{bmatrix} \end{aligned} \quad (6.8)$$

Also, compute the associated transposed matrix of $[T_1]$ and $[T_2]$.

$$\begin{aligned} [TT_1] &= \begin{bmatrix} \cos \theta_1 & \sin \theta_1 \\ -\sin \theta_1 & \cos \theta_1 \end{bmatrix} \\ [TT_2] &= \begin{bmatrix} \cos \theta_2 & \sin \theta_2 \\ -\sin \theta_2 & \cos \theta_2 \end{bmatrix} \end{aligned} \quad (6.9)$$

Remark: if the fiber frame (denoted (x', y') in Figure 6-4) is used instead of Naghdi frame, one must compute the local cartesian fiber frame which is obtained by computing the fiber directions using gradient tensor F as such:

$$\begin{aligned} \{f_W\}_{new} &= \frac{F \cdot f_{W_{init}}}{\|F \cdot f_{W_{init}}\|} \\ \{f_F\}_{new} &= \frac{F \cdot f_{F_{init}}}{\|F \cdot f_{F_{init}}\|} \end{aligned} \quad (6.10)$$

Because the newly computed vectors are not orthogonal after deformation the shear stress does not respect the symmetry conditions. We thus have four in-plane stress and strain components related to local cartesian frame (x', y') as is shown in Figure 6-4.

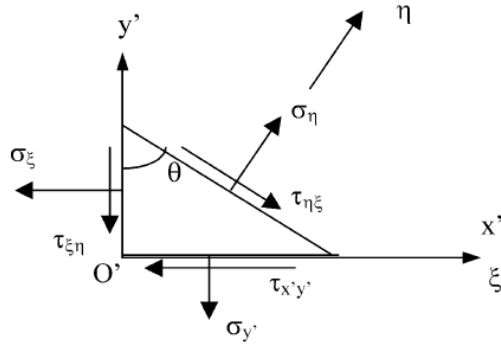


Figure 6-4: Stress and strain components in fiber frame

These stress and strain in-plane components can be expressed in the fiber frame using T_2 and T_3 transformations as such:

$$\begin{bmatrix} \sigma_{x'} \\ \sigma_{y'} \\ \tau_{x'y'} \end{bmatrix} = [T_2] \begin{bmatrix} \sigma_{\xi} \\ \sigma_{\eta} \\ \tau_{\xi\eta} \\ \tau_{\eta\xi} \end{bmatrix} \quad (6.11)$$

$$\begin{bmatrix} \epsilon_{\xi} \\ \epsilon_{\eta} \\ \gamma_{\xi\eta} \\ \gamma_{\eta\xi} \end{bmatrix} = [T_3] \begin{bmatrix} \epsilon_{x'} \\ \epsilon_{y'} \\ \gamma_{x'y'} \end{bmatrix}$$

where T_2 and T_3 are defined in term of angle theta between the fiber material frame f1 and f2 as:

$$[T_2] = \begin{bmatrix} 1 & 0 & 0 & 0 \\ 0 & 1 & -\cot \theta & -\cot \theta \\ -\cot \theta & \cot \theta & 0 & 1 \end{bmatrix} \quad (6.12)$$

$$[T_3] = \begin{bmatrix} 1 & 0 & 0 \\ \cos^2 \theta & \sin^2 \theta & \sin \theta \cos \theta \\ 0 & 0 & 1 \\ 0 & 0 & 1 \end{bmatrix}$$

The evolution of the reference frames are presented in the Figure 6-5.

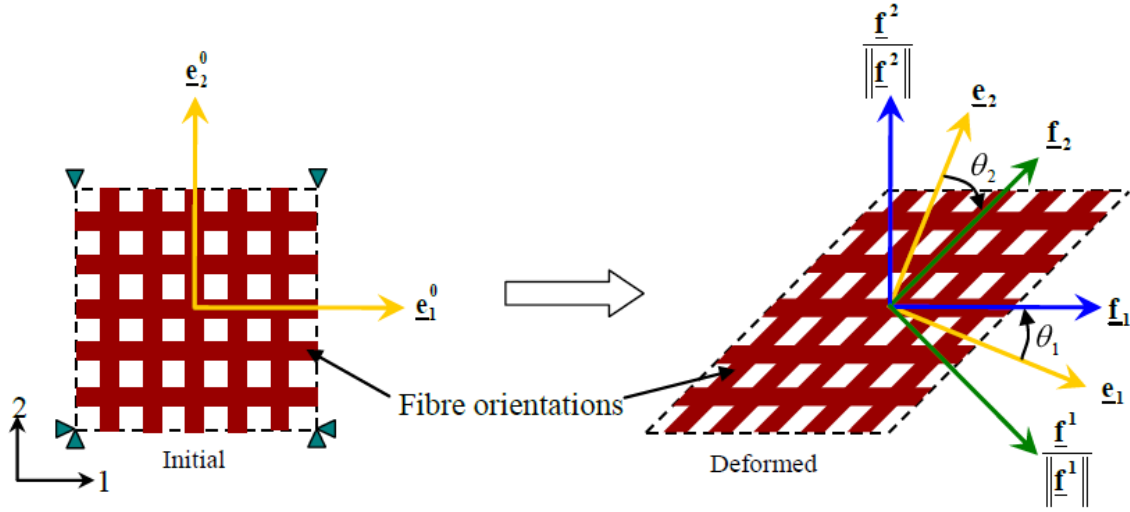


Figure 6-5: Evolution of the Green-Naghdi and material frames during the deformation's evolution

The frame (e_1, e_2) is the Green-Naghdi frame and (f_1, f_2) , also noted (f_W, f_F) is the material frame that moves with the virtual yarns. As we can see in Figure 6-5, in the initial position the material frame is the same as the Green-Naghdi frame, but at the deformation progresses this is no longer true that's why we need to track each vector during the analysis and use transformation matrix to transpose relevant variables from one frame to another as we will be doing in the following procedure.

Step-9: Perform a transfer from macroscale strain to mesoscale level by computing the strain increment in the yarns directions. Knowing the transformation matrix from the local material frame to the local updated Green-Naghdi frame, we can transform the strain increments (strainInc) given by Abaqus in the Green-Naghdi frame to the material frame. This will generate a strain increment tensor for each yarn family (StrainIncW, StrainIncF) using the transformation matrix as follows:

$$\begin{aligned} [StrainIncW]_{mat} &= [TT_1][StrainInc]_{GN} [T_1] \\ [StrainIncF]_{mat} &= [TT_2][StrainInc]_{GN} [T_2] \end{aligned} \quad (6.13)$$

In the previous equation, the Green-Naghdi strain increment tensor denoted $[StrainInc]_{GN}$ is given by Abaqus at the beginning of the increment.

Step-10: calculate the incremental stretch ratio along each yarn. The displacements along the two yarn directions are calculated using the well-known results of continuum mechanics. The stretch increment in the direction of a vector from time step n-1 to n is determined as follow:

$$StretchIncrement_i^n = \sqrt{1 + 2\Delta\varepsilon_{i11}^n} \quad (6.14)$$

Step-11: calculate the total stretch ratio for each yarn. The total stretch in material direction Λ_i^n is updated at each time step using the incremental values of stretch $StretchIncrement_i^n$ as shown below:

$$AllongTot_i^n = AllongTot_i^{n-1} StretchIncrement_i^n \quad (6.15)$$

Step-12: calculate the unit cell displacement along each yarn. Using the total stretch and the length of the unit cell $UCHalfLength_{i_{init}}$, we may calculate the displacement $UCDisplacement_i^n$ along each yarn family as follows:

$$UCDisplacement_i^n = (AllongTot_i^n - 1) UCHalfLength_{i_{init}} \quad (6.16)$$

From the knowledge of the displacements, we may now calculate the tensile forces developed inside the yarns. Also, from the knowledge of the shear angle, we may calculate the shear modulus and then the shear stress as will be discussed further later.

Step-13: calculate the unit-cell half length from the displacement of the unit-cell and the initial half length of one yarn

$$UCHalfLength_i = UCDisplacement_i^n + UCHalfLength_{i_{init}} \quad (6.17)$$

Step-14: calculate the initial half length of the yarns from the knowledge of the unit-cell half length and the height of the yarn centerline as:

$$L_{i_{init}} = \sqrt{UCHalfLength_{i_{init}}^2 + H_{i_{init}}^2} \quad (6.18)$$

Step-15: check if any of the two yarns has previously failed. If that is the case, set the tension in the yarn to zero.

Figure 6-6 illustrates the schematic model of a yarn in the fabric in contact with the crossing yarn and the corresponding free body diagram showing the forces acting on it as it is presented in Shahkarami's works (4).

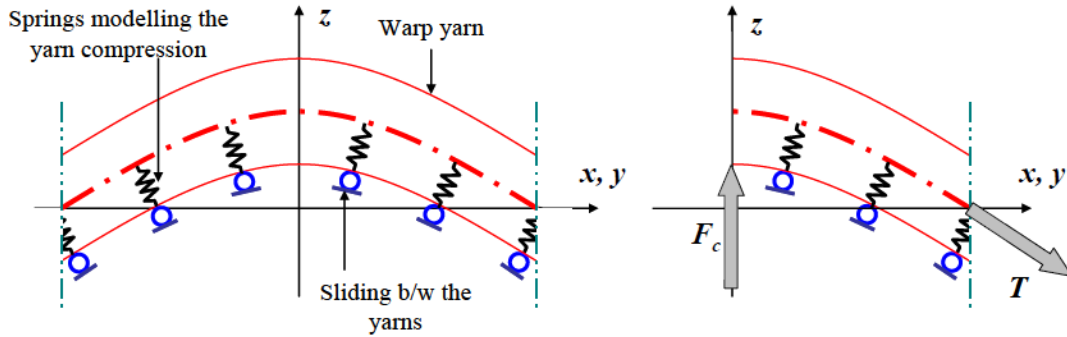


Figure 6-6: A yarn in the fabric (left) in contact with the crossing yarn with a free body diagram showing the forces acting on it (right)

Step-16: Start the Newton-Raphson iterations to obtain the yarns' centerline heights H_W and H_F .

6.2.5 Newton-Raphson iterations

The Newton-Raphson iterations are required to determine H_W and H_F and in order to do so we have to initialize the routine by doing some preliminary computations. The purpose here is not to give the detail of the routine's functioning; the theory is covered in Appendix B thus we will only show the computations performed in the routine and it's the basic parameterization.

At this point it is important to note that the calculations presented in step 17 through step 25 are computed at each iteration of the Newton-Raphson routine. The first iteration uses the initial yarns centerline heights denoted $H_{i_{init}}$. To accentuate that fact we will denote that parameter $H_{i_{iter}}$.

Step-17: The first task is to calculate the current yarn length from the knowledge of the current unit-cell half-length and the current height of yarn centerline. This is done by computing the extension of the yarn represented by beams.

$$L_i = \sqrt{UCHalfLength_i^2 + H_{i_{iter}}^2} \quad (6.19)$$

Step-18: calculate the contact forces. It is important to note at this point that tensile forces developed inside the yarns due to the in-plane deformation are a function of the yarn material and geometrical properties of the yarns. Bending and shear mechanical properties of the yarns are considered negligible compared to the axial tensile stiffness and thus they are not considered in this study. The tensile behavior of the yarns is assumed to follow the linear elastic model defined by the equation below:

$$T_i = E_i A_i \frac{L_i - L_{i_{init}}}{L_{i_{init}}} \quad (6.20)$$

Where A_i is the cross-sectional area of the yarns and $L_{i_{init}}$ and L_i are the initial and current length of the yarns. E_i is the Young modulus of the yarns.

Step-19: compute the angles formed by the warp and fill yarns at the corner of the unit cell which are called the yarn end slope Psi_W and Psi_F . They are shown on figure 6.2.

$$\sin Psi_i = \frac{H_{i_{iter}}}{\sqrt{UCHalfLength_i^2 + H_{i_{iter}}^2}} \quad (6.21)$$

Step-20: compute the contact forces between the yarns which are calculated as such:

$$F_{c_i} = 2 T_i \sin Psi_i \quad (6.22)$$

Step-21: calculate the transverse yarn compression. When the two yarn support loads and are not broken and in contact, the distance between the two summit points is smaller than the initial distance, and contact force is developed between the two yarns. The extent of this force depends on the yarn contact over-closure given by:

$$d_{c1} + d_{c2} = d_c \quad (6.23)$$

This is actually the yarn overclosure at the contact point and it appears only when the contact force between the yarns is positive. In the case of an existing contact force between the yarns,

the yarn overclosure, the relationship between the transverse contact force and the yarn overclosure is given in the works of Grujicic et al. (32) :

$$F_c = \frac{b d_c}{a - d_c} \quad (6.24)$$

The two parameters a and b have been determined using the 3D crossover compression numerical experiment.

Step-22: in order to calculate the yarn heights we have introduced, following the works of Shakharami et al (4), an equilibrium function f_1 which has to be satisfied in conjunction with the geometric compatibility function f_2 . These two functions are given by:

$$\begin{cases} f_1 = Fc_W - Fc_F \\ f_2 = H_{W_{iter}} + H_{F_{iter}} - H_{W_{init}} - H_{F_{init}} + dc_W + dc_F \end{cases} \quad (6.25)$$

The Newton-Raphson technique is used to estimate the unknowns by an iterating process over $H_{W_{iter}}$ and $H_{F_{iter}}$ from their initial values $H_{W_{init}}$ and $H_{F_{init}}$ using a system of two non-linear equations constituted by function f_1 and f_2 . The Newton-Raphson iterative scheme used in this VUMAT is presented in detail in appendix B.

It is quite easy to define the iterative scheme of the Newton-Raphson algorithm. We have to calculate the Jacobian matrix from the partial derivatives of equations developed earlier and give an initial guess of the two values close to the values we are looking for, in our case we gave $H_{W_{init}}$ and $H_{F_{init}}$.

$$J = \begin{bmatrix} \frac{\partial f_1}{\partial H_W} & \frac{\partial f_1}{\partial H_F} \\ \frac{\partial f_2}{\partial H_W} & \frac{\partial f_2}{\partial H_F} \end{bmatrix} \quad (6.26)$$

The explicit form of function f_1 and f_2 are given in Appendix C.

Step-23: compute the tolerances. We instructed the routine to do a maximum of 50 iterations until the tolerance values for the contact forces (tol_1) and height of centerline (tol_2) are reached. The tolerances were defined as follows:

$$\begin{aligned}
 tol_1 &= 1.10^{-5}|Fc_W - Fc_F| \\
 tol_2 &= 1.10^{-5}
 \end{aligned}
 \tag{6.27}$$

These tolerances are chosen arbitrarily and depend on the level of precision we want to obtain. We observed that a tolerance of 1.10^{-5} is enough to obtain very good results.

Step-24: Check for convergence of the iteration scheme. Thus, if the values of functions f_1 and f_2 are below the tolerance, the iterations stops and return the last values of H_W and H_F which are considered valid and thus used in the next steps.

Step-25: Return the two values H_W and H_F to the main program.

6.2.6 Tensile response

The tensile response of the yarn is concerned with the in-plane extension of the beam representing the yarns. Also we will describe here the failure criterion that has been used in the subroutine to assess if the yarns are broken or not. The element erosion is also an important aspect taking place when the two yarns have failed. The matrix defining the fabric stress from the knowledge of the tension taking place inside the yarn will also be presented here.

Step-26: Recalculate the tensions T_W and T_F . From the modified heights H_W and H_F of the centerlines of the yarns we may recalculate the half-length of the fibers and obtain the true tensile force inside the yarns.

$$\begin{aligned}
 L_i &= \sqrt{UCHalfLength_i^2 + H_i^2} \\
 T_i &= E_i A_i \frac{L_i - L_{i_{init}}}{L_{i_{init}}}
 \end{aligned}
 \tag{6.28}$$

Step-27: Check for yarn failure. At each time increment and for each shell element, the program will compare the tension calculated in the yarns with the (ultimate) tension limit given by the yarn manufacturer. This is obviously done for both yarns as follows:

$$\begin{cases} \text{If } T_i < Tu_i \text{ then yarn is intact} \\ \text{If } T_i > Tu_i \text{ then yarn is broken} \end{cases} \quad (6.29)$$

We have defined within the subroutine a failure flag for each yarn that is activated if one yarn is reported broken. By default the yarn is considered intact and thus the failure flag has a value of 0. If the yarn is reported broken, the value of the failure flag is set to 1. This flag is defined as a state variable, meaning that the state of the yarn is propagated between steps. Erosion of the element takes place only when both yarns are broken.

Step-28: eroding of shell element. Quite simply, if at one point in the analysis the two failure flags both have values of one then the state variable controlling the erosion of the element is set to zero. This is a capability in user material that Abaqus provides in case we want to remove an element from the analysis. By default when the element is active in the analysis, the value to this state variable is one. In our case state variable 30 is dedicated to element removal.

Step-29: obtain the fabric stress increments for each yarn. From the tensions in the yarns T_i we can calculate the components of the stress tensor increments in the material frame. In this case at increment n for warp and fill yarns the tensors are:

$$\sigma_{W_{mat}}^n = \begin{bmatrix} \frac{T_W}{A_W} & 0 \\ 0 & 0 \end{bmatrix} \quad \text{and} \quad \sigma_{F_{mat}}^n = \begin{bmatrix} \frac{T_F}{A_F} & 0 \\ 0 & 0 \end{bmatrix} \quad (6.30)$$

where A_i is the cross-sectional area of the concerned yarn. The tensors of equation (6.30) can accommodate further model developments if other yarn stress components are required.

Step-30: Transfer data from mesoscale to macroscale level by computing the stress in the Green Naghdi frame. The tensors above are expressed in the material frame and must be transformed into the Green-Naghdi frame so it can be properly read by Abaqus. We use the transformation matrix θ_i^n that we have previously defined (this transformation matrix θ_i^n is not defined yet) as such:

$$\sigma_{i_{GN}}^n = \theta_i^{nT} \sigma_{i_{mat}}^n \theta_i^n \quad (6.31)$$

6.2.7 Shear response

As we already mentioned before, plain weave fabrics display unconventional shear behavior due to the specific arrangement of the yarns in the weave structure. The fabric can shear easily up to a certain value of locking angle, from which the yarns then get compacted laterally to resist any further shearing. The shear response of a crossover is subdivided into three distinct regions depending on the transverse compaction of the fibers. From a micro-mechanical point of view, shear is permitted while the reduction of spacing between adjacent yarns is possible; it's only the shear modulus that varies. To define the transverse compaction of the yarns that ultimately defines the shear modulus to be applied, we have to define the angles β_1 and β_2 separating each region as one can see in Figure 6-7 which presents one fourth of the unit-cell. The principle of shear modelling has been extensively described in section 3.6.2 and the picture frame test is presented in Figure 3-11.

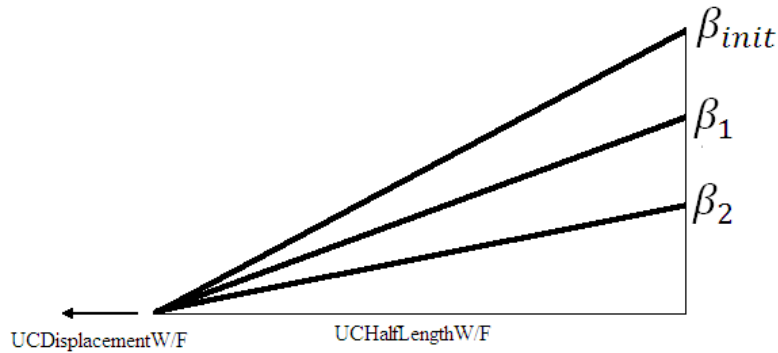


Figure 6-7: Yarn centerline height position depending on angle β

The first region between β_{init} and β_1 is where the fiber is able to rotate freely and does not get compacted, there is very little friction between the two perpendicular yarns and a very small shear modulus is applied. The second region between β_1 and β_2 is where the yarn is getting compacted, the yarns rotation is progressively impeded and as a consequence, the shear modulus increases linearly. The third region starting from β_2 is when the yarn has been compacted up to 65% of its original width as Shahkarami underlines it in his work (4). At this point the applied shear modulus is high. The definition of the yarn's crimp angles β was taken and interpreted from the works of Shahkarami (2), presented in Figure 6-7 and has been defined as follows:

Angle β_1

$$\sin \beta_{1i} = \frac{|YarnWidth_{i_{init}}|}{UCHalfLength_{i_{init}}} \quad (6.32)$$

$$\sin \beta_1 = \frac{\sin \beta_{1W} + \sin \beta_{1F}}{2}$$

Angle β_2

$$\sin \beta_{2i} = \frac{|0.65 YarnWidth_{i_{init}}|}{UCHalfLength_{i_{init}}} \quad (6.33)$$

$$\sin \beta_2 = \frac{\sin \beta_{2W} + \sin \beta_{2F}}{2}$$

Step-31: calculate the shear strain of the trellis mechanism from the knowledge of the strain increment tensors for the warp and fill yarns computed before.

$$ShearStrainInc = StrainIncW(1,2) + StrainIncF(1,2) \quad (6.34)$$

Step-32: calculate β to assess the compaction of the fiber

$$\sin \beta_i = \frac{|H_i|}{UCHalfLength_i} \quad (6.35)$$

$$\sin \beta = \frac{\sin \beta_W + \sin \beta_F}{2}$$

Step-33: define the shear modulus for the trellis. Using the locking angles β_1 and β_2 , the corresponding shear strains γ_1 and γ_2 can be determined. Shahkarami in his work transforms the angles β into their corresponding strains before calculating the shear modulus. In our VUMAT we applied directly the knowledge of the angles describing the compression of the fibers to the computation of the proper shear modulus to be used in following computation. The results presented in the following chapters show that this modification has no negative impact; it is yet a way to avoid doing unnecessary computations of the strains. The shear stress-strain relationship can be formulated as in Shahkarami et al (2) and is given as follows:

$$G = \begin{cases} G_1 & \text{si } 0 < \beta \leq \beta_1 \\ G_1 + \frac{G_2 - G_1}{\beta_2 - \beta_1} (\beta - \beta_1) & \text{si } \beta_1 < \beta \leq \beta_2 \\ G_2 & \text{si } \beta \geq \beta_2 \end{cases} \quad (6.36)$$

A relationship exists between the shear angle and shear modulus for values smaller than zero that means the shear model for positive and negative values of the angle is the same and shown in Figure 6-8.

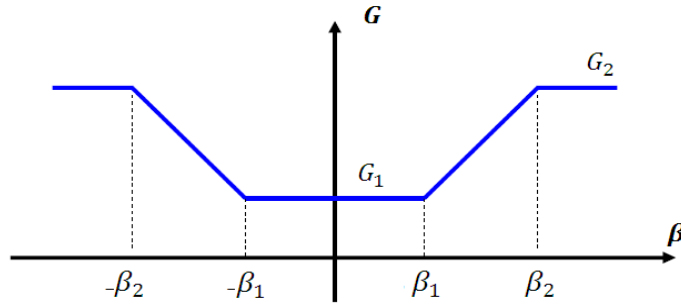


Figure 6-8: Shear modulus as a function of β

Step-34: compute the shear stress

$$ShearStress = G12 ShearStrainInc + StressOld(k, 4) \quad (6.37)$$

6.2.8 Final computations

Step-35: calculate the stress tensor of the unit cell in the Green-Naghdi frame and return the computed stresses to Abaqus. The total stress tensor is an average of the two yarn stress tensors as calculated below:

$$\sigma_{avg\ GN}^n = \frac{\sigma_{1\ GN}^n + \sigma_{2\ GN}^n}{2} \quad (6.38)$$

An extra term should be added to account for the stresses generated by the in-plane shear phenomenon as we already discussed. The additional shear term can easily be determined from the knowledge of the shear angle between two yarns since the two material vectors of the yarns are updated at each time increment.

6.2.9 Intermediate result extraction

Abaqus gives the user the ability to extract some of the results of the calculations performed inside the subroutine. This is very useful if we want to observe the behavior of the VUMAT during the analysis and monitor the evolution of a specific variable to verify that the given results are in accordance with the mechanics of the problem. This is done by using the user variables in Abaqus, thus we simply define a set of these user variables and assign specific results to them. The variables are written by Abaqus at each time step. For example, we can extract the tensile force in warp and fill fibers as well as the shear angle between the fibers. The complete list of user variables is available in chapter 7.

6.3 Shell element testing

In order to use the shell element in an impact application, we first have to define all the parameters the VUMAT needs to work with. These parameters are mostly material properties as it will be seen in the next paragraphs. Also we have to make sure its behavior is coherent with the behavior of the 3D yarn crossover model under various loadings.

The analyses presented here have been performed on a single smeared shell element with applied displacements on the shell edges with the shell element's material law given by the VUMAT user material modeling one crossover of plain woven fabric.

6.3.1 Input parameters for the VUMAT

The determination of input parameters using the 3D crossover model has been performed in the previous chapter. The full listing of the input parameters and the value attributed to each one is shown in appendix 2.

6.3.2 Uniaxial extensional response

The first analysis performed is a uniaxial extension test with a displacement of 0.05mm applied on the warp yarn (direction 1) as shown in Figure 6-9.



Figure 6-9: Application of the loads on the shell element for a simple extension test

The curve extracted for this analysis is presented in Figure 6-10 shows build up of tension in the yarn as a function of displacement.

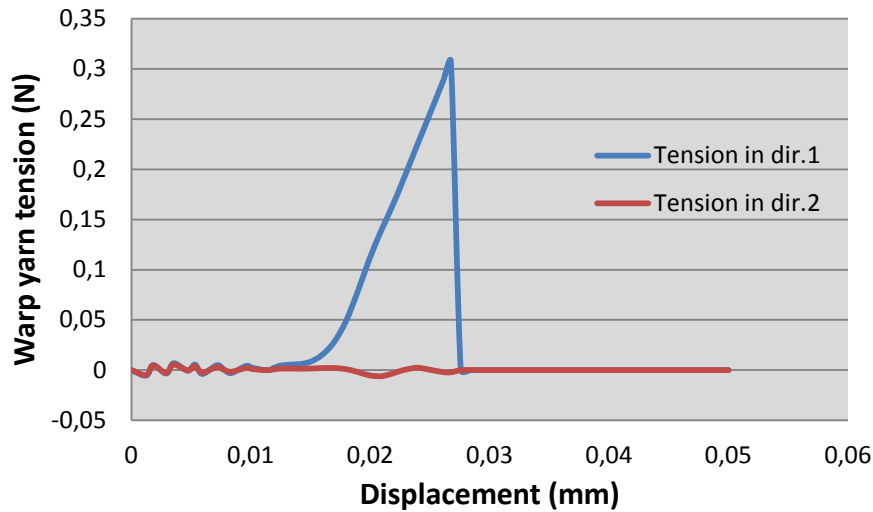


Figure 6-10: Tension in the warp yarn during a simple extension test

The blue curve clearly shows a tension taking place inside the warp yarn. First there is a non-linear phase until the displacement reaches a value of 0.01 mm. We observe a relatively small tension applied in both yarns even though displacement is applied in one direction. This is a symptom of fiber placement which takes place when the yarns are rearranging inside the woven. Then, the tension in the fiber is almost linear as the displacement increases. The tension reaches the tension limit set up in Abaqus and then rupture occurs. No tension is supported by the yarn at this point on in the analysis.

The same results have been obtained by Shahkarami (2) (see Figure 6-11) but we could not compare the curves directly since he provided the results only for Kevlar S-726 while we used

the material properties for Kevlar S-720 to conduct our tests. To give the reader an idea of the loading curve's shape in unidirectional tension obtained by Shahkarami we presented it in Figure 6-9. One can observe that the S-720 Kevlar has a lower crimp percentage (3.21%) than the crimp percentage for Kevlar S-726 (3.44%). This results in a rupture of the S-720 yarn at a slightly lower displacement than the Kevlar S-726.

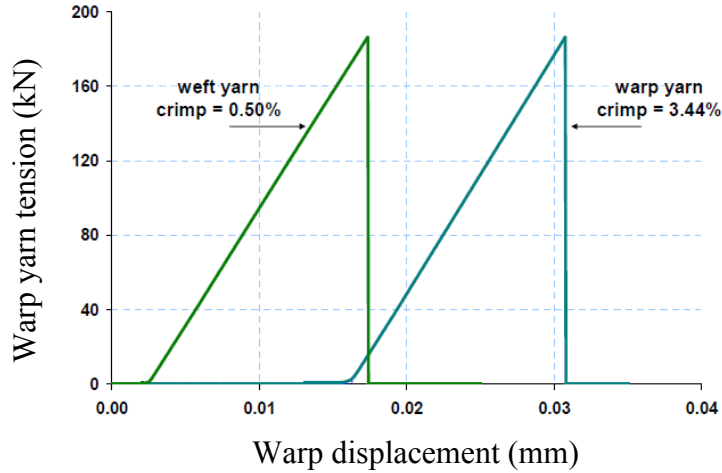


Figure 6-11: Shahkarami et al. (4) unidirectional tensile loading curve for Kevlar S-726

It is also important to observe the movement of the yarn centerlines at the crossing point. While tension develops only in the warp yarn it tends to straighten. Physically, the reduction of undulation in the warp yarn implies that the fill yarn will get more undulated, that is shown in Figure 6-12.

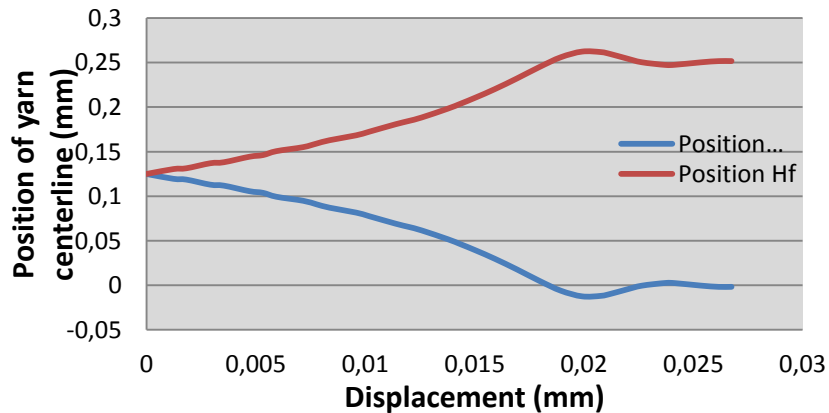


Figure 6-12: Movement of the warp and fill yarn centerline at the crossing point during a simple extension test

6.3.3 Biaxial extensional response

In this case, the objective is to test the biaxial tension on the smeared shell element. The displacement applied on each side of the shell element is set to 0.05 mm and the tensile forces appearing in each yarn are extracted. In this biaxial test there is no yarn placement since the yarns are initially in contact and the decrimping that occurs is the same for both yarns. Consequently, as soon as the displacement is applied, the tension in the yarn is increasing linearly as one can see in Figure 6-13.

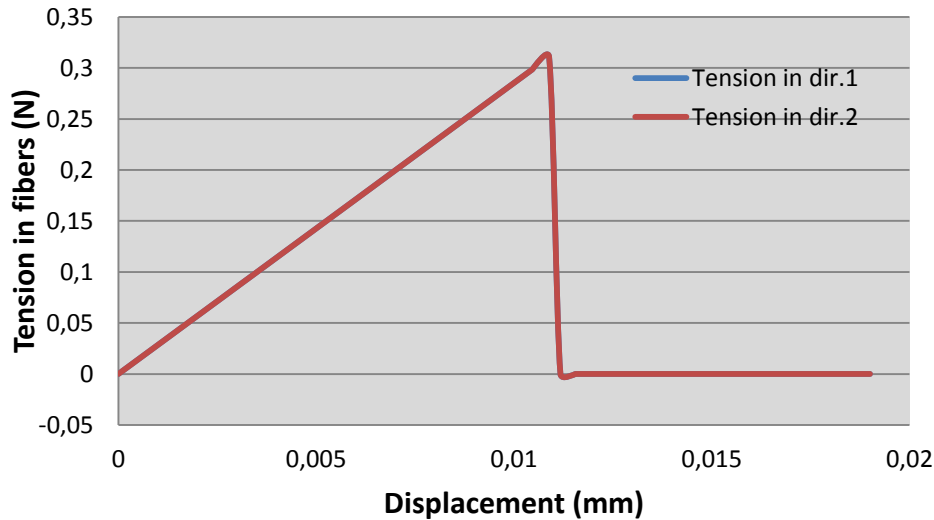


Figure 6-13: Tension in the warp yarn during a biaxial extension test

Also, one can observe that in the case of a biaxial extension, the ultimate tensile resistance of the yarns is reached for a smaller displacement than what we have observed in the uniaxial tensile test. For a displacement of 0.01 mm, both yarns fail at the same instant and then the element is removed from the analysis.

Concerning the position of the warp and fill yarn centerlines, their variations is very small. As the crossover gets extended, the warp and fill yarns pack against each other and their cross-sectional area gets flattened in the z-axis. As it was determined during the transverse compaction test on the 3D crossover, the yarns have some resistance in transverse compression. This is why a progressive and very small variation of the centerlines' position is observed as shown in Figure 6-14.

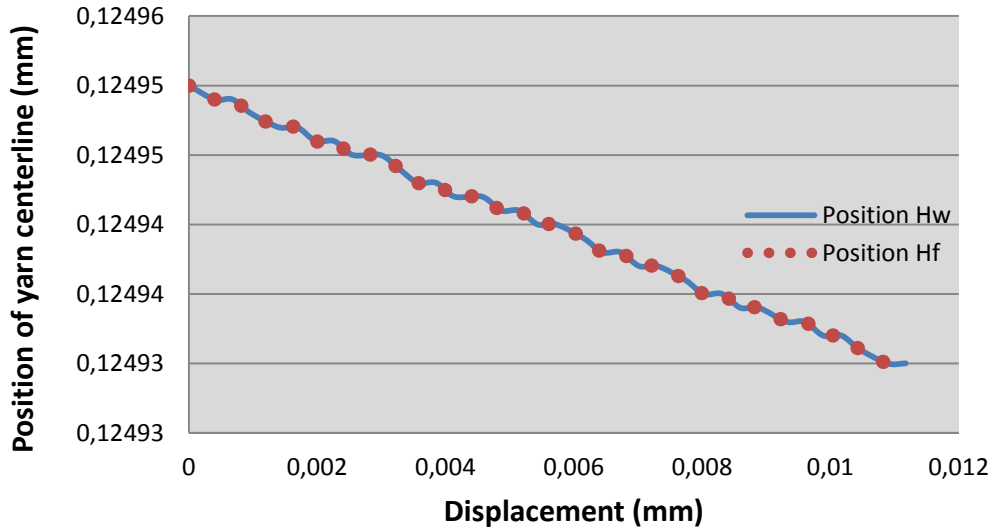


Figure 6-14: Movement of the warp and fill yarn centerline at the crossing point during a simple extension test

One can observe that in the case of a biaxial extension the two directions exhibit the exact same variation of the centerline position in the normal direction of the shell element.

6.3.4 Shear response

The shear response of the unit cell which was obtained has the same form as the theoretical shear response taken from the works of Shahkarami (4). Figure 6-15 gives the shear response that was obtained.

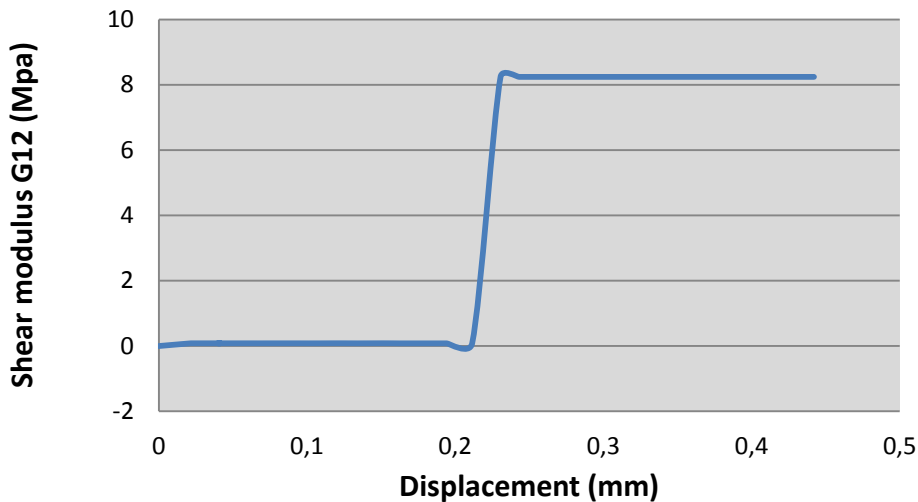


Figure 6-15: Shear modulus evolution as a function of the transverse displacement of the yarns

It can be observed that the shear modulus is greatly varying from a zero value up to the limit value of 8.24 Gpa.

6.4 Conclusion

In this chapter, we went over the definition of the trellis mechanism that was used to approximate the behavior of the crossover as well as the simplifying assumptions we made. All equations used at each step of the calculations in the developed VUMAT were detailed.

Finally, we tested the VUMAT using only one shell element under various loadings. These loadings were uniaxial tension, biaxial tension and shear.

CHAPTER 7 - MODELING OF A BALLISTIC IMPACT ON A COMPOSITE PLATE

In this chapter we discuss the modelling of a ballistic impact problem on plain weave reinforcement using Abaqus. In this work one ply is first used to assess the validity of the model and then extended to two and four plies. The extension to multiple plies was necessary in order to fully understand and set up the contact between plies using Abaqus' capabilities.

The goal in this study is first to monitor the velocity of the impactor during its interaction with the composite plies. Then the analysis results are compared with those obtained by Shahkarami (2) using his own VUMAT. A parametric study is also performed to study the influence of a number of selected parameters over the analysis results.

7.1 Analysis set-up for 1-ply model

The analysis setup presented here follows the necessary steps to create a model in Abaqus using the explicit package to handle the transient dynamic nature of the impact and the large deformations that are taking place.

Quite simply, the model is constituted of the metallic projectile and of a plate whose material is the fabric described by the VUMAT. The elements used for the plate are S4R shell elements available in Abaqus and the initial sidelength of the shell elements we used is 0.94 mm because it is the typical size of the crossover geometry. We will see later in the chapter that an increased size can be used for shell elements without loss of accuracy in the results.

7.1.1 Geometrical setup of the analysis

First of all, only one quarter of the total model has been used to reduce the number of elements and thus to reduce the computation time needed to complete the analysis. In order to capture an accurate behavior of the plain weave structure, a detailed analysis is very important; hence the mesh has to be quite refined. For geometric modelling, we defined two parts in our analysis: one for the plain weave ply, which is a two dimensional square of approximately 97 millimeters and the other for the impactor which has a specific parametric solid geometry adapted from the works of Shahkarami (4). The particular geometry of the impactor is given in Figure 7-1. All dimensions are given in millimeters.

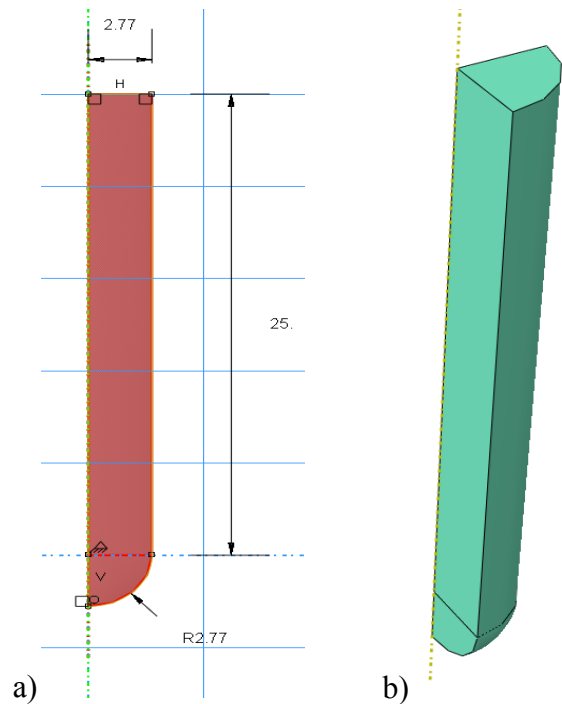


Figure 7-1: a) Impactor section definition in the sketch module, b) final three dimensional geometry of the impactor to be used in the assembly

The impactor initial position is set pretty close to the ply to reduce the distance it has to travel before impacting the ply. This also helps to reduce the computational time of the analysis. The final geometric model and set up of the analysis is represented in Figure 7-2.

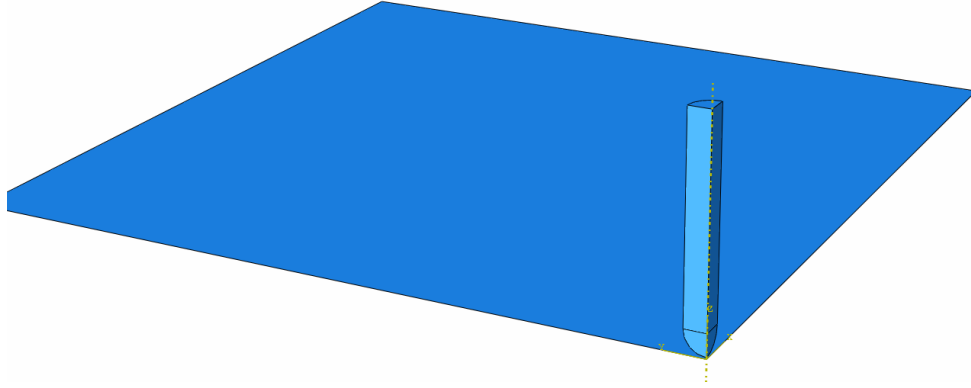


Figure 7-2: Model assembly with impactor and fabric plate

7.1.2 Definition of the materials

The impactor material was selected to be steel; which has the great advantage over aluminium of staying perfectly rigid throughout the analysis. Because aluminium projectile reaches its limit plastic deformation and stress, it is less reliable and interesting to use it as it adds an unwanted complexity to the numerical experimentation. The elastic mechanical properties of steel that we used are presented in Table 7-1:

Table 7-1: Mechanical parameters of the steel impactor

Property	Value used in Abaqus
Density	7.922
Young's modulus (Gpa)	210
Poisson's ratio	0.3

For the ply fabric material, a user material subroutine was developed through the Abaqus VUMAT subroutine facilities and used to specify the fabric model and to define the behavior of the plain weave ply under impact loading. The user material model requires to input 19 material properties to define weave architecture parameters into Abaqus in order to satisfy the user

subroutine input requirements. These input values are taken from the works of Shahkarami (42) and are summarized up in Table 7-2:

Table 7-2: Summary of parameters used by the VUMAT to define the fabric

Symbol	Property	Value entered in Abaqus
d	density	1.44
E_w	Young's modulus in warp direction (Gpa)	96
E_f	Young's modulus in fill direction (Gpa)	96
ν	Poisson's ratio	0.3
H_w	Height of the warp yarn centreline (mm)	0.12495
H_f	Height of the fill yarn centerline (mm)	0.12495
h_w	Unit cell initial half-length in warp direction (mm)	0.47035
h_f	Unit cell initial half-length in fill direction (mm)	0.47035
A_w	Warp yarn cross sectional area (mm ²)	0.149664
A_f	Fill yarn cross sectional area (mm ²)	0.149664
T_w	Ultimate tensile force in warp direction (N)	0.315
T_f	Ultimate tensile force in fill direction (N)	0.315
G_{init}	Initial shear modulus (Gpa)	0.0824
G_{max}	Maximum shear modulus (Gpa)	8.24
C_{max}	Maximum fiber compression coefficient	0.65
a	Fiber compression coefficient a	0.12389
b	Fiber compression coefficient b	984.32
t_w	Initial thickness of the warp yarn	0.2499
t_f	Initial thickness of the fill yarn	0.2499

7.1.3 Definition of the step

A dynamic explicit analysis was set up in Abaqus and in our analysis the time is given in milliseconds. The total analysis time is set to 200 milliseconds which corresponds to the time needed for the projectile to go through the ply at a velocity of 100 m/s. The incrementation parameters are handled automatically by Abaqus. We instructed Abaqus to output all the energies, stresses, displacements and velocities variables every 10ms during the analysis simulation. Also, non-linear geometric analysis options are activated to account for the non-linear nature of the impact analysis (large deformation).

7.1.4 Definition of the boundary conditions

Three types of boundary conditions were introduced during the analysis definition. First to rigidly set the plate in space, the Abaqus “encastre” option was used on two edges of the plate to set all its degrees of freedom to zero. Since only a quarter of the problem was modelled, it is necessary to specify geometric symmetry boundary conditions. This is done by using the options X-symmetry and Y-symmetry depending on the edge of the model we want to constrain. Lastly, the initial velocity of the impactor was set up by using a predefined field to be applied to the whole impactor geometry. Because in the analysis the time is set to be in milliseconds we applied a 0.1m/ms velocity along the Z-axis which is equivalent to a velocity of 100 m/s. All other velocities in other space directions are set to zero. Boundary conditions are summed up in Figure 7-3.

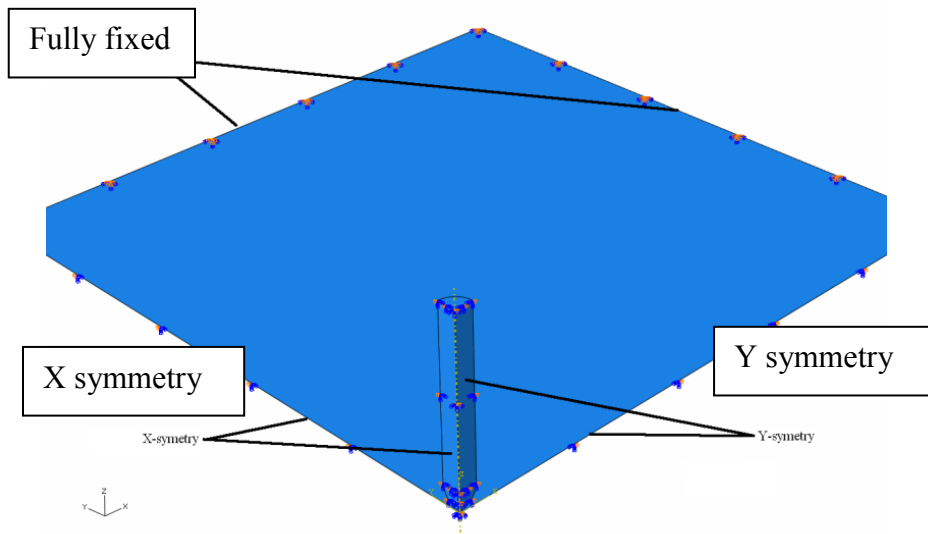


Figure 7-3: Boundary conditions applied on the model

7.1.5 Transverse shear stiffness

Using the shell elements we have to provide Abaqus with values for the transverse shear stiffness when defining the thickness of the shell in the section module. Only a linear-elastic transverse shear response of the fabric can be defined in Abaqus and this requires specification of these two moduli directly in the guest user interface. The values used in the simulations have been taken from Grujicic’s work (1) in which it is stated: “Low values for the transverse normal

and shear moduli and for the Poisson's ratios arise from the fact that the fibers bundled within yarns are only weakly coupled to each other". The values used are $G_{13}=3.28$ Gpa and $G_{23}= 3.28$ Gpa for a Kevlar 129.

7.1.6 Interactions and contact properties

For this analysis, the "Surface-to-surface contact" option available in Abaqus was used and specified by picking the two surfaces involved in the contact. The master surface is the composite ply and the slave surface is the impactor. The mechanical constraint formulation is the penalty contact method. Also, a contact control was defined, essentially to define the angle criteria for the elements' highly warped facet. This value was set to 40 degrees, meaning that if at one point during the analysis the face of an element exceeds the criterion, the analysis will issue a warning message. Doing this allows one to monitor if any element is getting abnormally deformed thus providing inaccurate results. This was not the case in the present situation.

7.2 Analysis results discussion for 1-ply analysis

The graphical results of the analysis are given below; they were extracted from the .odb file to show the evolution of the stresses in the fabric ply near the contact zone between the ply and the impactor. The evolution throughout the time of the analysis is shown in Figure 7-4.

Various shell element sizes to mesh the plate were tested to analyse the impact behaviour of the VUMAT. First a mesh size a quarter of the size of the representative volume element was used and yielded similar results when compared to a plate modelled with shell elements the size of the crossover as is presented in Figure 7-13.

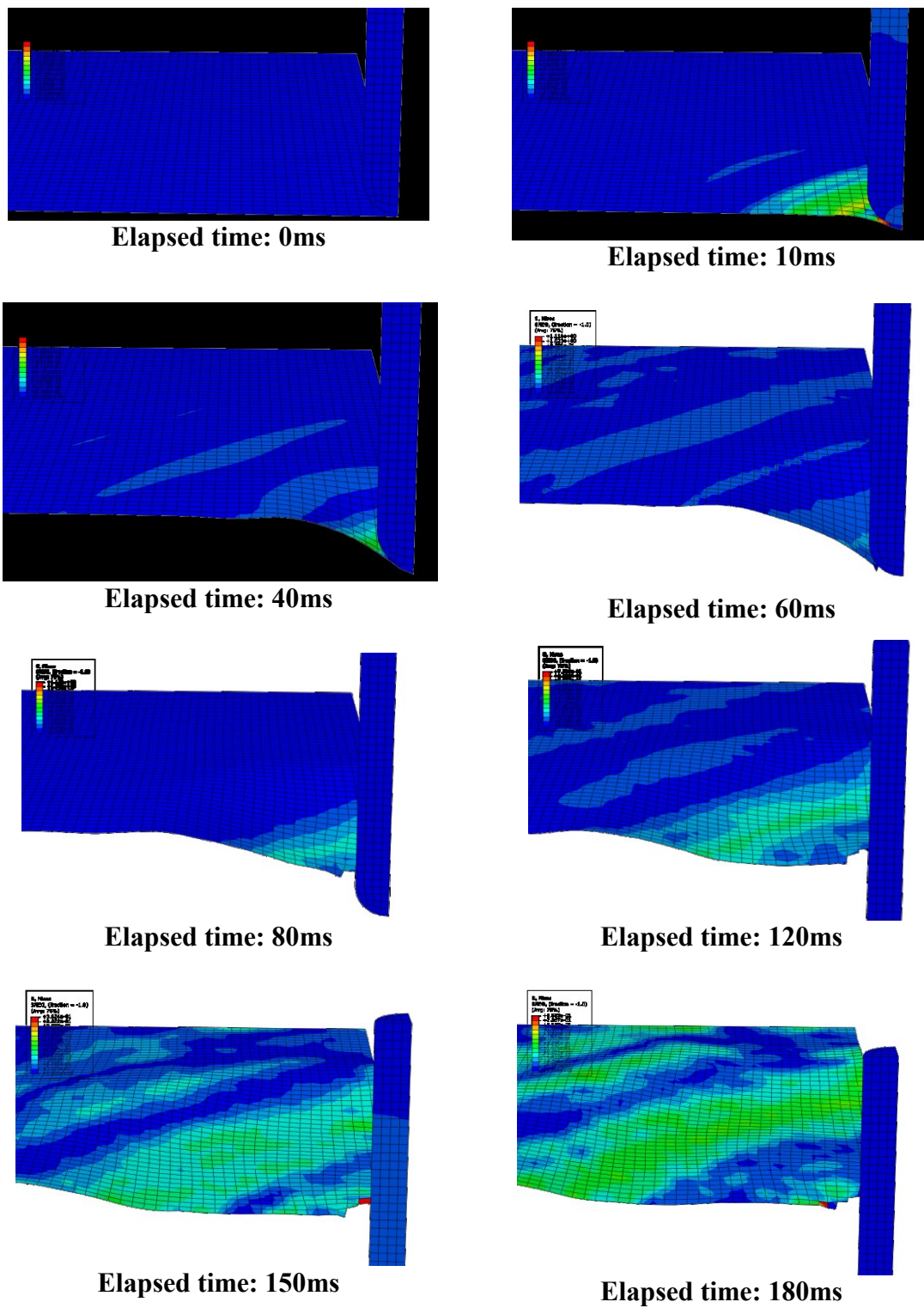


Figure 7-4: Evolution of the impact analysis on a one-ply plain weave fabric over time (in milliseconds)

We can observe in Figure 7-4 that the stress waves in the fabric are propagating outward from the impact point. At the beginning of the analysis, the fabric behaves like a net trying to stop the projectile. We may observe that the fabric is getting deformed, dragged by the tip of the projectile advances until the yarns in both direction are straightened. This is the kind of behavior that was also obtained in Shahkarami's works (31). After 60 milliseconds into the analysis, the tensile stress in the fabric yarns reach the limit, irreversible damage occurs and thus element erosion starts. This indicates that the tensile stresses developed in both warp and weft yarns are greater than the ultimate tensile load given by the manufacturer for the material. At this point the fabric is damaged and is letting the projectile passes through.

Overall, only a fraction of the projectile kinetic energy is absorbed by the fabric until it fails. As we observe that the projectile perforates the composite ply we deduce that one ply is not enough to stop the impactor from its initial velocity of 100 meters per second.

7.2.1 Projectile velocity analysis

From the impact experiment over one ply of fabric we can plot the projectile velocity over the total time of the analysis as it is shown in Figure 7-5. The initial velocity of 100 m/s decreases during impact to approximately 85 m/s and then remains constant. This indicates that the projectile is transmitting some energy to the composite but still has enough left to perforate the fabric.

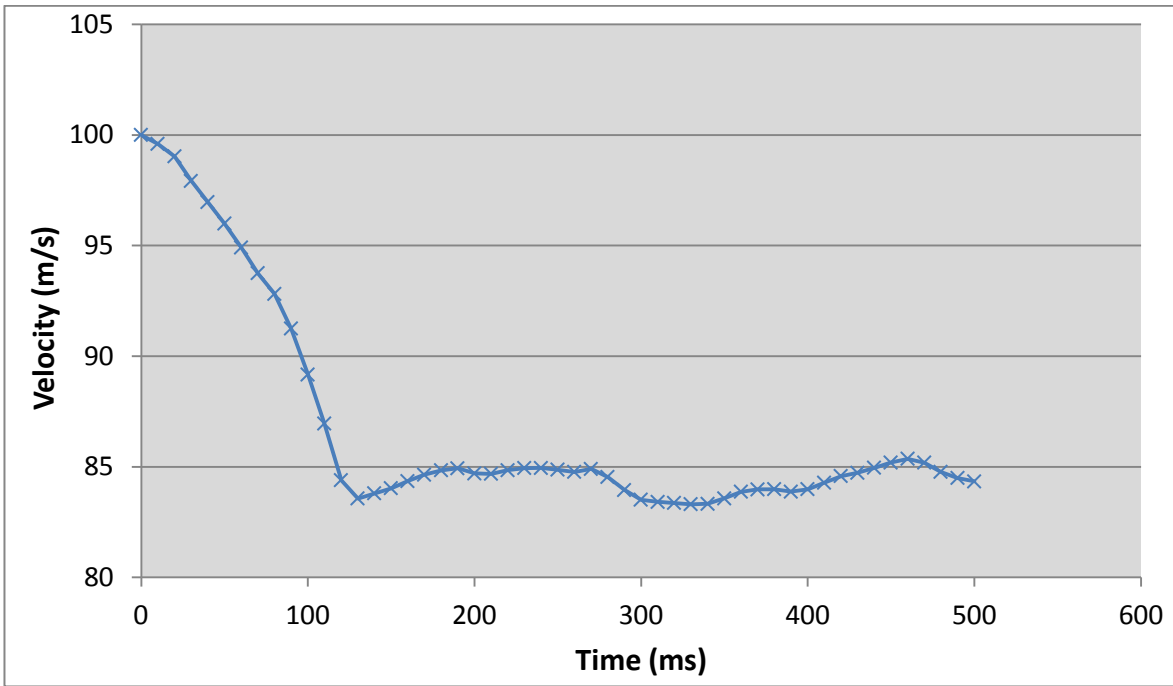


Figure 7-5: Projectile velocity result

7.2.2 Parametric study

To fully understand the effect of certain parameters on the results of the model, a simple parametric study was carried out in order to assess their effects on the speed of the projectile throughout the analysis. The studied parameters are:

- The crimp of the fabric
- The initial velocity of the projectile
- The impacted fabric plate size
- The compression parameters a and b

7.2.2.1 Velocity variation analysis

Three different initial velocities of the projectile were tested thus changing the kinetic energy. Plotting the velocity of the projectile (Figure 7-6) through the analysis enables us to observe that the end velocity of the projectile is not decreasing in the same way.

When initial velocity is set to 125 m/s, the residual velocity is 115 m/s thus the decrease is only 10 m/s. An initial velocity of 100 m/s will lead to a decrease of 15 m/s and an initial velocity of 75 m/s leads to a decrease of 20 m/s. Thus, we can conclude that the model is adequately predicting the velocities by following the kinetic energy law.

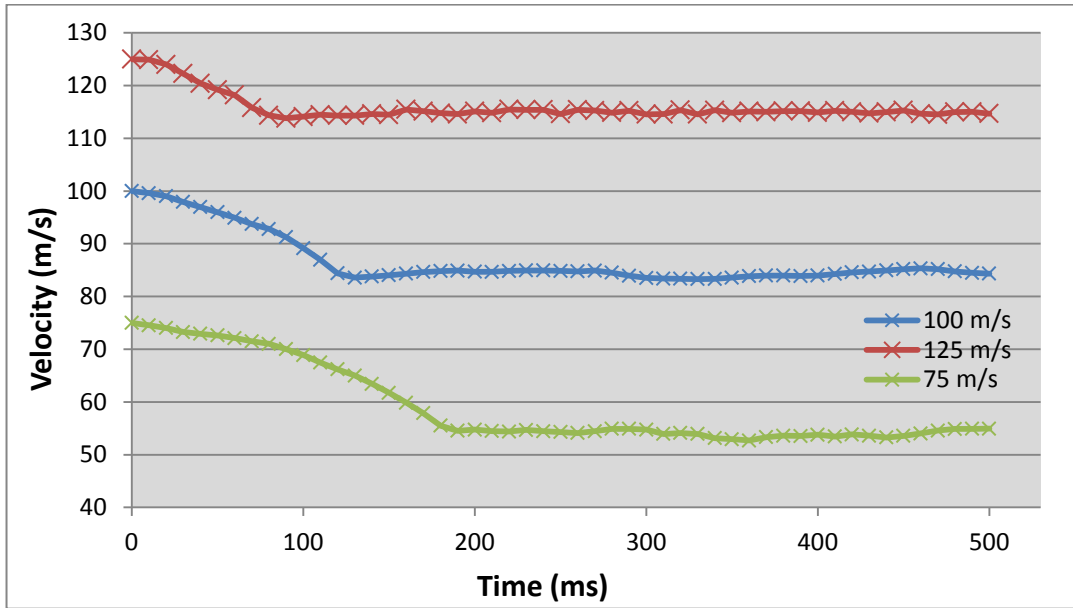


Figure 7-6: Initial velocity influence over projectile velocity during the analysis

7.2.2.2 Crimp variation analysis

To study the effects of the crimp angle (which is the angle at which one yarn crosses over the other) on the fabric ability to absorb the projectile’s energy, we run three models with three different crimp values for the fabric. The influence on the velocity of the projectile through the analysis is plotted in Figure 7-7. We can observe that the crimp value has a significant influence on the results of the analysis. It has an influence on the energy absorption capability of the fabric, and this corresponds to typical result one was expecting.

Indeed, changing the crimp of the fabric is directly affecting its ability to deform by modifying the amount of possible yarn straightening. As a result, a large crimp angle means that the fabric will be able to absorb more energy because the straightening phenomenon of the yarns will be increased. The fabric can deform greatly until the yarns are straightened completely. This is exactly what can be observed in Figure 7-7.

For an initial velocity of 100 m/s, a large value of crimp can modify the straightening phenomenon so much that one ply of fabric would be able to stop the projectile.

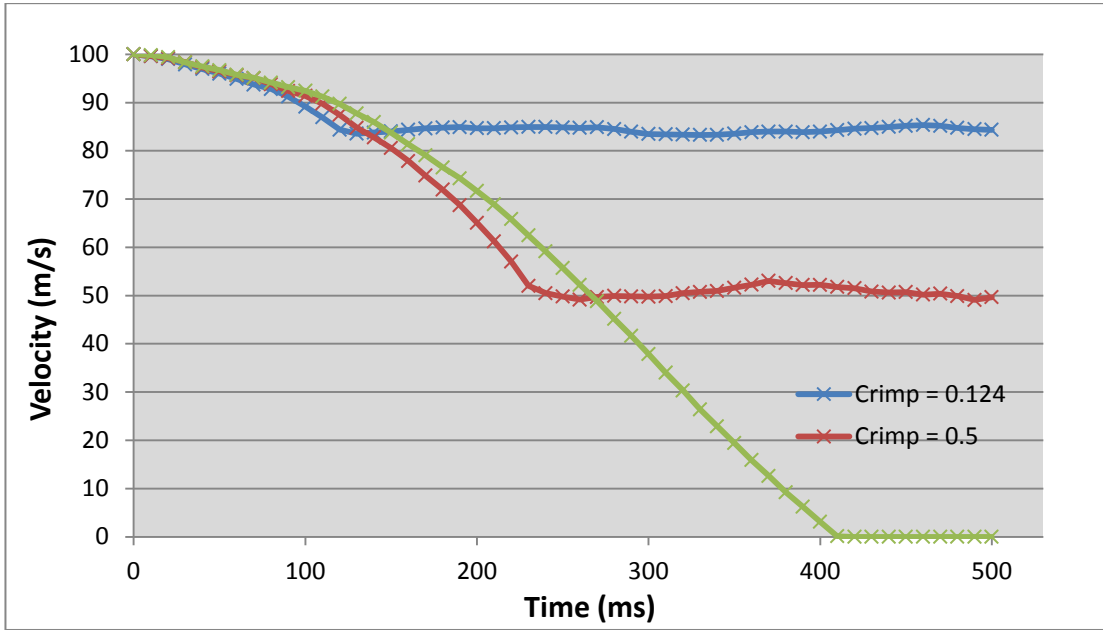


Figure 7-7: Crimp influence over projectile velocity during the analysis

7.2.2.3 Plate size influence

The effect of the composite plate size was also studied (Figure 7-8) to observe if the fixed boundary condition applied to the edges of the plate had influence over the results of the analysis. We wanted to observe if the chosen dimension of the plate for all analysis was affecting the results we got in other analysis.

All plates are squares and the given dimension is the sidelength. We may observe that plate dimension has a great influence over the results. For a plate sidelength of less than 47 millimeters the velocity of the projectile after impact is a third of the velocity we obtain using a plate sidelength of 97 millimeters.

This can be easily explained by the fact that there is a reduction in the number of elements. If the same mesh size is used, in the case of a 97 x 97 square millimeters plate we have 100 elements on the edge, while we have 50 elements in the case of a 47 x 47 square millimeters plate. This leads to the fact that there is less possible deformation of the elements in the latter

case (i.e. fewer elements to be bent) and as the fabric stretches less, it absorbs less energy and the projectile velocity after the impact is greater.

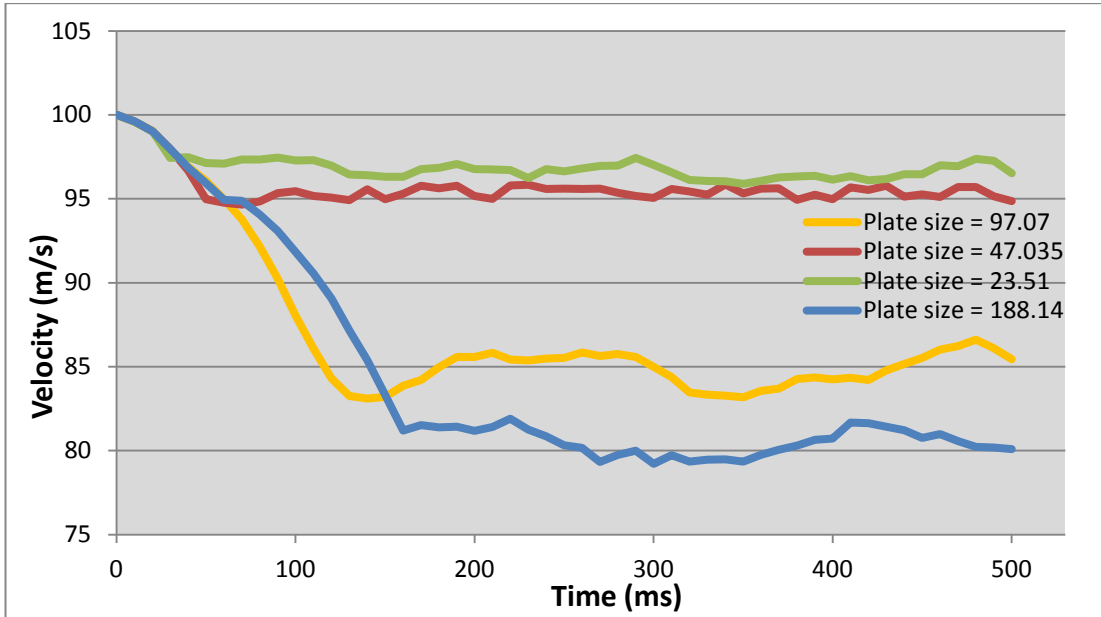


Figure 7-8: Plate sidelength influence over projectile velocity during the analysis

7.2.2.4 Compression parameters influence

The last parameter study (results shown in Figure 7-9) was concerned with the influence of compression parameters a and b linking the contact force F_c between the yarns with the contact over closure d_c . The relation was defined as:

$$F_c = \frac{b d_c}{a - d_c} \quad (7.1)$$

We conducted five analyses to assess the influence of these parameters by modifying each parameter separately as it is presented in Table 7-3.

Table 7-3: Parameter a and b variation

Study case	a	b
Case 1	0.154862	984.32
Case 2	0.092917	984.32
Case 3	0.12389	1229.225
Case 4	0.12389	984.32
Case 5	0.12389	737.535

The original values determined by using the full blown 3D crossover model correspond to case 4. Figure 7-9 presents the influence of parameter a and b variation on the projectile end velocity. We may observe that a $\pm 25\%$ variation of each value has little influence over the overall result of the analysis. This is what one would expect since the rigidity of the crossover in compression is not affecting directly the calculation of the tensile loads inside the yarns. The knowledge of the overclosure and contact force between yarns is used to define the equilibrium and thus the position of the crossover.

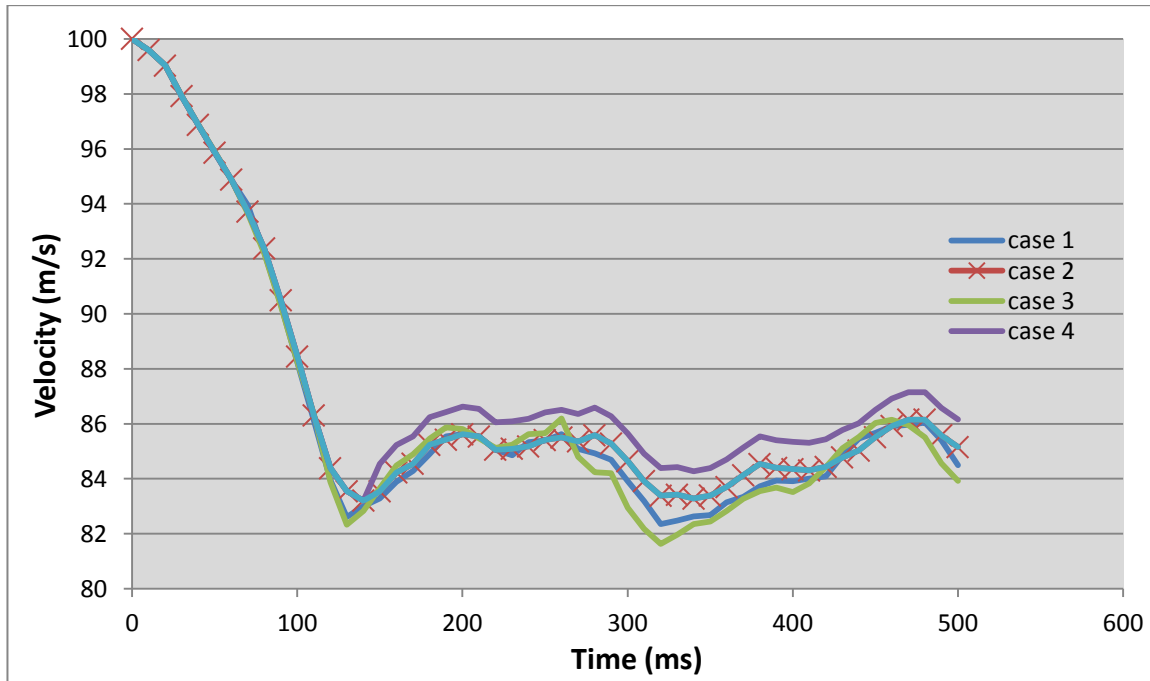


Figure 7-9: Compression parameters influence

7.3 Analysis results and discussion for 4-ply analysis

Since for one ply fabric model, perforation is taking place, the next step is to study the influence of the number of plies on the fabric response.

Going forward in our analysis we set up a model for the impact on a 4-ply composite plate. This was selected because ELVS experimental data were available for validation of the obtained numerical results. The General Contact option with no friction between each plies was used during the analysis to handle the contact between the plies and between each ply and the projectile. The initial velocity of the projectile was selected to be 120 meters per second in order

to be able to compare the generated velocity versus analysis time curve with the one obtained during the experimental tests of Shahkarami (2).

7.3.1 Graphical evolution of the analysis

The evolution of the projectile as it impacts the composite is shown in

Figure 7-10. Looking closely to the figures, one can observe that the fabric is getting deformed and that some elements around the impact zone on the top layer are fully damaged and then deleted automatically from the model.

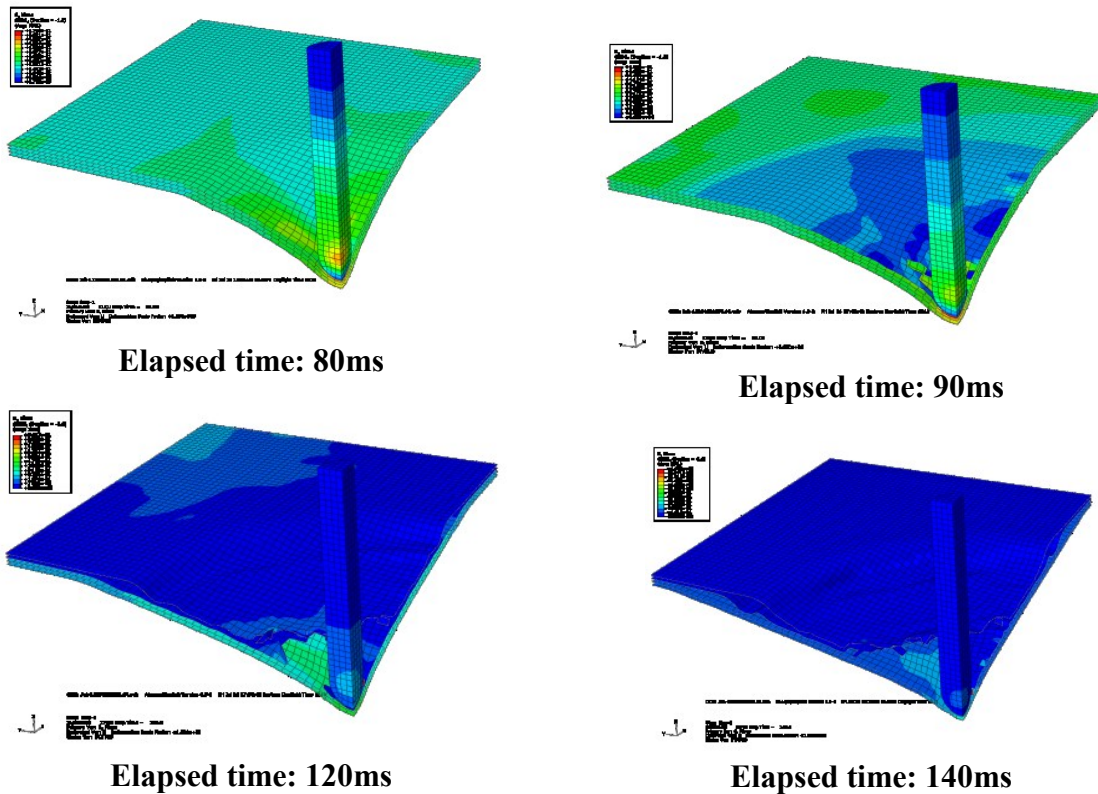


Figure 7-10: Evolution of the ply stresses on a four-ply plain weave fabric over time (in milliseconds)

In this analysis the projectile does not go through the composite and is stopped at 200 milliseconds into the analysis.

7.3.2 Energies plots to validate the analysis

To validate the analysis we extracted the energies of the global model as shown in Figure 7-11. The total energy of the model is conserved throughout the analysis with no major disturbance. The kinetic energy is converted entirely into internal energy as the projectile's energy is absorbed by the fabric because the projectile is stopped by the four layers of fabric. We also observe on the energy curves that the kinetic energy is near zero at 205 milliseconds which indicates that the projectile has been stopped. This result correlates with the FEM analysis showing that the velocity of the impactor is near zero at around 200 milliseconds. We may thus conclude that the analysis is valid.

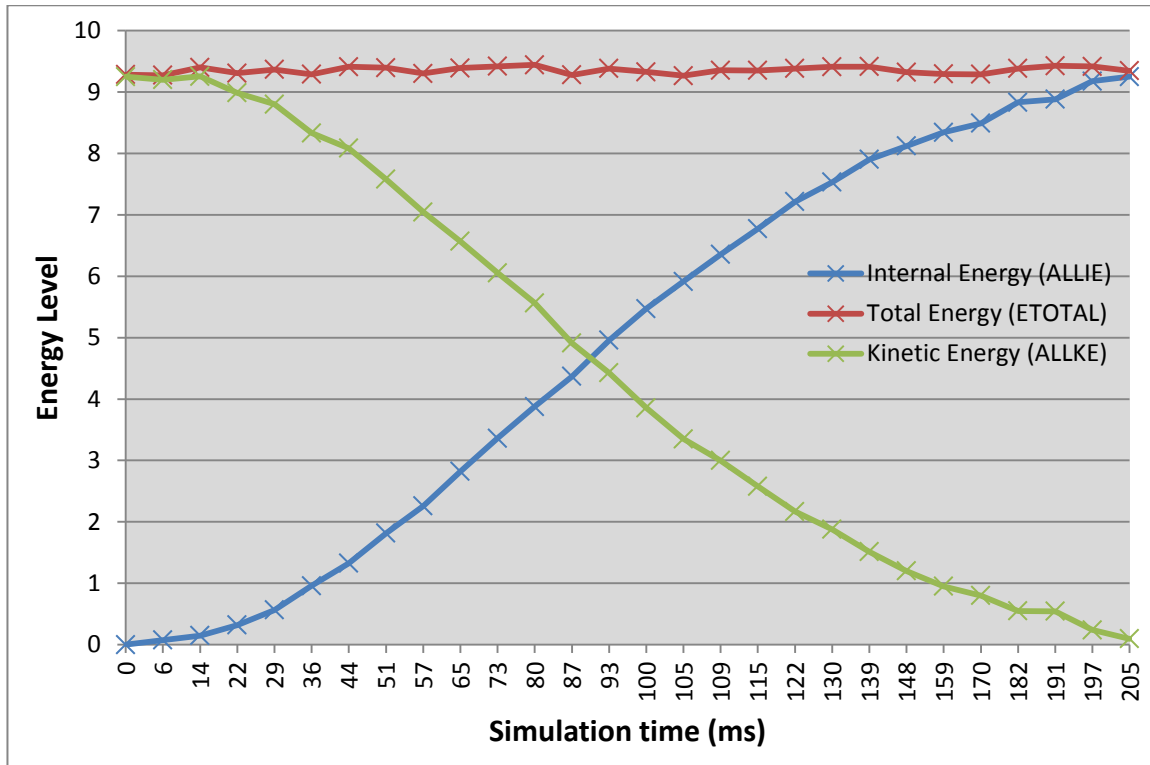


Figure 7-11: Evolution of the kinetic, internal and total energy of the system over time (in milliseconds)

7.3.3 Comparison between FEM analysis and experiment

The experimental results obtained in G. Toussaint (5) thesis to validate an LS-Dyna Fabric UMAT model obtained from Shahkarami (2) and the our FEM results obtained from the VUMAT model implemented in Abaqus show a very good correlation as shown in Figure 7-12.

The physics are captured by our VUMAT and therefore the principal mechanical phenomenon which were selected and implemented within the subroutine is adequately modeled.

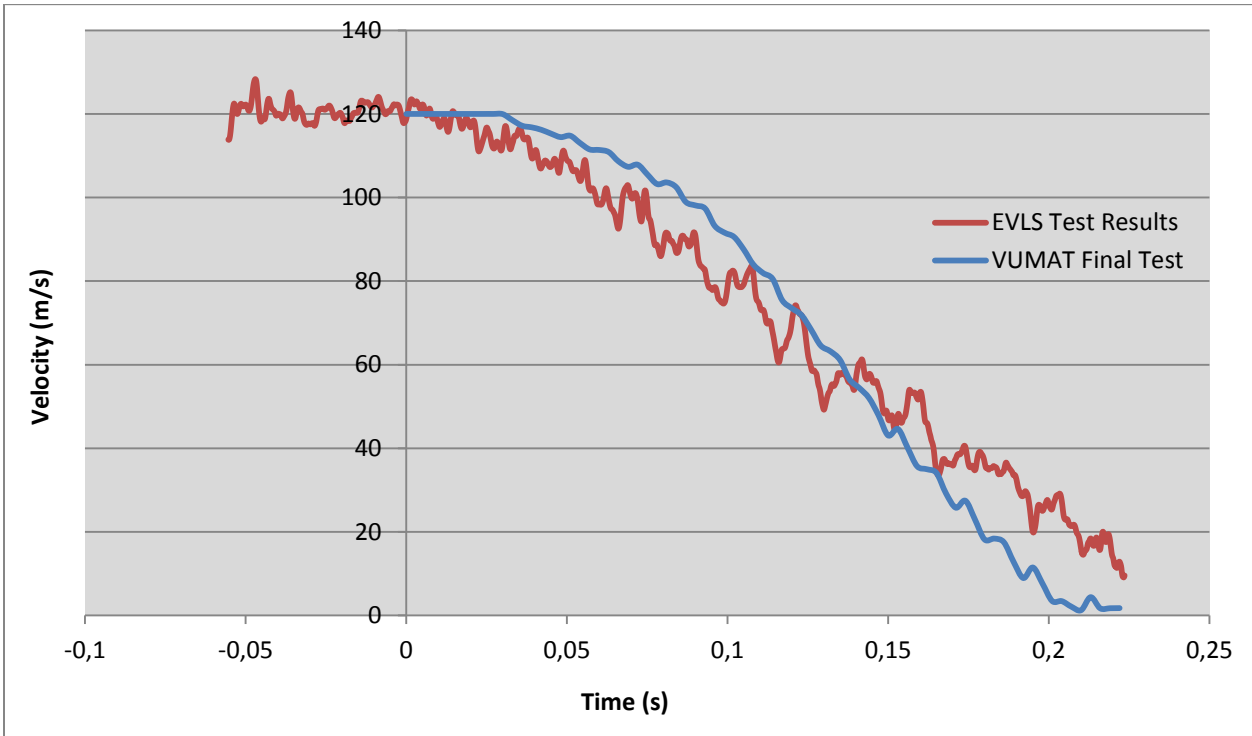


Figure 7-12: Comparison between FEM and experimental analyses from Shahkarami (4) of the impact velocity

7.3.4 Mesh size influence on projectile velocity

Finally we wanted to evaluate the influence of the mesh size over our results. This analysis was carried out with the impact model on a 4-ply composite. It was also done to understand to what extent the results of the VUMAT were valid regarding mesh size.

7.3.4.1 Reduction in mesh size

The first analysis carried out was to verify that a refined mesh four time smaller than the size of the RUC (i.e. the nominal mesh size used for the comparison of the projectile velocity to the experimental results given by Shahkarami (2)) yielded results similar to those obtained using the nominal mesh size. This is to investigate if it would be necessary to locally refine the mesh around the projectile impact location to obtain more accurate results. As is shown in Figure

7-13 a refined mesh gives similar results compared to the nominal mesh size. It is thus not necessary to refine the plate mesh.

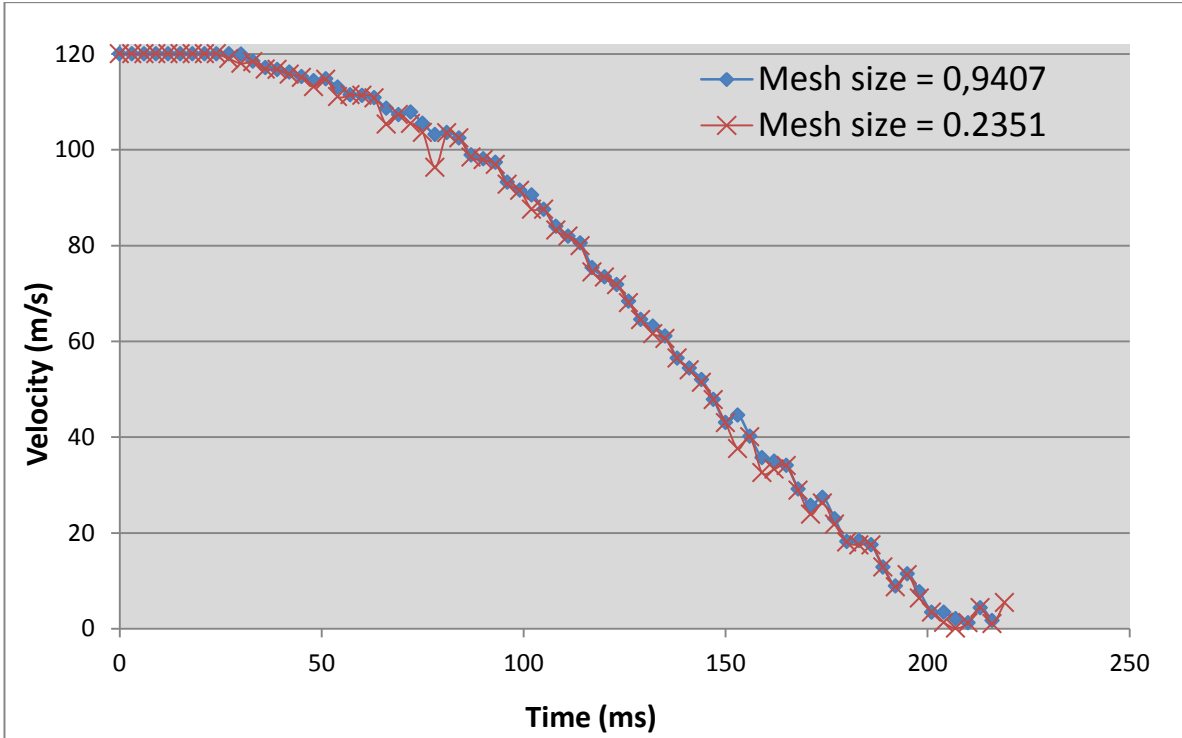


Figure 7-13: Mesh size influence over the results compared with the results obtained with the nominal mesh size

7.3.4.2 Increase in mesh size

In the industry it is very computationally inefficient to apply a very refined mesh on large structures and so it is interesting to see how accurate the results are if the mesh size is increased. Thus we carried out several analyses to investigate the variation in the projectile's velocity results. Doubling the size of the mesh appears to have little influence on the results. Overall an element size of 2 mm leads to an average error of 7.1% over the total time of the analysis as compared to the 0.9407 mm element sidelength. The 4mm element leads to an average error of 51% and the 6mm element leads to an average error of 70% overall.

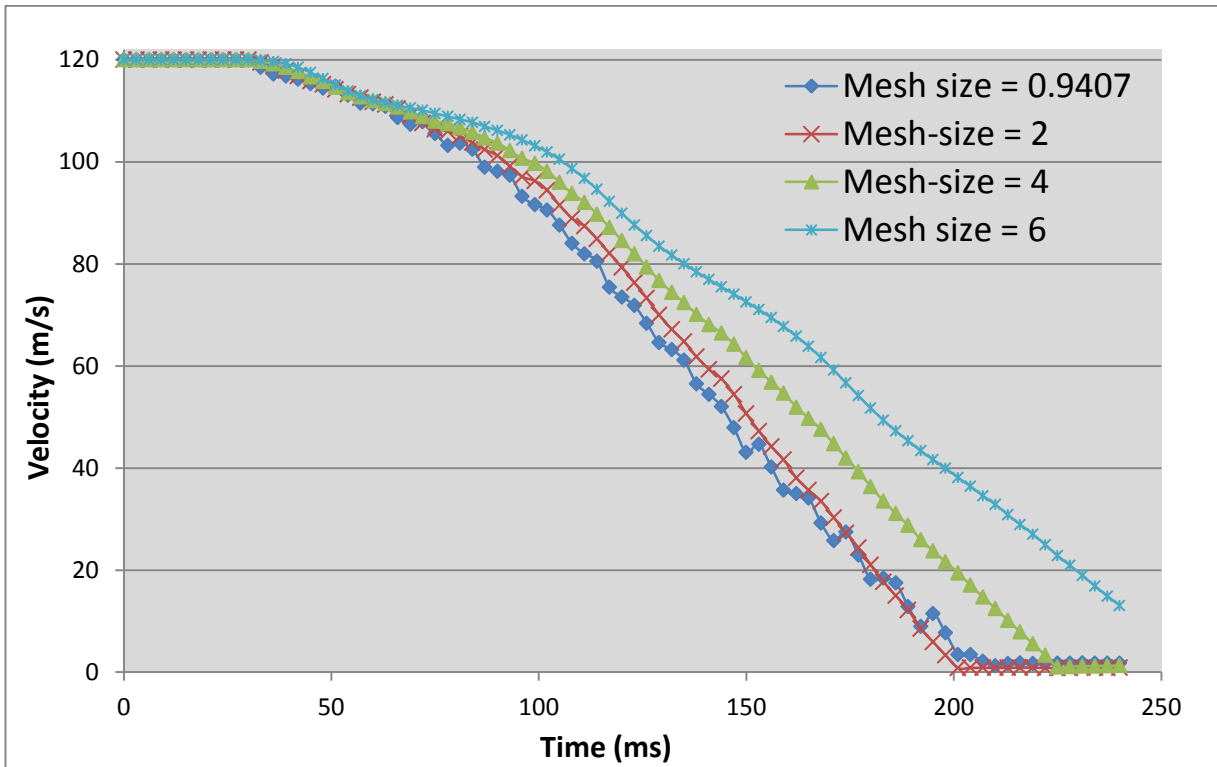


Figure 7-14: Mesh size influence over the projectile velocity throughout the analysis

In conclusion, as observed in Figure 7-14 we may use the 2 mm shell element to improve the computational efficiency of the analysis and still obtain relatively accurate results. Use of element sizes greater than 4mm is not recommended because the results are not accurate.

7.4 Final velocity comparison between different layup configuration

In Figure 7-16 we show a simple study on the impact of the projectile on a plate made of increasing number of fabric layer. This study was carried out to find out if we were able to predict the number of layers needed to prevent penetration of the projectile based on some partial information. Indeed the computation time needed to obtain result increases drastically with the number of layers.

We first collected the final velocities after impact on a one-ply plate, a two-ply plate and a four-ply plate. All other parameters such as initial velocity, crimp angle of the fabric, element size remain the same for all analysis. In the case of the one-ply impact, the final exit velocity of the

impactor is 82 m/s. In the case of the two-ply plate, it is 58 m/s and in the case of the four-ply impact the final post impact exit velocity is 18 m/s.

Also we run an analysis for a six ply plate which we found out to be the configuration needed to prevent perforation by the projectile, the curve is showed in Figure 7-15. We also show the graphical stress result extracted during the analysis in Figure 7-17. Of course this result was not taken into account for the predictions.

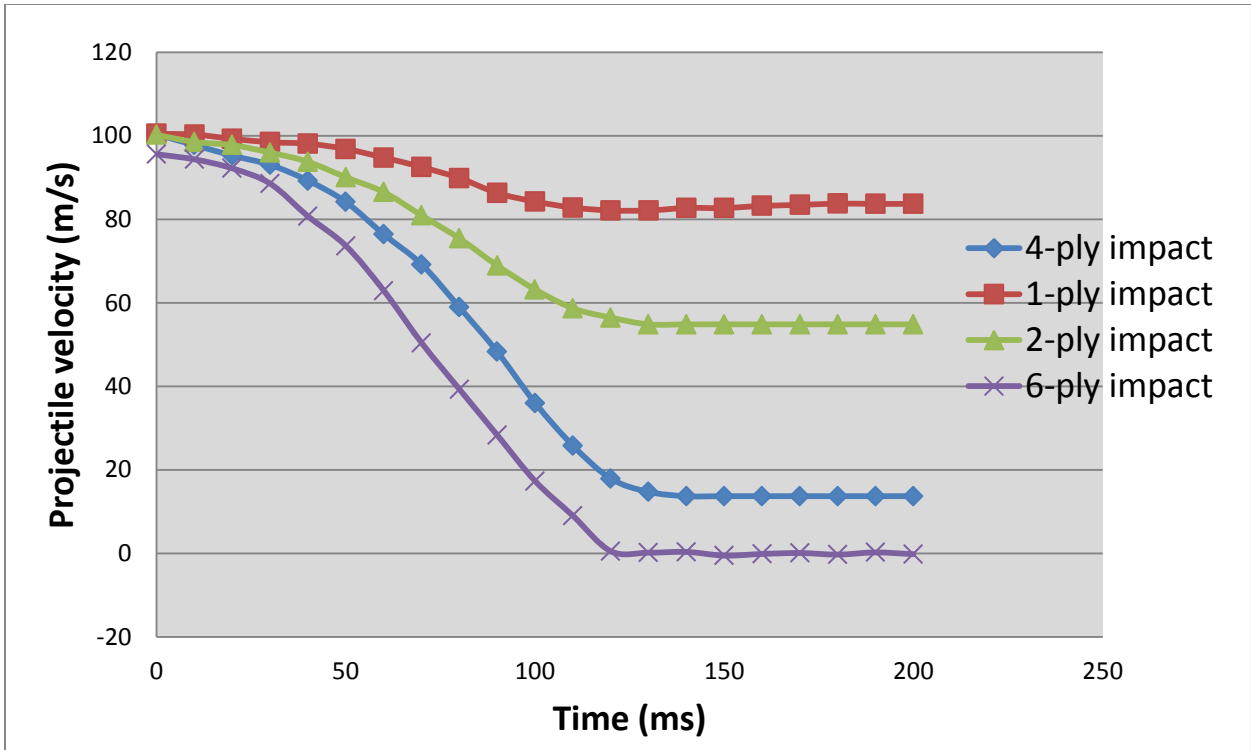


Figure 7-15: Influence of the number of layers over the final velocity of the projectile

Plotting each final velocity for one-ply, two-ply and four-ply impacts we were able to create a quadratic function in Excel interpolating each of three results. This is presented in Figure 7-16. The quadratic function has the following equation where X is the number of layers:

$$f(X) = 2.7639X^2 - 37.161X + 118.12 \quad (7.1)$$

Using this equation, it was possible to predict the number of layers needed to stop the projectile. The projections for five and six layers of fabric are shown in Figure 7-15 in red. We can observe that five layers are not enough to stop the projectile as the projected residual velocity is

3 m/s. The right number of layers is six and it is interesting to note at this point that this is the result we get from Abaqus.

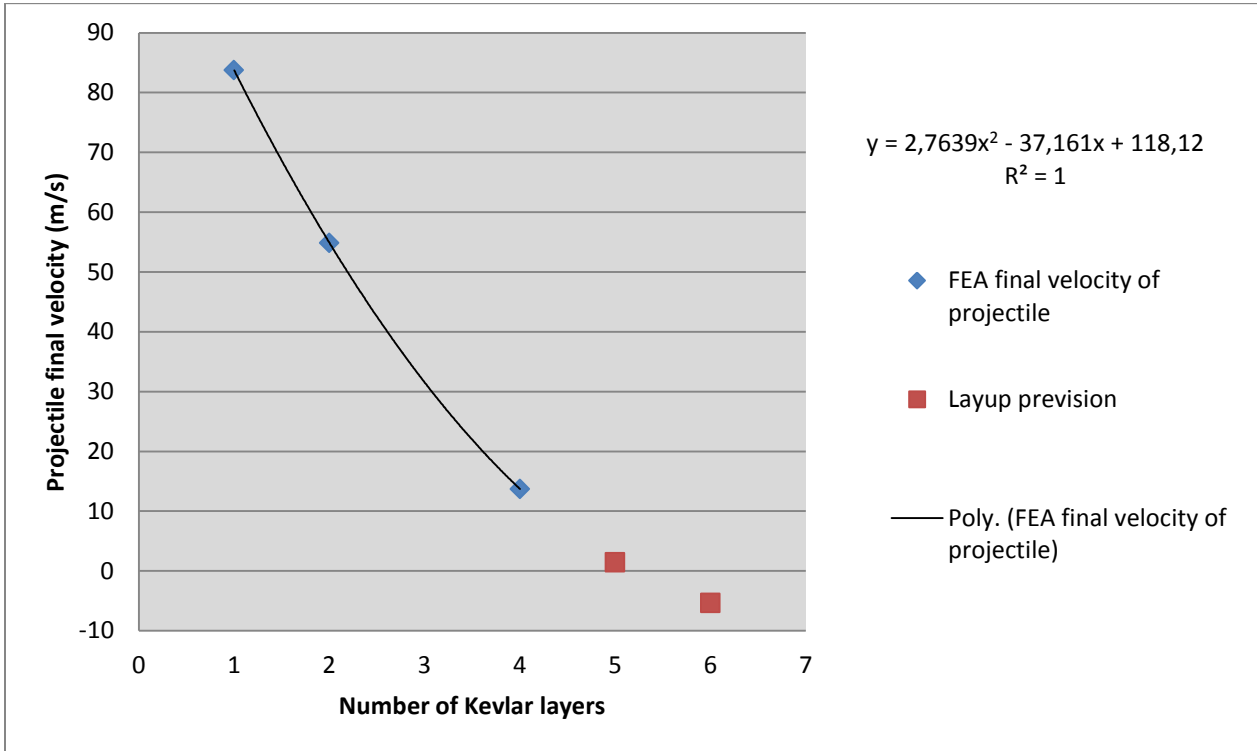


Figure 7-16: Prediction analysis to define the number of layers needed to stop the projectile

Consequently we can conclude that for this simple impact test our predictive model based on equation 7.1 that links the final velocity of the impactor with the number of fabric layers is correct. This technique will also be used to predict the number of layers needed in the hybrid casing to stop the fan blade which is the object of the next chapter.

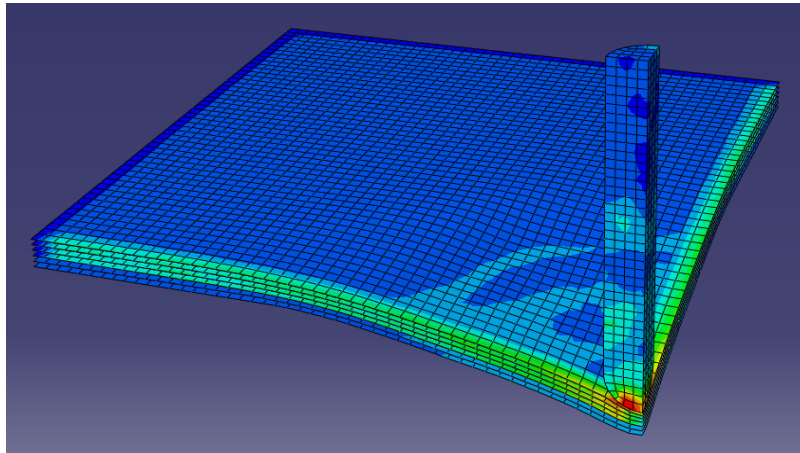


Figure 7-17: Stresses caused by the projectile stopped by 6 layers of plain weave fabric

7.5 Conclusion

In this chapter, numerical tests of a projectile impacting on a fabric plate were conducted. The influence of the number of plies on the post impact residual velocity has been studied. Also we studied the influence of various other material parameters that were input in the VUMAT to assess their influence over the results.

Predicting how many plies are needed to prevent complete perforation of the fabric target by the projectile based on partial simulation was a key objective of the chapter. We found out that it is indeed possible to predict the number of needed plies and this prediction has been verified with numerical testing. This methodology will be used in the predictions of fan blade containment within a lightweight hybrid engine casing.

CHAPTER 8 - MODELING THE IMPACT OF AN ENGINE FAN BLADE ON A COMPOSITE CASING

8.1 Overview of the analysis

In this chapter, a simplified engine fan blade containment problem is considered as an application of the work done in previous chapters. All the parameters and model geometry of this chapter are taken from the works of Toussaint (5) in order to compare the results between her FEA model and ours. The analysis comprises two separate modeling steps: (i) a pre-stress model for initialization of field variables induced by setting up the motion of the fan blade from rest to cruise rotating speed; (ii) the model for blade debris release and its impact with the engine casing. The modeling technique is thus interesting in the sense that we use a first model to pre-constrain the fan blade following the rotating motion built-up and then use the results to start the subsequent impact analysis. The setup of these two models is dealt with using specific tools and functionalities of Abaqus.

The first analysis is solely concerned with the fan blade and is used to obtain the initial stresses and strains appearing in each element as well as the velocities of each node of the fan blade model when it is put in rotational motion. In Abaqus, this motion is defined by specifying an

axis of rotation and a rotational velocity as well as multipoint constraints (MPCs). This analysis phase is performed using Abaqus implicit solver, i.e. Abaqus standard. The results of this first analysis are then imported in the second analysis which deals with the impact of the fan blade debris on the engine casing. In this second analysis phase, a new part, called engine casing, is created and assembled with the previous fan blade model. A hybrid engine casing is modeled using an aluminum ring as the base structure defining the casing shape around which a dry fabric composite material is wrapped. For high velocity impact modeling involved in this containment simulation the Abaqus explicit solver is used together with the developed VUMAT user subroutine.

Details regarding the modeling methodology of the first and second sub-models for the fan blade impact analysis are first presented in the chapter. Then the results regarding the velocity of the blade during the impact will be presented. And finally discussion about the validity of the simulation results are presented by taking a look at the energy curves from the model.

8.2 First analysis setup: fan blade rotation

8.2.1 Analysis basics

We will use an implicit integration scheme in the first analysis since it is suited for large analysis durations. This algorithm is unconditionally stable and it is based on solving the following equation to compute the acceleration, velocity and displacements:

$$M\ddot{u} + C\dot{u} + Ku = F \quad (8.1)$$

Solving this equation requires, for realistic models, to compute, assemble and invert large matrix arrays which makes the implicit scheme very demanding in computational time. In our case this is not a concern since the model of the blade that is analysed has been greatly simplified following the work of G. Toussaint (5).

8.2.2 Defining the geometry

As it was mentioned previously, the objective of the first analysis is to obtain the pre-stresses in the blade elements and the velocities at the nodes of the damaged fan blade induced by setting

up the blade rotating motion from rest to cruise speed. In order to obtain these results, we first have to define the overall simplified geometry of the fan blade based on the one used by G. Toussaint while working with LS-Dyna. The geometry was slightly modified as it is shown in figure 8.1 b). For example we do not use four fan blades but only one since we found out that for our purpose, it is not necessary to model the other three: they do not interact with the casing. Also, after trying the configuration proposed by G. Toussaint (5), the outer edge of the blade has been modeled using a curve instead of a straight line.

These modifications helped greatly to obtain good convergence of the contact algorithm and reduced the computational time during these preliminary impact computations. The modification of the outer edge was partly motivated by the fact we noticed that during the first instants of the impact there was a high concentration of stresses and strains at one of the sharp outer edges of the blade (circled in red in the figure 8-1 a)) and the contacting shell elements of the casing. In other words, while the blade was piercing through the casing very few elements were involved in the contact and that caused the analysis to be unstable and eventually crash. We identified that this problem arises from the contact algorithm which was dependent on the size of the shell elements of the casing and blade. Since we did not want to use shell elements of a size smaller than 0,94 mm, we decided to modify the geometry instead. Ultimately the revised geometry improved the convergence of the contact algorithm and enabled us to perform the complete analysis.

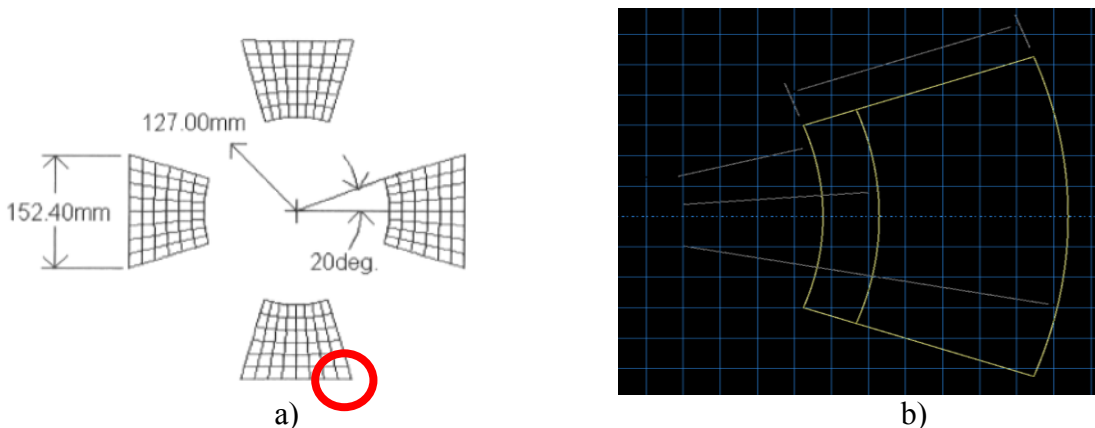


Figure 8-1: a) Fan blade geometry as defined by G. Toussaint (5). b) fan blade geometry defined in Abaqus for the present work

We can also observe in figure 8-2 that the fan blade is modeled into two distinct features or parts. This is because in the experiments, the fan blade is supposed to break in two pieces: one that remains attached to the rotating shaft and the other that is ejected outward to impact the casing. This subtlety in the modeling of the blade enabled us to model the crack that is of great importance in the impact analysis.

8.2.3 Defining the material of the fan blade

The thickness of the blade shell elements is 4.98 mm and the properties of Table 8-1 were input in Abaqus. These properties have been used in LS-Dyna by Toussaint (5) to model the material of the blade and are given in Table 8-1.

Table 8-1: Titanium properties for the definition of the fan blade

Young's Modulus	115.1424 Gpa
Poisson's Ratio	0.35
Plastic: yield stress	0.8273709 Gpa
Plastic strain	0
Mass density	4.424
Fracture Strain	0.25
Stress Triaxiality	0.3
Strain Rate	10

8.2.4 Constraining the model

There are two kinds of coupling that we need to set up in the model. First, we need to attach the base of the blade to the control point at which we apply the boundary conditions to define the rotational motion as we can observe in Figure 8.2 a). The other coupling is used to attach the two parts of the fan blade as is shown in Figure 8.2 b).

A coupling constraint has been defined between the reference point and the nodes at the base of the blade where the junction between the blade and the rotating shaft is located. This coupling constraint will transmit the radial velocity applied to the reference point to the fan blade. Since it is a velocity we want to transmit, one has to select the kinematic coupling type. The control point of the constraint is set to be the reference point that would be located on the axis of rotation of the engine's shaft and the slave nodes are the nodes at the base of the blade.

For the impact analysis, we had to pre-define the crack in the fan blade since the blade has to be broken into two different sub-components that will be used in the subsequent explicit analysis. Thus, to join the two parts of the fan blade we need to set another constraint. We used the tie constraint available in Abaqus as it is able to rigidly connect two sets of nodes very close to each other. The master set of nodes is constituted of the nodes at the base of the fan blade and the slave set is constituted of the nodes of the tip of the fan blade. We positioned the pairs of interacting nodes in a manner so that each of the two nodes sets has the same spatial location.

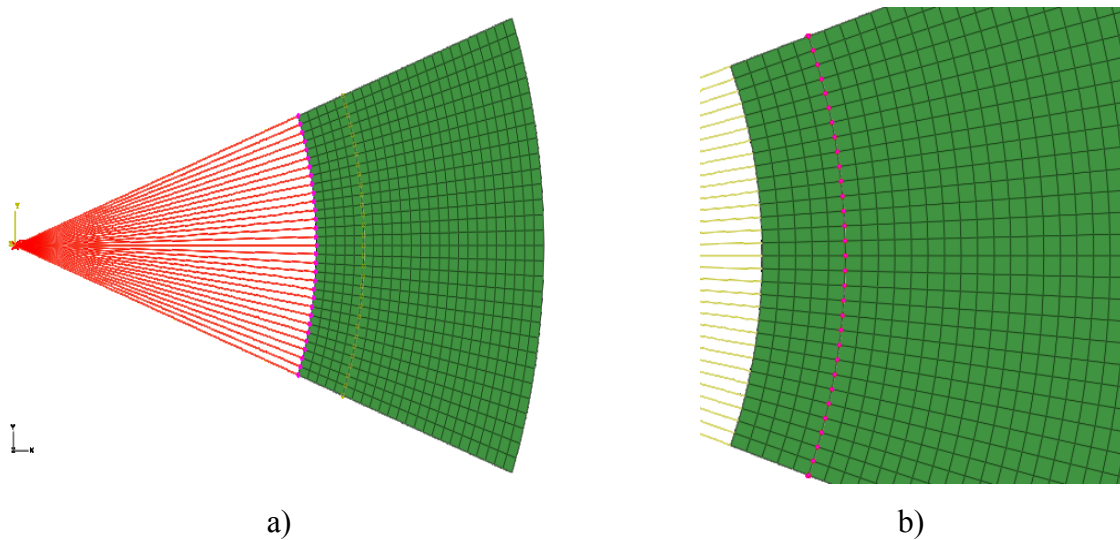


Figure 8-2: a) Coupling constraint between the control point and the base of the fan blade. b) Tie constraint between the two sub-components of the fan blade.

In this case, the two parts of the blade are rigidly connected and thus behave the same way as a blade modelled with only one Abaqus part. The junction between the two parts is shown in Figure 8-2.

8.2.5 Applying the boundary conditions

To set the rotating motion, we applied a velocity boundary condition to the reference point. We deny (impeded) any displacement of the point in each of three directions of space thus setting their values to zero. Then as the axis of rotation is the Z-axis, we set the value of the angular radial velocity to 1047 radians per second. Other angular velocities are set to zero.

To apply the velocity boundary condition, an amplitude was defined. This amplitude helps to apply the boundary condition in a very progressive manner so that we would not distort any element or cause any unnecessary strain or stress on the fan blade structure during the first seconds of the motion. This amplitude is called a step time of the smooth step type and has the shape presented in Figure 8-3.

In the first tests, it was noted that not defining this amplitude resulted in the immediate application of the full angular speed to an initially motionless system. This translated into the application of an infinite acceleration to the blade base nodes that distorted the mesh and caused the analysis to crash.

Hence in the retained analysis methodology, this smooth step time has been applied over nine seconds as presented in Figure 8-3. This means the engine rotating speed goes from 0 to 1047 radians per second in that period of time.

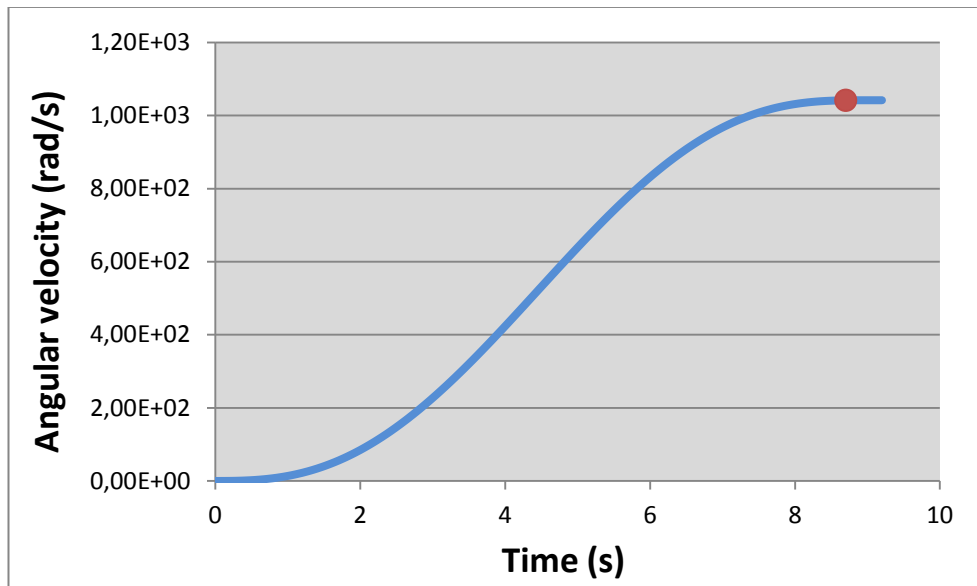


Figure 8-3: Progressive application of the rotating motion to the fan blade

The extraction of the velocities that are fed to the next analysis model is performed at time equal to 9 seconds as it is marked by a red dot in Figure 8-3. This is a critical point in time at which the stresses in the blade reach a maximum just before the establishment of a permanent regime.

8.2.6 Implicit analysis results

Figure 8-4 shows the obtained stress distribution inside the fan blade at the end of the implicit analysis phase. It is noted that this distribution is the same as the one obtained by G. Toussaint (5) using in LS-DYNA. Our goal running this preload analysis is to obtain the velocity vector at each node of the fan blade so this information can be imported in the second analysis. Importing that information will enable us to apply a velocity boundary condition in the impact analysis that will set the blade in motion in the explicit analysis.

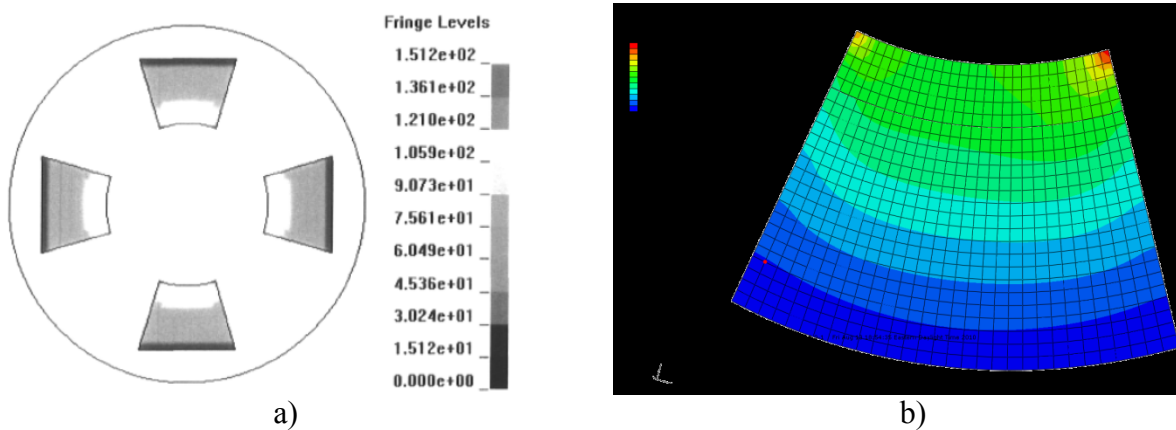


Figure 8-4: a) Stress distribution inside the fan blade obtained by G. Toussaint (5) using LS-Dyna. b) Stress distribution obtained in Abaqus

8.3 Second analysis setup: fan blade containment

The second analysis has been set up using the Abaqus explicit solver environment. The fan blade geometry needs to be imported from the first analysis.odb result file. Also, on that geometry a velocity predefined field calling the previous .odb result file needs to be defined to set the fan blade in motion. The standard metallic engine casing is replaced by a hybrid model, meaning that it is made of an assembly of a metallic base layer and of several dry fabric composite layers wrapped around it. In the considered model there are four layers of Kevlar fabric wrapped around the cylindrical inner aluminum shell.

8.3.1 Definition of the geometry

The first operation to set up the analysis is to create the geometric model of the engine casing. Then, from the implicit analysis result file, the geometry of the tip of the blade is imported and assembled to form the fan case model.

The engine casing is thus made of four concentric cylinders as presented in Figure 8-5 a). The innermost cylinder is metallic and the four other cylinders are made of fabric composite materials. Of course we will be using the developed VUMAT user subroutine to model the composite behavior during impact. Each cylinder radius is increased by 0,2499 mm to account for the exact thickness of the material. The inner radius of the innermost metallic skin is 250mm; the length of the cylinder is 150 mm. These are approximately the values used in LS-Dyna by G. Toussaint(5) which are respectively 249 mm and 105 mm.

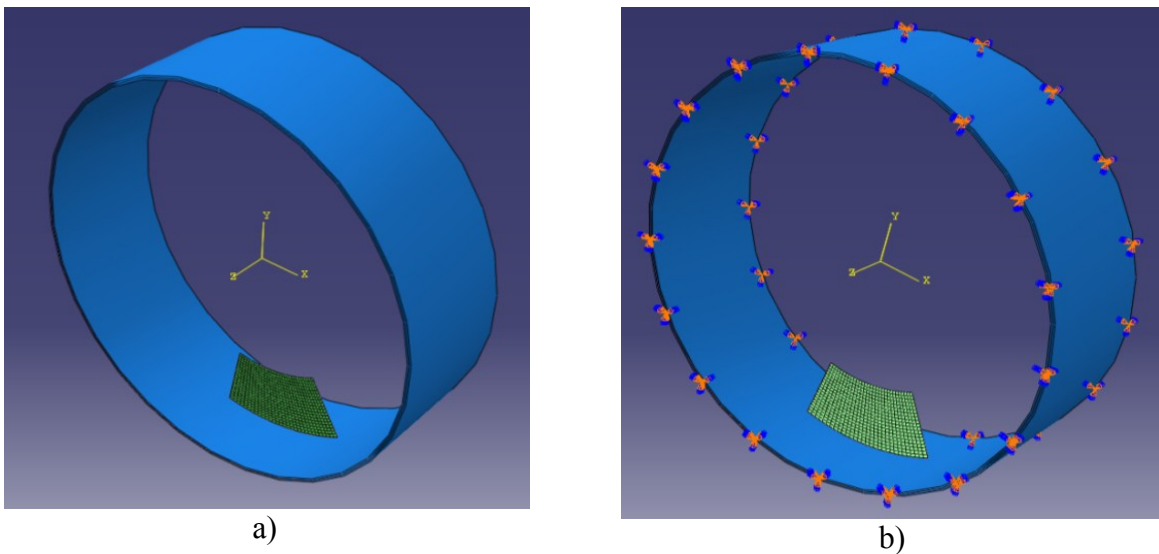


Figure 8-5: a) Assembly of the casing and the fan blade for the explicit analysis, b) definition of the boundary condition on the edges of the casing to fix it rigidly in space.

8.3.1 Definition of the materials

The material properties of aluminium used for the inner layer of the casing are presented in Table 8-2.

Table 8-2: Aluminum properties for the definition of the fan blade

Young's Modulus	72 Gpa
Poisson's Ratio	0.32
Plastic: yield stress	0.077951 Gpa
Plastic strain	0
Plastic: yield stress	0.21378 Gpa
Plastic strain	0.18
Mass density	2.78
Fracture Strain	0.18
Stress Triaxiality	0.3
Strain Rate	0

Hardening for this material has been defined as isotropic in Abaqus. The blade's shell elements thickness is 4.98 mm

8.3.2 Interactions

To define the contact between the blade and each layer of material that compose the casing as well as the contact between layers themselves, we used a "general contact" option available in Abaqus (already presented in Chapter 6).

8.3.3 Contact property

A contact property was used to define the mechanical surface interaction models that govern the behavior of surfaces when they are in contact. The default contact property model in Abaqus/Explicit assumes "hard" contact in the normal direction. Contact property assignments propagate through all analysis steps in which the general contact interaction is active. The normal behavior is set to allow separation after contact with a "Hard" contact pressure overclosure behavior using the standard constraint enforcement method. Tangential behavior is defined to be frictionless.

8.3.4 Boundary conditions

There is only one boundary condition applied to fix the casing in all directions of space as is shown in Figure 8-5 b). It has been applied at the two edges of the cylinders to approximate the manner in which the composite strap is integrated in the engine.

8.3.5 Predefined field

The predefined field has been used to import the velocities at each node of the blade as well as the strains and stresses which are obtained at the end of the first analysis phase and to apply them to the imported geometry of the blade.

To do this, we need to place the output database file from the first analysis in the second, explicit analysis folder. Then using the Abaqus guest user interface, we chose to create predefined field, selecting the mechanical category and velocity type. Then we select the geometry of the blade as the region on which to apply the predefined field. Finally we selected the step at which the predefined field has to be applied. This is used to define the initial state of the blade in the analysis during the initial step before the explicit analysis step definition in the software. Abaqus also gives the users the opportunity to select which frame of the previous analysis they want to extract from. In our case we extracted the results at the last frame.

8.4 Impact on the hybrid casing

The graphical results that show the evolution of the blade impact analysis are given in Figure 8-6. As it can be seen the blade is progressively going through the casing. The element deletion parameter is removing all the damaged elements from the analysis. The analysis takes approximately 20 minutes to run but this time could be reduced by modeling only half of the casing.

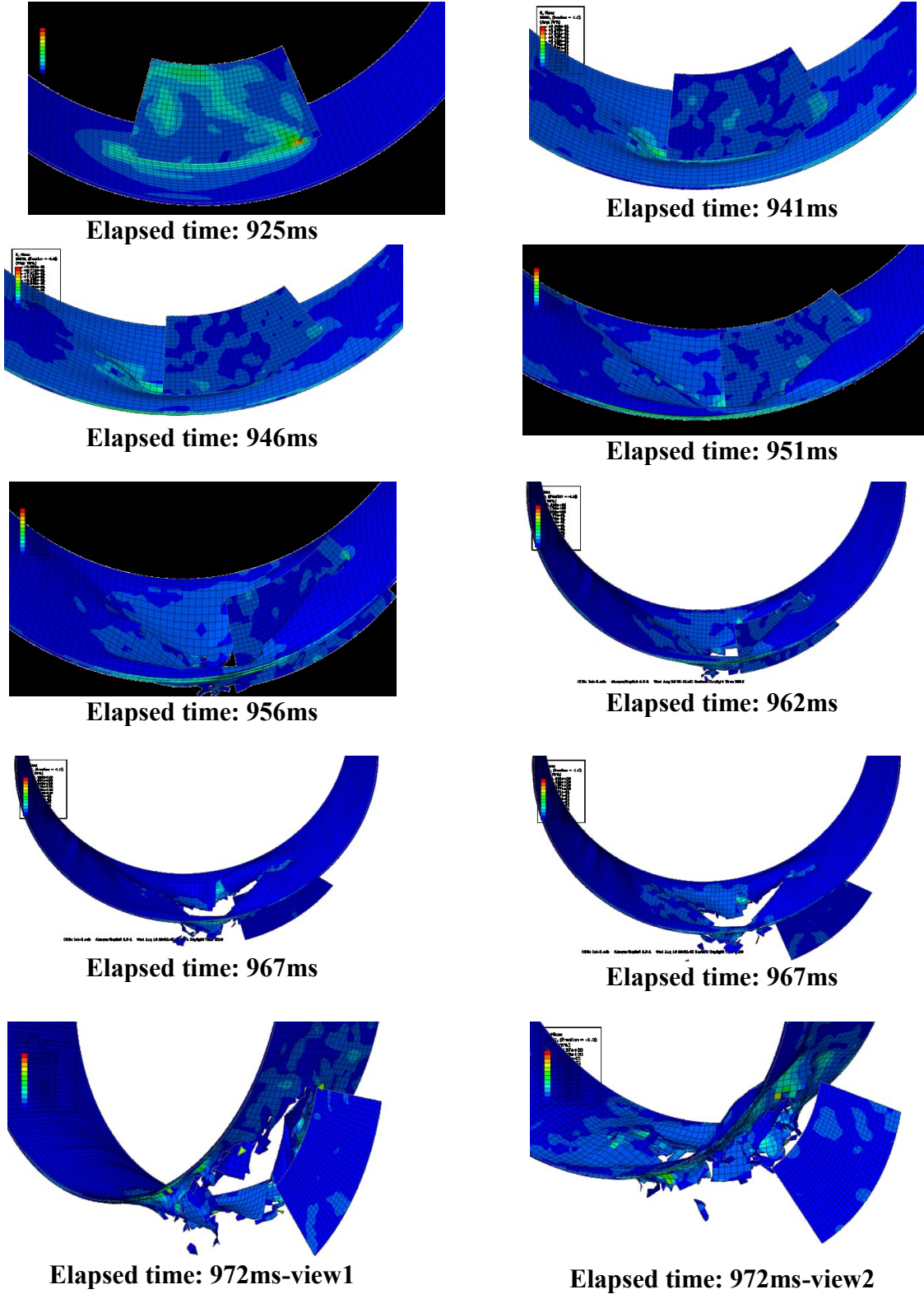


Figure 8-6: Graphical evolution of the impact analysis of the fan blade on the hybrid casing

To complete this graphical extraction, we plotted in Figure 8-7, the curve which shows the drop in velocity of the fan blade during the impact. We can observe that the fan blade has an initial velocity of 149 m/s and over the course of the analysis this velocity decreases to approximately 125 m/s. Hence, the blade perforates the containment casing and exits at 125 m/s. It is possible to note that the second dynamic analysis starts at the point in time where the previous analysis stopped and this is why the curve is plotted from 9.2 s (Figure 8-7).

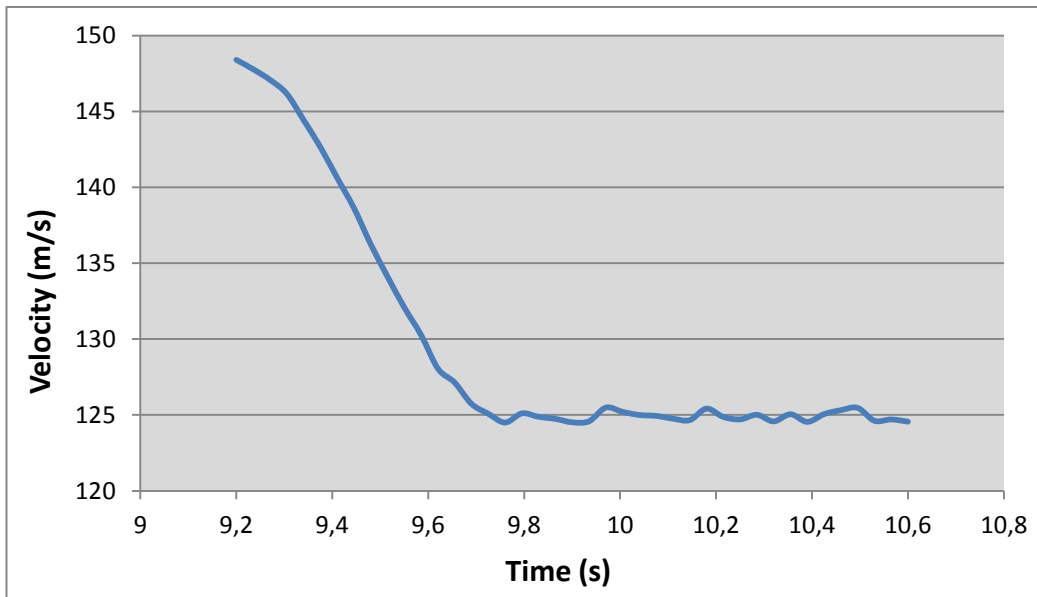


Figure 8-7: Blade's velocity over the duration of the analysis

To validate the results, we plot the energy curves for this impact analysis and extracted the internal energy (ALLIE), the kinetic energy (ALLKE) and the total energy of the model (ETOTAL). We plot the curves representing these three quantities as it is shown in Figure 8-8.

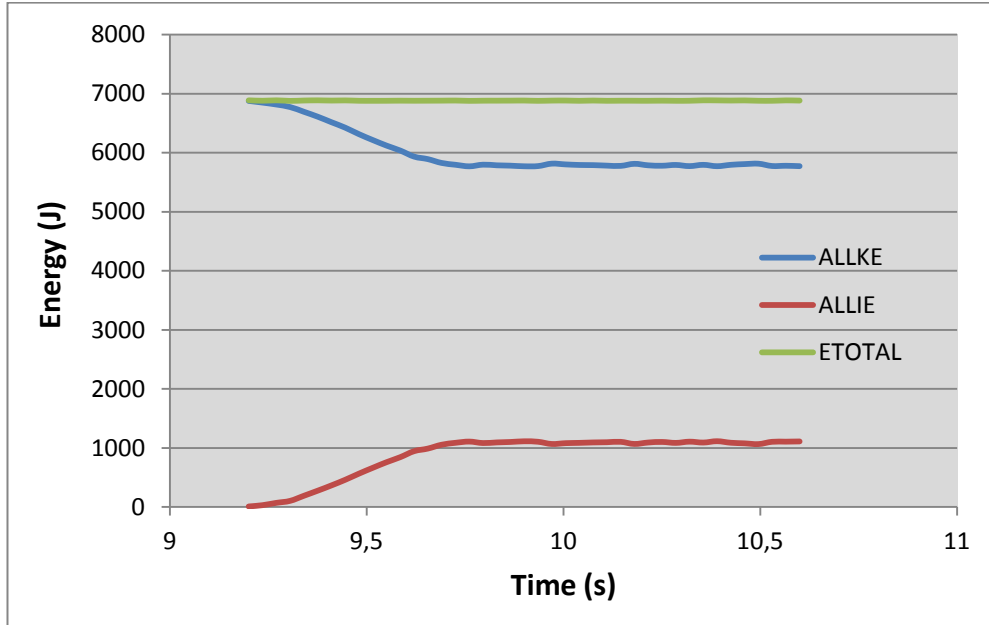


Figure 8-8: Energy curve of the blade’s velocity over the duration of the analysis

We may observe that the total energy of the model remains constant over the duration of the analysis which indicates that our model is valid. Furthermore the loss of velocity that we observed before is translated in a loss of kinetic energy which is transferred to the casing as internal strain energy that deforms and damages it. This is the main reason for the observed increase of internal energy of the model. Those few observations demonstrate that the model is behaving correctly.

8.5 Impact on full metal casing

In this paragraph, we will focus on finding the number of aluminum layers required to contain the fan blade debris. This has been done through a trial and error approach. We set up six analyses to test different configurations of the engine containment involving different number of 0.5 mm thick aluminum layers which is exactly the value used by G. Toussaint (5) to set up her analysis in LS-Dyna. The configuration of the analysis is presented in Figure 8-9 and depicts the twenty-four layer thick aluminum casing. The total computation time to run a twenty four layers fully metallic model is approximately 35 minutes.

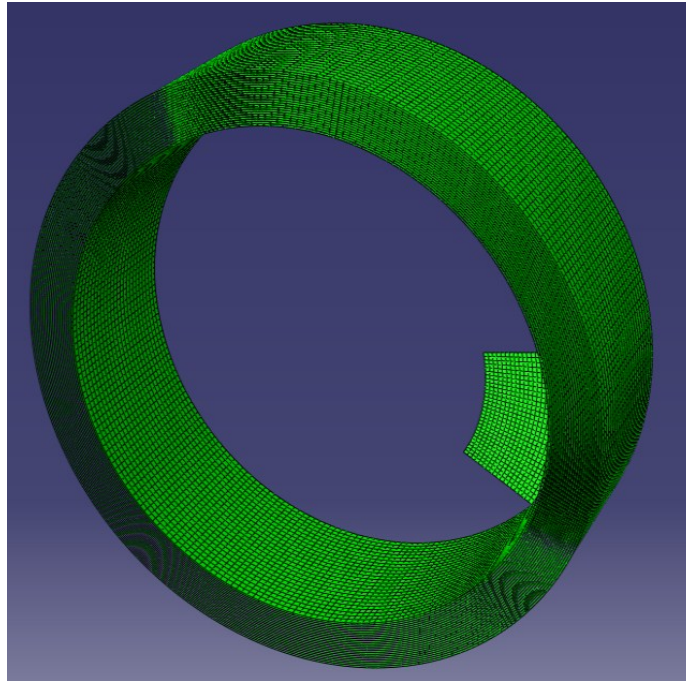


Figure 8-9: Fan containment made of twenty four layers of aluminum

We tested the following configurations: four layers, eight layers, twelve layers, eighteen layers, twenty layers and twenty-four layers, extracted the final velocity of the projectile and summed up the results in Table 8-3. The table shows that twenty-four layers is very close to stopping the projectile thus we can conclude without doubt that twenty-five layers of aluminum would stop the projectile from escaping the containment. Figure 8-9 is interesting since it is very close to the result obtained by G. Toussaint through the FEA model. It is stated that a thickness of 12.7 mm of aluminum is enough to stop the debris. In our case, stopping the blade takes twenty-five layers of 0.5 mm thickness which leads to a total thickness of 12.5 mm. Surely a unique 12.5 mm thick layer could have been used to accomplish this task but doing it this way, our goal was to validate the adequacy of the contact algorithm used to model the interaction between numerous layers.

Table 8-3: Results obtained from FEA

Number of layers	Total thickness of the casing (mm)	Final velocity of the fan blade debris (m/s)
4	2	123,254
8	4	110,956
12	6	95,4771
18	9	81,8509
20	10	35,9109
24	12	0,6278

Finally to fully verify our statement, we ran the analysis using twenty-five layers of aluminum and it indeed stops the blade as is shown in Figure 8-10. The stresses are very low at the end of the analysis because there is no longer any displacement of the blade and this is proven in Figure 8-10 (b).

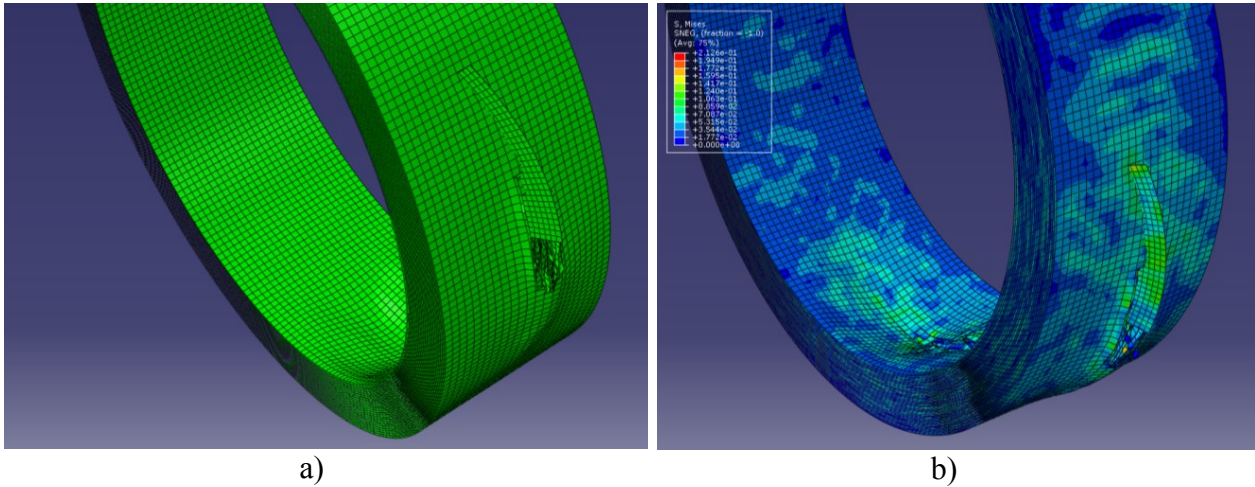


Figure 8-10: Analysis results for the 25-layer fan containment: (a) the blade has been stopped inside the containment, (b) graphical representation of the stresses at the end of the analysis.

Finally, we plotted the FEA results in a graph to fully understand how a variation in the number of layers was affecting the final debris velocity. This is shown in Figure 8-11 along with a quadratic regression of the results we obtained through FEA modeling.

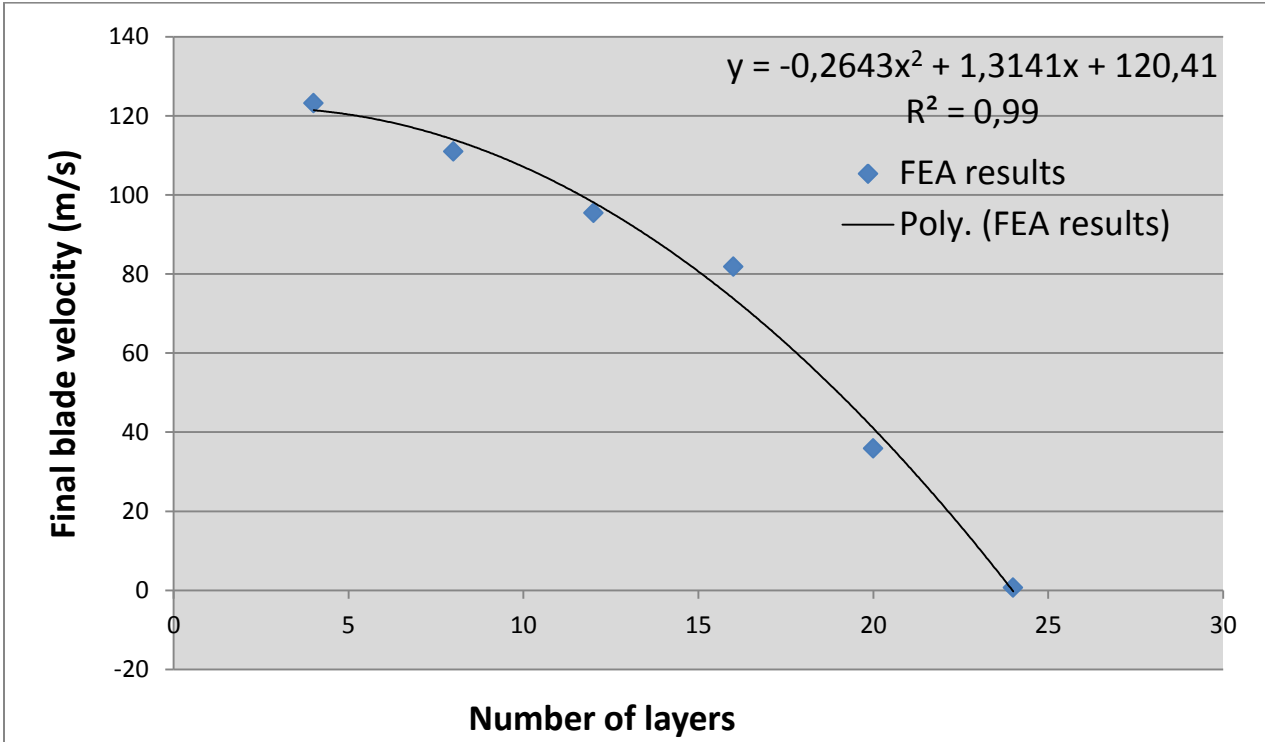


Figure 8-11: Blade's velocity over the duration of the analysis

The equation linking the number of layers in the containment with the final velocity of the blade is given below:

$$f(X) = -0,2643X^2 + 1,3141X + 120,41 \quad (8.1)$$

8.6 Hybrid fan case containment study

In this section we will go over the simple optimization process to obtain the number of layers needed to stop the fan blade and contain it. As we did before with the optimization of the impact on the fabric plate in chapter 7 we will correlate the number of layers of fabric with the final velocity of the blade. We remind the reader that the fabric plies are wrapped around an inner metallic casing. While running the simulations for four, six, eight and ten layers of fabric and it was possible to obtain the following results which are presented in Figure 8-11. The final velocity of the blade for the four-ply casing is approximately 133 m/s, for the six-ply casing it is 131 m/s, for the eight-ply casing it is 129 m/s and finally for the ten-ply casing it is 124 m/s.

The reason why we stopped our analysis to ten layers is that it takes too much time to compute. Indeed we are modeling the full casing with 54830 elements (not including the number of elements of the blade) each calling the subroutine to compute the updated stresses at each time increment. This causes the computations to exceed one hour for ten layers of fabric.

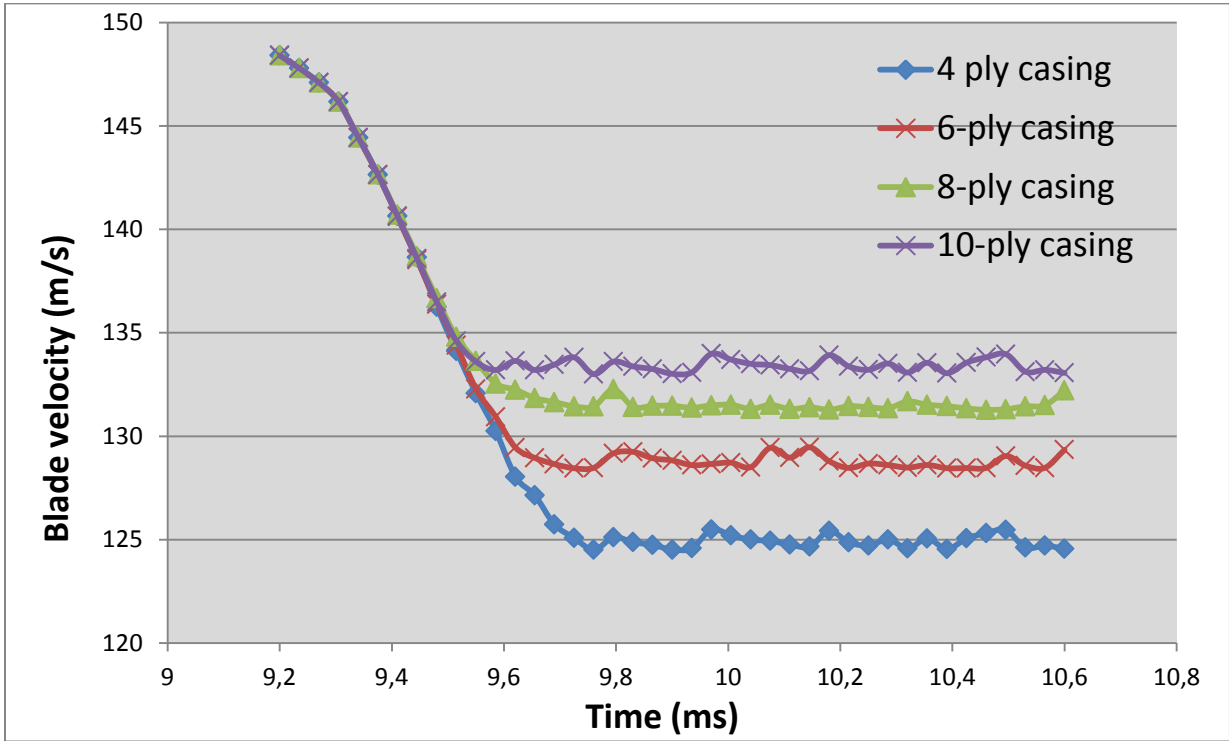


Figure 8-12: The fan blade's velocity evolution on different configurations of the hybrid casing

These four results were used to construct a quadratic function (Figure 8-13). We raise the reader's attention towards the regression coefficient's value R^2 which is very close to one. Also, we can observe that the form of the equation and its coefficient are very close to the one obtained for the fully metallic casing. It is not surprising that adding layers to the containment affects the final velocity of the debris in the same way.

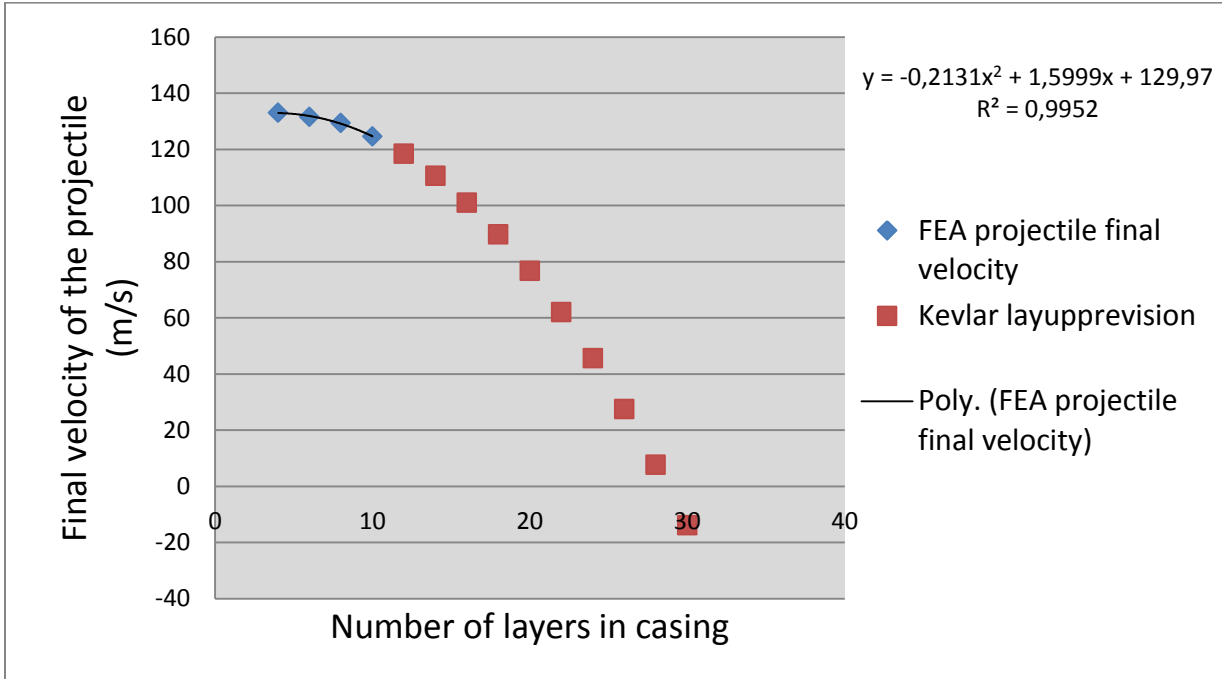


Figure 8-13: Velocity evolution predictions of the fan blade for different configuration of the casing

The interpolation done in Excel of the FEA results yields the following function to predict the number of Kevlar layers needed to stop the blade:

$$f(X) = -0.2131X^2 + 1.5999X + 129.97 \quad (8.2)$$

Using this function, a few predictions have been done which are shown them in red in Figure 8-13. This analysis leads us to determine that approximately thirty layers of fabric are needed to stop the projectile from completely perforating the engine casing.

One might consider that we have insufficient data to make such a prevision. In order to further support our conclusion we have run a very large analysis for a thirty layers of fabric configuration of the containment vessel. Thirty layers were chosen specifically because it is roughly the number of layers needed to stop the projectile. This analysis crashed before completion but the goal was to observe the evolution of the impactor velocity for the first increments of the analysis and to compare it with the evolution obtained for the blade working with a twenty-five layer full metallic casing which is able to stop the projective. The results are presented in Figure 8-14.

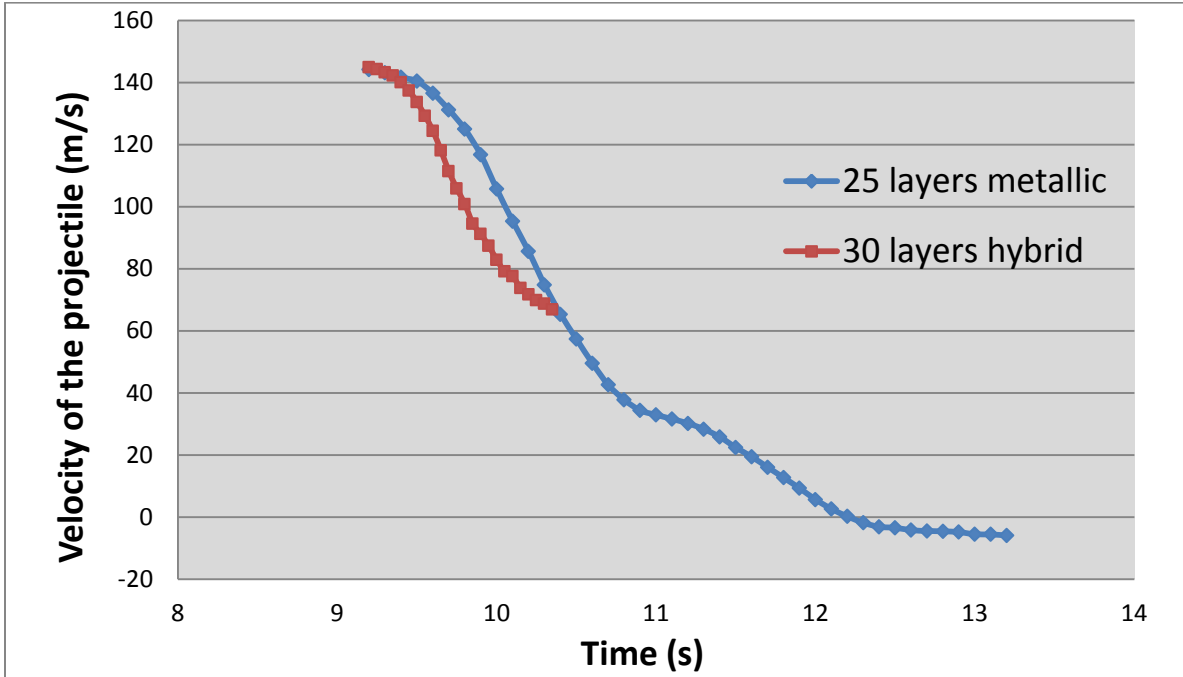


Figure 8-14: Comparison of the blade velocity evolution for the twenty-five layer metallic casing and the thirty layer hybrid casing

We can observe the evolution of the two velocities is roughly the same at the beginning of the analysis time. Since the thirty layers hybrid casing analysis behaves the same way as the projectile stopping twenty-five layer metallic casing we can reasonably assess that a thirty layer hybrid casing might be able to stop the projectile.

At least the evidence we presented in this paragraph lead us to make that conclusion but we could not fully demonstrate it. Obviously further testing will be needed to fully verify this statement.

8.6.1 Computation interruption

Performing our various numerical tests on multiple configurations of the hybrid casing we had to stop at ten layers of fabric on top of the metallic internal casing. The main reason is that the analysis becomes progressively too unstable to compute and crashes. This phenomenon appeared starting at eleven layers of fabric. Two hypotheses have been made to try to explain this problem. First, the instantaneous damage law defined in the VUMAT has been identified as a potential problem which would lead to numerical instabilities. In our case, using the element

deletion option in Abaqus implies that the element is removed as soon as the damage criterion is met. Simply put, element deletion leads to a loss of material implying a loss of internal energy while affecting the stability and accuracy of the contact algorithm.

In theory, a progressive damage law would have delayed the occurrence of such instabilities since the law would not have translated into instantaneous damage of a large number of elements leading to their immediate removal in the early stages of the analysis. This is obviously causing a brutal instability of the contact algorithm in Abaqus. Instead, it would have progressively damaged the elements and thus smoothed the removal of elements throughout the duration of the analysis. This would have enabled us to add layers to the hybrid casing and run the full analysis without it crashing. Unfortunately no testing of this assumption has been carried out in this work.

Exploring other possible ways to solve this instability would include the use of the corotational frame based on fiber frame (FF approach) as described by Badel in his works (8) to replace the GN approach as a possible solution. According to this paper, a calculation run using the FF approach completed whereas the GN approach failed suggesting that this might be a way of solving the crash issue encountered. More developments need however to be done to implement the FF approach in the VUMAT user subroutine.

8.7 Conclusion

Overall we obtained results similar to those obtained by G. Toussaint (5) using an in-house fabric VUMAT user subroutine. If we assume that our prediction for the composite casing is right, we are able to calculate roughly the mass for each configuration. The results are summed up in Table 8-4.

Table 8-4: Weight reduction approximate study

	Number of layers needed	Approximated mass of one layer (kg)	Total mass of the configuration (kg)
Metallic configuration	25	0.3240	8.0994
Hybrid configuration	30	0.1663	4.989

In this situation we observe that the hybrid configuration represent an approximate 35% mass savings which is the same order of magnitude when compared to the weight reduction observed in the industry.

GENERAL CONCLUSION

In this work we have been able to successfully create a material user subroutine for the finite element software Abaqus. This user subroutine is used to capture the physics of a fabric' yarn crossover under dynamic loadings. This user subroutine has been validated using a S4R shell element available in Abaqus. After the validation it has been used to model the dynamic behavior of a composite plate of varying layup in a simple impact problem. A quick study has been carried out to assess the influence of the most important parameters (element size, crimp angle, plate size, impactor velocity etc...) over the impactor final velocity and the ability of the composite to stop the projectile. The routine has finally proven successful in demonstrating its capabilities in an industrial problem dealing with the containment of engine fan blade debris. We were also able to re-produce the results obtained by Geneviève Toussaint (5) concerning the simplified metallic engine casing using LS-Dyna software.

The main problem of the subroutine lies in the fact that it is still pretty expensive to run in terms of computational time. Indeed it takes approximately one hour to run the analysis with a 10-ply fabric containment system. A simple solution would be to increase the size of the elements used

General conclusion

in the model. In that case, great caution should be taken in assessing the quality and accuracy of the results that could be obtained using this solution. Also it would be very interesting to consider creating a user subroutine that would be able to capture the behavior of four crossovers instead of just one. This would double the size of the shell elements thus leading to tremendous reductions in computational time.

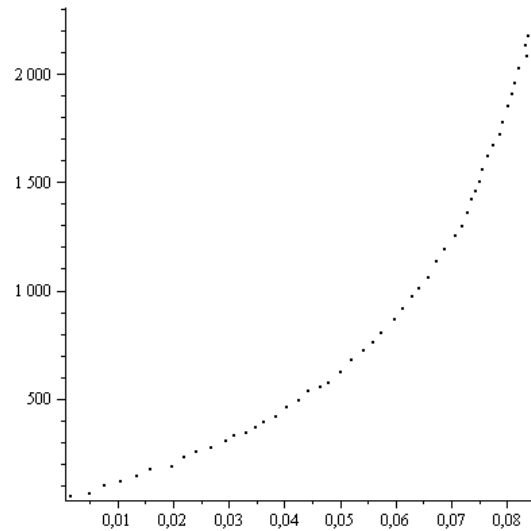
Another problem to address is the stability of the analysis. We need to be able to complete an analysis run for a casing model allowing us to studying more than 10 plies of fabric. In that direction it would be a very interesting subject to explore the application of a progressive damage law to this problem. Also the FF approach proposed by Badel (8) would be very interesting to look at. These two potential solutions would surely benefit computational stability as well as the overall accuracy of the results.

Finally, it should be kept in mind that the model used for the fan blade containment is very simplified and is merely used to demonstrate the possible application of the tools we developed to this specific field. These tools could be used to, at least, validate some basic results and explore the gains of using fabric and composites in general to replace metal in aeronautical primary structures. We have very briefly demonstrated at the end of this work that for this application and for the same design requirements, a composite part can enable us to achieve a double digit percentage of weight reduction for aeronautical structures.

In future work, in order to reduce the computational time, it would be interesting to use multiscale finite element modeling approach in which the developed VUMAT model and associated shell element is used in the region prone to impact, damage and perforation and using simplified membrane shell element in region not involved at all in this high strain loading.

APPENDIX A – MAPLE CODE FOR PARAMETER DETERMINATION

```
> restart: with(linalg): with(plots): with(Optimization): with(LinearAlgebra):  
#=====  
#   Donnees experimentales  
#=====  
fich:= "./test1.txt":  
Data:=readdata(fich,2):  
Data1:=convert(Data,Matrix):  
N:=RowDimension(Data1):  
x:=Vector(N):  
y:=Vector(N):  
for i from 1 by 1 to N do  
  x[i]:=Data1[i,1]:  
  y[i]:=Data1[i,2]:  
end do:  
Fig1:=pointplot({seq([x[i],y[i]],i=1..N)},color=black, symbol=point):  
Fig1;
```



```

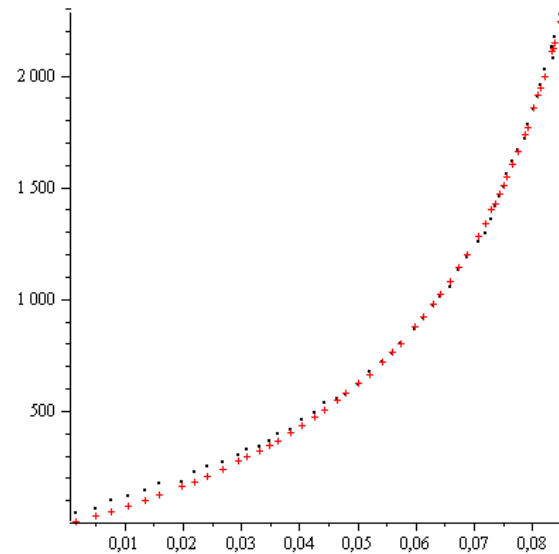
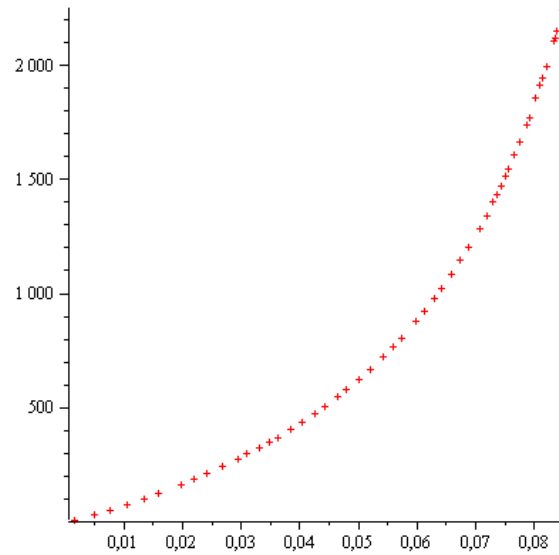
> ya:=Vector(N):
for i from 1 by 1 to N do
  ya[i]:=b*x[i]/(a-x[i]):
  #print(ya[i]);
end do:
>
#=====
#  Fonction cout
#=====
  FC:=0.:
  for i from 1 by 1 to N do
    FC:=FC+(y[i]-ya[i])^2:
  end do:
  #print(FC);
  fonc_cout:=unapply(FC,a,b):

#=====
# Procédure d'Optimisation
#=====
  Alpha0:=NLPsolve(fonc_cout(a,b),assume=nonnegative) :
>
> assign(Alpha0[2]);
a;
b;
a := 0.12389
b := 983.39

> Fig2:=pointplot({seq([x[i],ya[i]],i=1..N)},color=red, symbol=cross):

```

Fig2;
display(Fig1, Fig2);



APPENDIX B – NEWTON RAPHSON ALGORITHM

The Newton-Raphson algorithm has been used in our work because we need to find the optimized solution to the following system of equations (we will describe this later in this chapter):

$$\begin{cases} f_1(H_{W_{iter}}, H_{F_{iter}}) = F_{C_W}(H_{W_{iter}}) - F_{C_F}(H_{F_{iter}}) = 0 \\ f_2(H_{W_{iter}}, H_{F_{iter}}) = H_{W_{iter}} + H_{F_{iter}} - H_{W_{init}} - H_{F_{init}} + dc_W + dc_F = 0 \end{cases} \quad (6.1)$$

In this section we will briefly present the mathematical principles of the Newton-Raphson algorithm that has been used in our material to calculate the height of the point of contact between the yarns. The full development and integration of the equations is given in the subroutine program in appendix B.

Basically the Newton-Raphson algorithm is a simple multidimensional root finding method. This method has been chosen because while simple it is very efficient to converge to a root given if we are able to make a sufficiently good initial guess. Our problem gives $N = 2$ functional relations to be zeroed involving $n = 2$ variables.

$$F_i(x_1, x_2) = 0 \quad i = 1, 2. \quad (6.2)$$

We let x denote the entire vector of values x_i and F denote the vector of functions F_i . In the neighborhood of x , each of the functions F_i can be developed in Taylor series as such:

$$F_i(x + \delta x) = F_i(x) + \sum_{j=1}^N \frac{\partial F_i}{\partial x_j} \delta x_j + O(\delta x^2) \quad (6.3)$$

The matrix of partial derivatives appearing in the previous equation is the Jacobian matrix J .

$$J_{ij} = \frac{\partial F_i}{\partial x_j} \quad (6.4)$$

We can also express equation 4.93 in matrix notation.

$$F(x + \delta x) = F(x) + J \cdot \delta x + O(\delta x^2) \quad (6.5)$$

By neglecting terms of order δx^2 and higher and by setting $F(x + \delta x) = 0$, we obtain a set of linear equations for the corrections δx that move each function closer to zero simultaneously. Technically we have to solve the following matrix equation:

$$J \cdot \delta x = -F \quad (6.6)$$

If we consider a matrix called A which is the result of the product of two matrices L which is lower triangular and U which is upper triangular then this matrix equation can be solved by using the LU decomposition dealing with the following typical form of matrix equation:

$$L \cdot U = A \quad (6.7)$$

We can further decompose this equation using x which is the initial guess of the solution needed to start the iterations as such:

$$A \cdot x = (L \cdot U) \cdot x = L \cdot (U \cdot x) = b \quad (6.8)$$

b is a matrix in this equation. Using 4.18, first we solve:

$$L \cdot y = b \quad (6.9)$$

Then, using y we solve:

$$U \cdot x = y \quad (6.10)$$

We finally get U which is none other than $(\delta x_1, \delta x_2)$. The corrections are then added to the solution vector:

$$x_{new} = x_{old} + \delta x \quad (6.11)$$

The process is then iterated to convergence.

Bibliography

1. **GRUJICIC, M., et al.** Development and verification of a meso-scale based dynamic material model for plain-woven single-ply ballistic fabric. *Journal of Materials Science*. 16 August 2008, pp. 6301-6323.
2. **SHAHKARAMI, A. et VAZIRI, R.** A continuum shell finite element model for impact simulation of woven fabrics. *International Journal of Impact Engineering*. 2007, Vol. 34, pp. 104-119.
3. **SHERBURN, MARTIN.** *Geometric and Mechanical Modelling of Textiles*. s.l. : Université of Nottingham, July 2007.
4. **SHAHKARAMI, Ali.** An efficient unit cell based numerical model for the continuum representation of fabric systems. *Thesis*. University of British Columbia : s.n., 2006.
5. **TOUSSAINT, GENEVIÈVE.** *Modélisation du confinement des débris des pales d'un moteur d'avion dans un caisson hybride métal-composite*. Université Laval, Département de Génie Mécanique. Québec : s.n., 2006.
6. **LONG, A.C.** *Design and manufacture of textile composites*. s.l. : Woodhead Publishing, July 2005.
7. **CHRÉTIEN, NICOLAS.** *Numerical constitutive models of woven and braided textile structural composites*. Blacksburg, Virginia : Virginia Polytechnic Institute and State University, April 2002.
8. **BADEL, P., VIDAL-SALLE, E. et BOISSE, P.** Computational determination of in-plane shear mechanical behavior of textile composite reinforcements. *Computational Materials Sciences*. 2007, pp. 439-448.
9. **LOMOV, SV., et al.** Full-field strain measurements for validation of meso-FE analysis of textile composites. *Composites: Part A*. 2008, 39, pp. 1218-1231.
10. **DURVILLE, D.** A finite element approach of the behavior of woven materials at microscopic scale. *11th Euromech-Mecamat conference - Mechanics of microstructured solids : cellular materials, fiber reinforced solids and soft tissues*. Torino, Italy : s.n., 2008.
11. **VANDEURZEN, P., IVENS, J. et VERPOEST, IA.** Three dimensional micromechanical analysis of woven-fabric composites: II Elastic analysis. *Composites Science and Technology*. 1996, pp. 1317-1327.
12. **ZHOU, G., SUN, X. et WANG, Y.** Multi-chain digital element analysis in textile mechanics. *Composites Science and Technology*. 2004, pp. 239-244.
13. **SAGAR, T.V., POTLURI, P. et HEARLE, J.W.S.** Mesoscale modelling of interlaced fibre assemblies using energy method. *Computational Material Science*. 2003, 28, pp. 49-62.
14. **BUET-GAUTHIER, K. and BOISSE, P.** Analyse et simulation du comportement mécanique des renforts composites tissés. *Thesis*. Thesis LMSP Orléans : Université d'Orléans, 1998. p. 125.
15. **DUMONT, F.** Expérimentations et modèles de comportement de renforts de composites tissés. *Thesis*. Paris : Université de Paris VI, 2003. p. 149.
16. **ROLANCE, D. et WANG, SS.** *Penetration mechanics of textile structures ballistic materials and penetration mechanisms*. Amsterdam : Elsevier, 1980. pp. 273-292.
17. **SHIM, VPW., LIM, CT. et FOO, KJ.** Dynamic mechanical properties of fabric armour. *International Journal of Impact Engineering*. 2001, 25, pp. 1-15.

18. **LIM, CT., SHIM, VPW. et NG, YH.** Finite element modeling of the ballistic impact of fabric armor. *International Journal of Impact Engineering*. 2003, 28, pp. 13-31.
19. **SHOCKEY, D.A., ELRICH, D.C. et SIMONS, J.W.** *Improved barriers to turbine engine fragments: Final annual report*. 2002. DOT/FAA AR-99/8.
20. *Modeling friction effects on the ballistic impact behavior of a single-ply high-strength fabric.* **DUAN, Y., et al.** 996-1012 : s.n., 2005, International Journal of Impact Engineering.
21. **KAWABATA, S., NIWA, M. et KAWAI, H.** The finite deformation theory of plain weave fabrics, Part I: The biaxial deformation theory. *Journal of textile institute*. 1973, 64, pp. 21-46.
22. **IVANOV, I. et TABIEI, A.** Loosely woven fabric model with viscoelastic crimped fibres for ballistic impact simulations. *International Journal of Numerical Method Engineering*. 2004, 61, pp. 1565-1583.
23. **KING, MJ., JEANANISILAWONG, P. et SOCRATE, S.** A continuum constitutive model for the mechanical behavior of woven fabrics. *International Journal of Solid Structure*. 2205, Vol. 42, pp. 3867-3896.
24. **BOISSE, P., et al.** Meso/macro-mechanical behavior of textile reinforcements for thin composites. *Composites Sciences and Technology*. 2001, Vol. 61, pp. 395-401.
25. **PENG, X. et CAO, J.** A dual homogenization and finite element approach for material characterization of textile composites. *Composites Engineering*. 2002, 33, pp. 45-56.
26. **SCOTT, B.R. et YEN, C.-F.** Analytic design trends of fabric armor. *22nd International Symposium on Ballistics*. Vancouver, BC, CANADA : s.n., 2005.
27. **PEIRCE, F.** The geometry of cloth structure. *Journal Textile Institute*. 1937. 28, pp. 45-96.
28. **V.F. POTERASU, L. BEJAN.** Woven composite material design by orthotropic compliance averaging method using mathematica. 1998.
29. **WARREN, W.** The large deformation elastic response of woven kevlar fabric. *Polymer Composites*. 1992, 13, pp. 278-284.
30. **REALFF, M.L., BOYCE, M.C. et BACKER, S.** A micromechanical model of the tensile behavior of woven fabric. *Textile Research Journal*. 1997, 67, pp. 445-459.
31. **SHAHKARAMI, A., et al.** A numerical investigation of the effect of projectile mass on the energy absorption of fabric panels subjected to ballistic impact. *Proceedings of the 18th international symposium on ballistics*. 2002, pp. 802-809.
32. **GRUJICIC, M., et al.** A meso-scale unit-cell based material model for the single-ply flexible-fabric armor. *Materials and Deign*. 2009, 30, pp. 3690-3704.
33. **NG, S., TSE, P. et LAU, K.** Numerical and experimental determination of the in-plane elastic properties of 2/2 twill weave fabric composites. *Composites*. 1998, 29B, pp. 735-744.
34. *Meso-macro modelling of fiber-reinforced rubber-like composites exhibiting large elastoplastic deformation.* **REESE, S.** Bochum, Germany : Department of Civil Engineering, Institute for Mechanics, Ruhr University, 2001.
35. **XUE, P., PENG, X. et CAO, J.** A non-orthogonal constitutive model for characterizing woven composites. *Composites*. 2003, Vol. Part A, 34, pp. 183-193.
36. **KAWABATA, S., NIWA, M. et KAWAI, H.** The finite-deformation theory of plain-weave fabrics Part II: The uniaxial-deformation theory. *Jounrla of Textile Institute*. 1973. Vol. 62, pp. 47-61.
37. —. The finite deformation theory of plain-weave fabrics Part III: The shear-deformation theory. *Journal of Textile Institute*. 1973. Vol. 64, pp. 62-85.

38. **PRODROMOU, A.G. et CHEN, J.** On the relationship between shear angle and wrinkling of textile composite preforms. *Composites - Part A: Applied Science and Manufacturing*. s.l. : 491-503, 1997. Vol. 28.
39. **McBRIDE, T.M. et CHEN, J.** Unit-cell geometry in plain-weave fabrics during shear deformations. *Composites Science and Technology*. 1997. Vol. 57, pp. 345-351.
40. **BADEL, P.** Large deformation analysis of fibrous materials using rate constitutive equations. *Computers and Structures*. 2008. 86, pp. 1164-1175.
41. **SIMULIA.** *Abaqus Theory Manual*. 2011.
42. **SHAHKARAMI, ALI.** Fabric Crossover UMAT: Input File Setup.